

## Department of Precision and Microsystems Engineering

### A ground structure based topology optimization method for thermofluid problems

Levi Dekker

Report no : 2021.073  
Coach : Ir. Max van der Kolk  
Professor : Dr.ir. Matthijs Langelaar  
Specialisation : Engineering Mechanics  
Type of report : Master Thesis  
Date : October 13, 2021



# A ground structure based topology optimization method for thermofluid problems

by

Levi Dekker

to obtain the degree of Master of Science  
at the Delft University of Technology,  
to be defended publicly on Monday October 13, 2021 at 10:00 AM.

Student number: 4224175  
Project duration: March 1, 2019 – October 13, 2021  
Thesis committee: Dr. ir. M. Langelaar, TU Delft, supervisor  
Ir. M. van der Kolk, TU Delft, supervisor  
Dr. ir. R. van Ostayen, TU Delft  
Dr. ir. W. Jin, ASML

An electronic version of this thesis is available at <http://repository.tudelft.nl/>.



# Abstract

In this thesis, a novel ground structure based thermofluid topology optimization method is presented which is applicable to problems with creeping flow. Creeping flow, also called Stokes flow, is found in a variety of engineering applications, primarily in the field of microfluidics. Topology optimization (TO) is a computational method that can generate optimized material layouts for systems/devices, given a certain performance objective and constraints. TO can be used to optimize fluid channel layouts of cooling devices; this is typically done with density-based TO and a Darcy-Stokes flow model. While this approach is able to improve the performance of cooling devices, certain benefits can be achieved by using a ground structure representation of the fluid channels and subsequently using the widths of the ground structure channel segments as design variables. By confining the flow to a Poiseuille flow pipe network, a significant reduction (up to a factor 13 in 3-D) in the number of degrees of freedom can be obtained compared to a finite element discretization of the Darcy-Stokes equations, thus reducing computation time. Other benefits of a ground structure representation are related to the increased control of explicit geometry features such as channel minimum/maximum width, channel to channel angles, or the number of channel branches at junctions.

In the first part of this thesis, the Ground Structure Projection (GSP) method is introduced and explained step by step. In every iteration of the GSP optimization routine, Poiseuille flow rates are calculated in a pipe flow network. With a projection step and *a priori* knowledge about laminar flow velocity profiles, the channel geometry and flow field are mapped onto an Ersatz material model and subsequently evaluated using an FEM discretization of the advection-diffusion equation. The modeling is validated with comparisons against a trusted commercial FEM package. For Reynolds numbers in the range of  $Re < 20$ , the GSP method shows fluid and thermal results within 5% accuracy of an FEM solution. Afterwards, a number of numerical cases are analyzed. A pressure drop optimization of a three branch Y-split channel layout serves as a verification case for the GSP method. Hereafter, an intricate Delaunay triangulated ground structure is used for a pressure drop and a multi-objective (pressure drop + average temperature) optimization. It is shown that the GSP method can achieve improved cooling performance with good objective convergence.

In the second part of this thesis, the presented GSP method is applied to an industrial case concerning the reduction of optical aberration of a Projection Optics Box (POB) mirror in an EUV photolithography machine from ASML. Extreme precision is required in EUV photolithography machines and hence any unwanted optical aberration of the POB mirrors must be minimized. However, the mirrors absorb some of the EUV radiation which results in thermomechanical deformation and consequent optical aberration. By optimizing the cooling channel layout to maximize surface temperature uniformity, an attempt is made to reduce optical aberration. A hybrid 2-D/3-D model is created which combines a 2-D cooling channel layer and a 3-D reflective surface layer. This model is used to evaluate the optimization objective which is taken as the mean square error (MSE) of the surface temperatures. It is shown that for a dipole and a circular heat load the temperature uniformity is improved significantly against a reference fluid channel layout. To check how well the choice for a temperature MSE objective translates to thermomechanical deformation reduction, an optimized design is transferred to a commercial FEM package (COMSOL Multiphysics®) and analyzed. Since the optical systems in the EUV machine can compensate for some optical distortion, a second order surface polynomial is fitted to the FEM deformed mirror surface. The residual root mean square (RMS) error of the FEM deformed surface and the polynomial fit serves as a measure for optical performance. The optimized design performs 20% better than the reference design with a residual RMS of 3.14  $\mu\text{m}$  versus 3.91  $\mu\text{m}$  respectively.



# Preface

I would like to thank Wenjie Jin from ASML and my thesis advisor Matthijs Langelaar for providing valuable feedback and guiding me in the process of writing this thesis. But most of all I want to thank Max van der Kolk, my daily supervisor, for the weekly discussions, feedback, useful insights, and always taking the time to answer my questions, even after Max left TU Delft for a new job.

*Levi Dekker*  
*Delft, September 2021*



# Contents

<b>1</b>	<b>Introduction</b>	<b>1</b>
1.1	Motivation . . . . .	1
1.2	Research goals and scope . . . . .	3
1.3	Thesis outline . . . . .	3
<b>I</b>	<b>A ground structure based topology optimization method for thermofluid problems</b>	<b>5</b>
<b>2</b>	<b>Background information</b>	<b>7</b>
2.1	Gradient based topology optimization . . . . .	7
2.1.1	Density-based method . . . . .	7
2.1.2	Ground structure TO . . . . .	9
2.1.3	Feature mapping . . . . .	10
2.1.4	Algorithms for gradient based TO . . . . .	10
2.2	Fluid channel topology optimization . . . . .	11
2.2.1	Governing equations of fluid dynamics . . . . .	11
2.2.2	Density based fluid channel TO . . . . .	11
2.2.3	Other fluid channel TO methods . . . . .	12
2.3	Thermofluid topology optimization . . . . .	13
2.3.1	Stabilization . . . . .	13
2.3.2	Examples from literature . . . . .	14
2.4	Feature mapping in thermofluid topology optimization . . . . .	16
2.4.1	Velocity mapping . . . . .	16
<b>3</b>	<b>Description of the GSP method</b>	<b>17</b>
3.1	GSP method routine . . . . .	17
3.2	Computing flow rates . . . . .	17
3.3	Projection onto FEM model . . . . .	18
3.3.1	Channel geometry projection . . . . .	18
3.3.2	Velocity projection . . . . .	20
3.3.3	Flow correction . . . . .	22
3.4	Sensitivities . . . . .	25
<b>4</b>	<b>Validation and optimization examples</b>	<b>27</b>
4.1	Validation . . . . .	27
4.2	Optimization example 1: Flow divider . . . . .	31
4.3	Optimization example 2: Minimizing pressure drop . . . . .	33
4.4	Optimization example 3: Cooling device . . . . .	34
<b>5</b>	<b>Benefits and limitations</b>	<b>37</b>
5.1	Benefits . . . . .	37
5.2	Limitations . . . . .	39
<b>II</b>	<b>Minimizing thermomechanical distortions in optical instruments</b>	<b>41</b>
<b>6</b>	<b>Thermally induced optical aberration</b>	<b>43</b>
6.1	TO of optical instruments . . . . .	43
<b>7</b>	<b>Problem description and model</b>	<b>47</b>
7.1	Optimization objective . . . . .	47
7.2	Hybrid model . . . . .	48
7.2.1	Coupling of cooling slab and mirror slab . . . . .	49
7.2.2	Validation . . . . .	50

<b>8</b>	<b>POB mirror optimization results</b>	<b>53</b>
8.1	Use case 1: Circular heat load . . . . .	54
8.2	Use case 2: Dipole. . . . .	54
8.3	Practical use and multi-objective optimization . . . . .	57
8.3.1	Increasing the cooling capacity . . . . .	57
<b>9</b>	<b>Finite Element Analysis of thermomechanical deformation</b>	<b>59</b>
<b>10</b>	<b>Conclusion and recommendations</b>	<b>61</b>
10.1	Ground Structure Projection method . . . . .	61
10.2	Projection Optics Box mirror . . . . .	62
10.3	Future work. . . . .	62
<b>A</b>	<b>Sensitivity analysis</b>	<b>65</b>
A.1	Temperature response sensitivities . . . . .	65
A.1.1	Implementation challenges . . . . .	66
A.2	Hybrid model . . . . .	67
<b>B</b>	<b>Additional data</b>	<b>69</b>
B.1	POB-mirror convergence plots . . . . .	69
B.2	Temperature distribution with zero flow . . . . .	70
B.3	Shoobox model thickness comparison . . . . .	70
<b>C</b>	<b>Validation</b>	<b>71</b>
C.1	Y-split channel structure . . . . .	71
C.1.1	Temperature comparison . . . . .	71
C.1.2	Velocity vectors . . . . .	75
C.2	Tapered channel . . . . .	76
	<b>Bibliography</b>	<b>79</b>

# Introduction

## 1.1. Motivation

With the advent of computer-automated design, engineers have the ability to augment their skills and creativity with the help of computational design methods such as Topology Optimization (TO). TO is a powerful method that can automatically generate entirely new and optimized structural designs or material layouts based on a predefined performance measure and constraints [9, 73]. An area in which TO has been applied but is not yet commonplace in industry is that of fluid cooling channels [2]. Optimizing fluid cooling channels requires a combination of thermal and fluid physics, hence this is commonly referred to as thermofluid TO. An example of thermofluid TO for cooling channels can be seen in Figure 1.1: on the left side is a channel layout designed by an engineer whereas the right side shows a channel layout that was algorithmically generated with thermofluid TO. For a uniform heat load, the optimized design performs better in minimizing the maximum temperature throughout the entire domain.

Most thermofluid TO methods in literature rely on the discretized Navier-Stokes equations to solve the fluid dynamics [2]. Computational Fluid Dynamics is often very intensive in terms of processing power. Even for flow in the creeping flow regime, i.e. slow laminar flow where inertial effects can be neglected, solving the fluid part is significantly more computationally intensive than solving the thermal Finite Element Method (FEM) equations [28, 98]. Combined with the successive iterations and model evaluations required for TO, this can lead to long computation times which form a hurdle to the engineer. Therefore, new methods that provide computational speed gains can be a valuable addition.

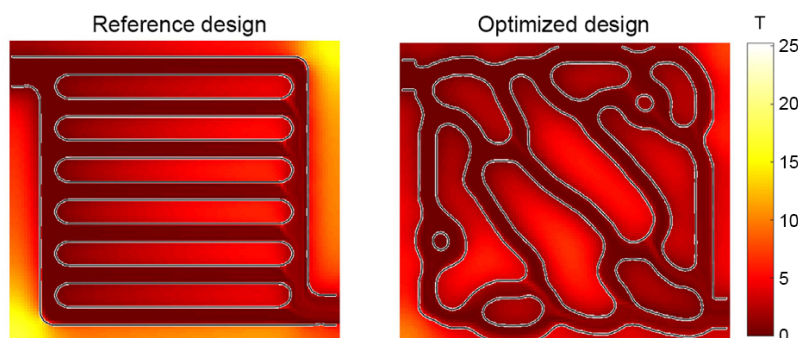


Figure 1.1: An example of fluid channel topology optimization [95]. On the left a simple reference design is depicted, on the right a design optimized to minimize the maximum temperature.

In this thesis, a novel ground structure based thermofluid TO method is presented which is applicable to problems within the creeping flow regime. Creeping flow, also called Stokes flow, is found in a variety of engineering applications. Examples include applications such as lab-on-a-chip technologies [77, 87], design of innovative materials [55, 60, 71], microfluidic fuel cells [43], or integrated cooling in electrical systems [26]. With the method presented in this thesis, the computation of flow rates is decoupled from the the finite element mesh that is used to compute the temperatures. Flow is confined to the channel segments that make

up the ground structure. A projection step is necessary to map the channel geometry and fluid velocities to the finite element mesh; an idea illustrated in Figure 1.2. This approach simplifies the computation of the fluid flow by restricting the problem to the ground structure, and can provide valuable computing speed gains while also allowing certain constraints to be implemented more easily.

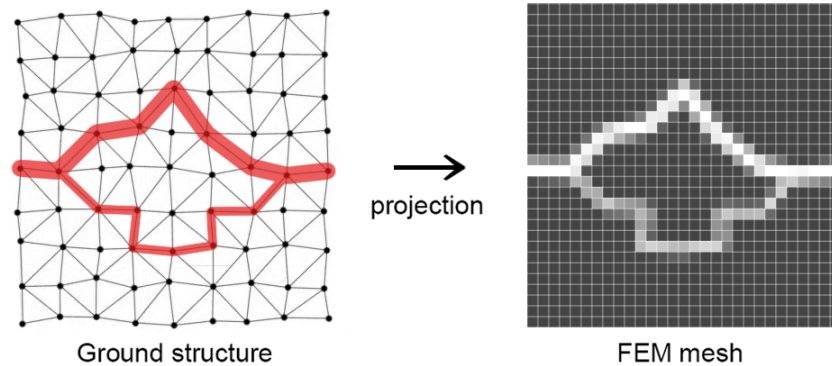


Figure 1.2: Fluid channel geometry is projected onto a structured grid FEM mesh. The original ground structure composed of a pipe flow network is seen on the left. The technique of projecting geometry onto a mesh is known as “geometry projection” [8, 54].

Another important motivation for this thesis concerns the thermomechanical distortions of mirrors in state of the art photolithography machines by ASML. Photolithography is a step in the process of fabricating computer chips where geometric patterns are transferred from a photo mask to a light sensitive substrate (also known as a wafer) to create integrated circuits. In the latest photolithography machines this is done with Extreme Ultraviolet (EUV) radiation. Figure 1.3(a) shows the size of an ASML EUV machine: the EUV radiation is illustrated with the purple beams in the center of the image. In EUV photolithography machines, a high power laser beam is used to vaporize tin droplets to create EUV radiation. After the EUV beam reaches the mask, the beam is further guided towards a silicon wafer by highly reflective mirrors in a so called Projection Optics Box (POB), see Figure 1.3. The POB mirrors are polished to *sub* nanometer accuracy [91]. Despite this, the mirrors still absorb a significant amount of EUV radiation which results in unwanted thermal distortions. Cooling channels can be implemented in the back side of the mirror to remove heat, but unfortunately surface deformations still occur. The deformations induced by the heat load cause the EUV beam to go out of focus and degrade the performance. By using thermofluid TO to design an optimized cooling channel layout, the unwanted thermomechanical distortions can potentially be reduced.

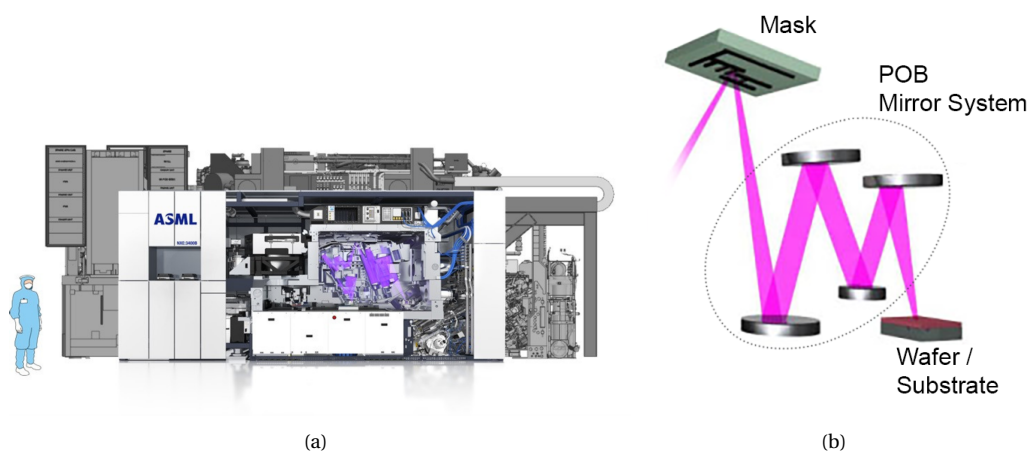


Figure 1.3: Left: a modern EUV photolithography machine from ASML. Right: a schematic depiction of the mirrors guiding the EUV beam.

## 1.2. Research goals and scope

The aim of this research is twofold: 1. to create a thermofluid TO method for initial design purposes that significantly reduces computation time for problems in the creeping flow regime; and 2. to apply thermofluid TO to an industrial optical instrument in order to reduce thermomechanical distortions. This is accomplished by synthesizing existing knowledge and methods to develop a new TO method that is subsequently applied to an industrial optical instrument.

The thermofluid TO method presented in this thesis is applicable to problems within or near the creeping flow regime. The goal is to develop a method that is able to generate optimized designs which may require further refinement. As such, the method is intended for initial design purposes as opposed to high accuracy simulations. The models used are not concerned with accurate representation of physical phenomena (i.e. temperature distribution or flow patterns) at length scales significantly below the fluid channel width. Temperature distribution results across the design domain within 10% of commercial FEM results are desirable. All domains that are optimized are 2-D, however a hybrid model is also shown where the optimized 2-D channels are coupled to the temperature distribution in a 3-D domain. Furthermore, all simulations are restricted to the steady state regime.

Possible applications for the research in this thesis are problems that involve cooling channels in general, and more specifically, problems with unwanted thermomechanical deformations. Other potential applications can be found in the field of microfluidics where numerous problems exist that deal with creeping flow, thin channels, and advection-diffusion phenomena.

## 1.3. Thesis outline

The thesis is divided into two parts. In Part I, a new thermofluid TO method is presented, from here on referred to as the Ground Structure Projection (GSP) method<sup>1</sup>. First, background information is provided and fundamental concepts are explained. This is followed by an extensive presentation of the method, validation and optimization examples, and finally discussion on the benefits and limitations.

In Part II, the GSP method is applied to an industrial problem where a cooling channel layout has to be designed to minimize thermomechanical distortions in an optical instrument (a POB mirror). The context for the case is presented and relevant background information is provided, after which a hybrid 2-D / 3-D model is introduced which is validated and used in the optimization problem.

The thesis is concluded with a section on conclusions and recommendations. Results are summarized and discussed, and recommendations on future work for the GSP method and the POB mirror are listed.

---

<sup>1</sup>During the research performed for this master's thesis it came to the attention of the author that a topology optimization method with a similar name (projection-based ground structure method (P-GSM)) was presented in 2020 by Deng and To [23]. However, the P-GSM method is only concerned with structural topology optimization and not with thermal or fluid physics.



# I

## A ground structure based topology optimization method for thermofluid problems

Part I of the thesis introduces the GSP method. In Chapter 2, the relevant background information and fundamental concepts will be explained. Chapter 3 provides an extensive description of the GSP method. In Chapter 4, a number of example optimization results are shown which involve a flow divider, a pressure drop minimization, and a heat sink like device. Finally, in Chapter 5 the benefits and limitations of the GSP method are discussed.



# 2

## Background information

This chapter provides the reader with fundamental concepts that are essential building blocks for the GSP method. Different methods of topology optimization are introduced, as well as fluid channel and thermofluid topology optimization with examples from literature. The last section (2.4) introduces a new aspect of the GSP method, named “velocity mapping”, and therefore serves as a bridge to Chapter 3 where the GSP method is described in detail.

### 2.1. Gradient based topology optimization

Topology optimization (TO) is a mathematical method that systematically generates an optimized design for the material layout and shape of an object, given a certain performance objective, constraints, and boundary conditions. The word topology indicates that the algorithm or optimizer not only improves a given shape, but can also come up with a new material layout or “topology”, e.g. making holes in a physical object would constitute a change in its topology.

Gradient based methods rely on the use of gradients, or derivatives, to find a minimum/maximum of the objective. Popular gradient based methods include the density-based method, the ground structure method, and the level set method [4]. The general structure of a gradient-based optimization loop can be seen in Figure 2.1. A model (often FEM) is used to evaluate the performance of the current design variable configuration. After this, the design sensitivities are computed, which are fed into the optimization algorithm. Every iteration a convergence check is done on the design variables to decide whether to continue or end the optimization loop.

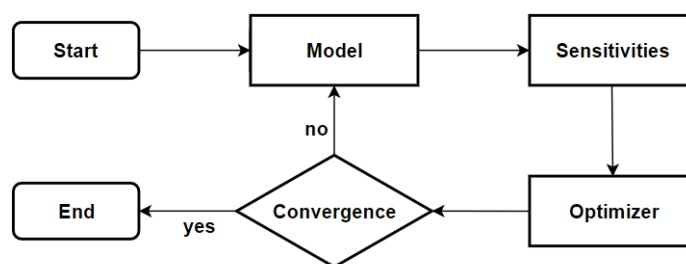


Figure 2.1: Simplified representation of a gradient based optimization loop.

#### 2.1.1. Density-based method

The density-based method was first proposed by Bendsoe in 1989 [10] and is the most widely used TO method. With the density-based method, the initial physical domain consists of a grid of material elements each with their own density as a design variable. Since an actual physical topology either has material in a certain place or is void, this would translate to a discrete problem and consequently no gradients can be calculated. Therefore, the design variables are made continuous, ranging from zero to one. With finite element analysis, the objective function is evaluated and the sensitivities of the objective function and constraints with regards to the design

variables are calculated and used by an algorithm which will subsequently determine how to progress towards an optimum.

### Penalization

An important aspect of the density-based method is the need to penalize intermediate densities. The optimal design often has intermediate densities, but a practical design should be manufacturable and cannot contain intermediate densities. Several methods exist to avoid this problem. The most obvious is to add an extra term to the objective function that increases for intermediate densities anywhere in the design domain, i.e. gray penalization [11]. It is often wise to start the optimization process without gray penalization to avoid getting stuck in an inferior local minimum. A disadvantage of this approach is that it is not always clear exactly when the gray penalization should start influencing the optimization process.

Another option is to artificially “weaken” elements with intermediate densities. In the case of compliance minimization this usually means that the Young’s modulus of the material decreases disproportionately for intermediate densities. The most well known example of this is Solid Isotropic Microstructure with Penalization (SIMP) proposed by Bendsoe in 1989 [10]. The idea is to make the element Young’s modulus  $E$  a function of the density  $\rho$  in a nonlinear fashion, i.e.  $E_i = \rho_i^p E_0$ ; see Figure 2.2a. The consequence is that intermediate densities will be unfavorable when there is a mass constraint or an objective that minimizes mass.

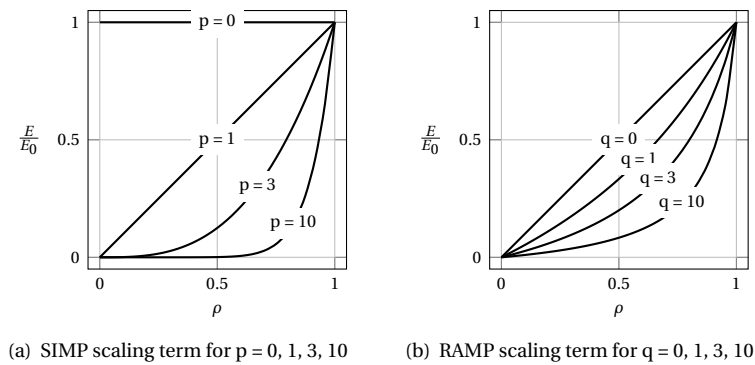


Figure 2.2: Young’s modulus as a function of density. Left using SIMP; right using RAMP.

A similar method used is Rational Approximation of Material Properties (RAMP), proposed by Stolpe and Svanberg in 2001 [76]; see Figure 2.2b. The RAMP method also adjusts the element Young’s modulus as a function of the density, however the relation is now defined as  $E_i = E_0 \frac{\rho_i}{1+q(1-\rho_i)}$ . The advantage of RAMP penalization is a nonzero tangent of the penalization function at zero density, which preserves sensitivity information at low densities. Apart from the previously mentioned penalization methods several other methods exist to interpolate material properties [69].

### Density filtering

A further important aspect in density based TO is the filtering or “blurring” of densities. Without density filtering, results will often exhibit “checkerboarding” patterns of alternating void and full density elements, see Figure 2.3(a). Checkerboarding artifacts are the result of numerical instabilities and are not optimal [25]. When density filtering is applied, the density of a single element will be the weighted average of surrounding element densities. Usually, the weights assigned to surrounding element densities decline linearly with radial distance. See Figure 2.3(b) for a result with density filtering.

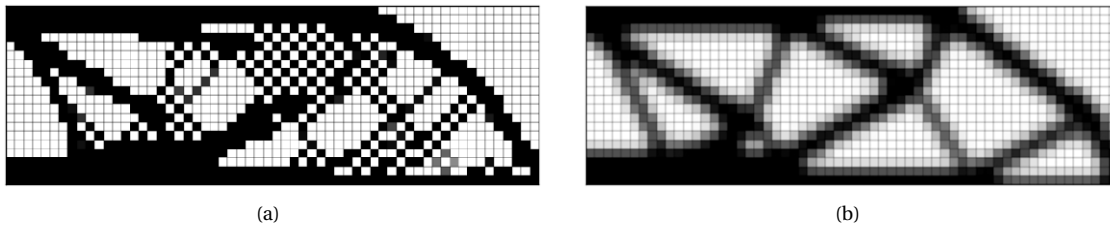


Figure 2.3: Checkerboarding artifacts in (a) are removed by applying density filtering in (b).

Density filtering will remove checkerboarding artifacts and guarantees a minimum feature scale. However, the resulting topology will be blurred and gray at the edges. To improve this, it is possible to apply an additional projection that makes the edges more pronounced [34]. A smoothed, differentiable Heaviside step function can be used to map the intermediate design variables  $\rho$  to the final design variables  $\tilde{\rho}$ :

$$\tilde{\rho} = \frac{\tanh(\beta\eta) + \tanh(\beta(\rho - \eta))}{\tanh(\beta\eta) + \tanh(\beta(1 - \eta))}$$

where  $\eta$  is the threshold parameter, and  $\beta$  controls the smoothness of the step function [84]. Figure 2.4 shows the function for  $\eta = 0$  and different values of  $\beta$ .

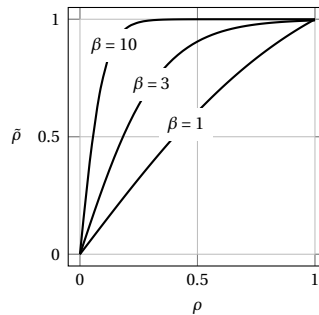


Figure 2.4: Smoothed Heaviside threshold functions to map intermediate densities  $\rho$  to final densities  $\tilde{\rho}$ .

### 2.1.2. Ground structure TO

The ground structure method works by removing or adding parts to a larger structure that consists of a number of sub-elements. It was first proposed by Dorn et al. [29] in 1964 who applied it to truss structures. Soon hereafter, the method was extended to more complicated problems with multiple load cases, self-weight, joint costs, etc. [37, 58]. As an example, take the case of minimizing compliance of a beam as seen in Figure 2.5. The beam starts out as a highly interconnected set of trusses: the so called ground structure. A constraint is imposed that restricts the allowed mass or volume. The design sensitivities with regards to the cross sections of the trusses are derived, and the TO algorithm can use these sensitivities to progress towards an optimum.

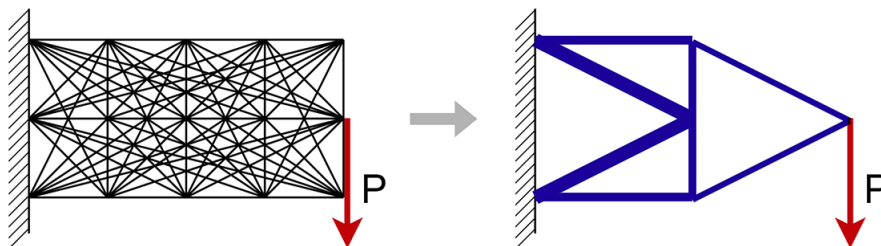


Figure 2.5: Left: the full ground structure and load  $P$ . Right: a structure optimized for minimal compliance subject to mass constraints [88].

### 2.1.3. Feature mapping

A relatively recent development in TO is known as feature mapping. Feature mapping, also referred to as geometry mapping or explicit TO, involves a combination of an explicit geometry description and a structured analysis grid (also called Ersatz material model) onto which the geometry is mapped/projected to evaluate performance. In general, the mapping can be done either by using pseudo densities in a pixel/voxel grid, or with an immersed boundary approach using techniques such as the extended finite element method (XFEM) to capture shape boundaries and discontinuities [81]. Examples of feature mapping methods are Moving Morphable Components (MMC) and Moving Morphable Voids (MMV). MMC was first proposed by Guo et al. [35] in 2014, and works by starting with a number of primitive components that can be moved and morphed into an optimized structure. Each iteration, the optimization algorithm will adjust the position, orientation, and shape of these components to improve the objective. The structure formed by the components is projected onto a finite element model to evaluate the performance. Analogous to MMC, there is MMV (Moving Morphable Voids) [94]. The components are now replaced by holes/voids which are optimally placed in a block of material. Figure 2.6 illustrates the basic principle of the MMC method. The main advantage of feature mapping methods is the explicit control over the geometry. For example, a minimum or maximum feature width constraint is trivial to implement.

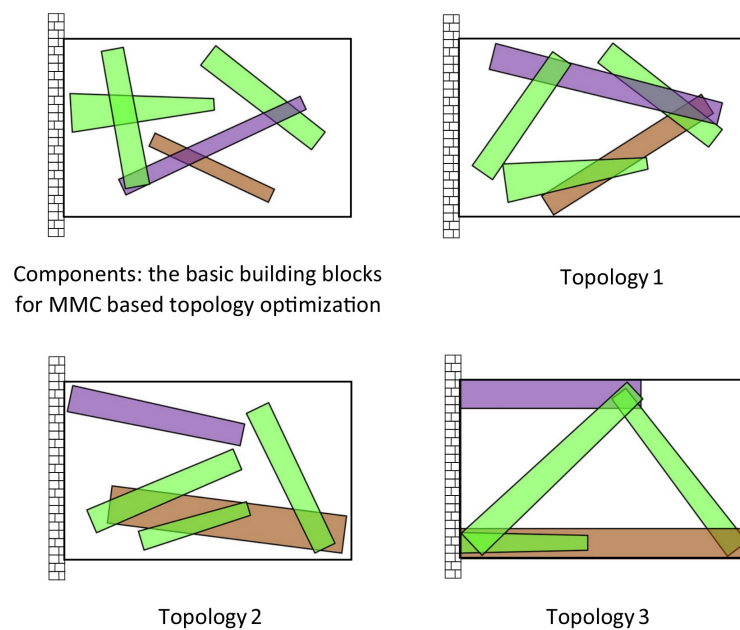


Figure 2.6: Basic idea behind the MMC method [93]. The initial topology consists of a number of components which subsequently morph and move into other, more optimal, positions. Topology 1, 2 and 3 correspond to advancing iterations of the optimization algorithm.

### 2.1.4. Algorithms for gradient based TO

A wide variety of algorithms exist to solve gradient based optimization problems, see for example [73]. The most commonly used methods in literature are approximation based algorithms where the actual response surface and constraints are approximated with linear or quadratic sub-problems. A popular method for density based TO is the Method of Moving Asymptotes (MMA) where strictly convex approximations of the objective function and constraints are made by using rational functions [79].

The TO problems in this thesis are solved using Matlab's built-in *fmincon* optimization function. The default interior point algorithm [65] is used, which generates a sub-problem in each iteration with inequality constraints incorporated using slack variables and a barrier function. This sub-problem is solved using either a second order approximation of the problem (i.e. a Newton step), or if this fails, with a conjugate gradient step. A detailed description of the specific implementation of the interior point method can be found in Matlab's documentation [51].

## 2.2. Fluid channel topology optimization

In the field of fluid mechanics, shape optimization techniques have been applied to applications such as minimum-drag profile design in laminar flows, by Pironneau [62] amongst many others. Research has also been done on the topology optimization of fluid channels. Various methods have shown to produce results for all sorts of applications. This section gives a brief overview of the fundamental concepts in fluid channel TO which include the governing physics and currently used methods of fluid channel TO.

### 2.2.1. Governing equations of fluid dynamics

Several computational methods exist that accurately model fluid dynamics. The governing physics of fluid dynamics are described by the Navier-Stokes equations:

$$\nabla \cdot \mathbf{v} = 0 \quad (\text{conservation of mass}) \quad (2.1)$$

$$\frac{D\mathbf{v}}{Dt} = \mathbf{g} - \frac{1}{\rho} \nabla p + \nu(\nabla^2 \mathbf{v}) \quad (\text{conservation of momentum}) \quad (2.2)$$

where  $\mathbf{v}$  is the velocity vector,  $\mathbf{g}$  body forces (only gravity in this case), and  $\nu$  the kinematic viscosity. The left hand side term in Equation 2.2 represents the material derivative of the velocities (i.e.  $\frac{D\mathbf{v}}{Dt} := \frac{\partial \mathbf{v}}{\partial t} + \mathbf{v} \cdot \nabla \mathbf{v}$ ), and hence contains time dependent and inertial effects. The research in this thesis focuses on steady state flow in the Stokes or creeping flow regime. Stokes flow concerns flow with a Reynolds number of  $Re \ll 1$ . When the Reynolds number is significantly smaller than one, the inertial effects on the flow will be negligible. If, in addition to this, the flow is steady state, the Navier-Stokes equations can be rewritten such that the entire material derivative on the left hand side of eq. (2.2) disappears [28]. The resulting equations describe Stokes or creeping flow:

$$\mathbf{0} = \mathbf{g} - \frac{1}{\rho} \nabla p + \nu(\nabla^2 \mathbf{v}). \quad (2.3)$$

Furthermore, for long cylindrical pipes and laminar flow, an analytical solution for the full Navier-Stokes equations is given by the Hagen-Poiseuille equation:

$$\Delta p = \frac{8\mu L q}{\pi r^4}, \quad (2.4)$$

which gives a direct relationship for the pressure drop  $\Delta p$  and the flow rate  $q$ , for a given dynamic viscosity  $\mu$ , channel length  $L$ , and channel radius  $r$ .

### 2.2.2. Density based fluid channel TO

Borvall and Petersson [13] have shown a fluid TO method similar to the density based method used in solid mechanics. In the method presented by Borvall and Petersson, the fluid flow throughout the entire domain can range continuously from full Stokes flow to Darcy flow. Here, Darcy's law describes the movement of fluids through porous media:

$$q = -\frac{k}{\mu} \nabla p, \quad (2.5)$$

where  $q$  is the fluid flux (flow per unit area),  $k$  the permeability of the porous medium,  $\mu$  the dynamic viscosity, and  $p$  the pressure. The interpolation between Stokes flow and Darcy flow is done by introducing a parameter  $\alpha(\rho)$  as a function of the densities. Combined with proper constraints and an objective that favors low power dissipation of the flow, the optimization algorithm will produce designs that minimize restrictions on flow. While the work done by Borvall and Petersson is restricted to Stokes flow, Gersborg-Hansen et al. [31] extended this work to also include problems with higher Reynolds numbers in which inertial effects are important. This can be seen in Figure 2.7. On the left is creeping flow with  $Re = 0$ . Inertial effects start to play a role with higher Reynolds numbers; at  $Re = 850$  the optimal fluid channel topology is curved as a result of the inertia of the fluid flow.

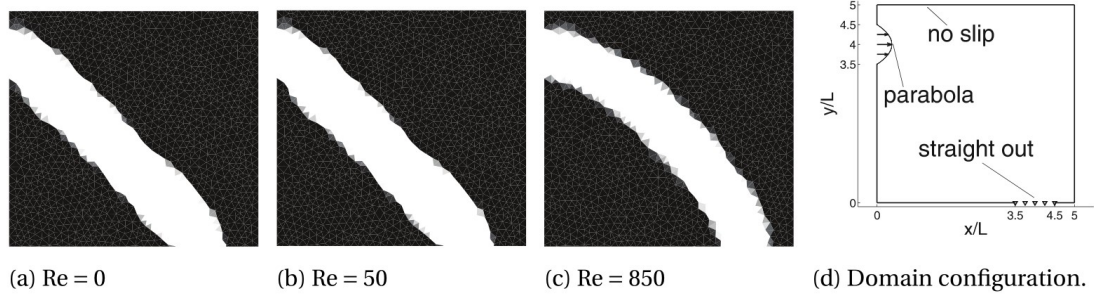


Figure 2.7: Comparison of flow restriction minimization for varying Reynolds numbers, from by Gersborg-Hansen et al. [31]. Channels are represented in white, impermeable regions in black.

An example of density based TO to generate a fluid channel network can be found in work by Zhou et al. [97]. Again, the type of flow is interpolated between the Navier-Stokes equations and Darcy's law for porous media. A comparison was made with an electric circuit analogy design method, which can be seen in Figure 2.8. In the electric circuit analogy, the required pressure drop is attained by varying the length and hence the resistance of channels.

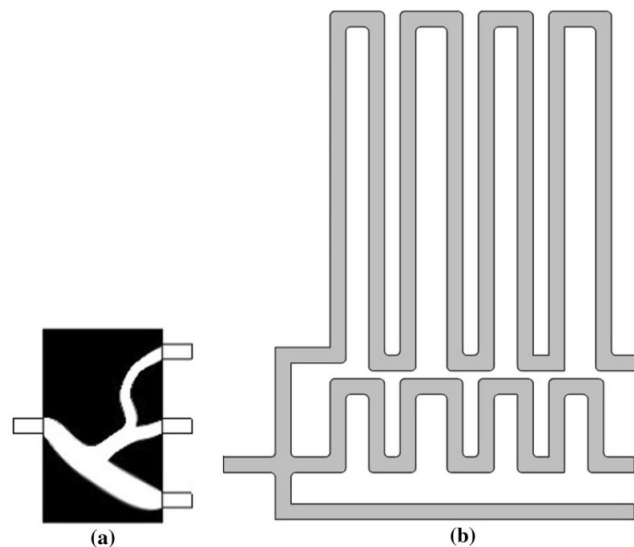


Figure 2.8: Comparison between gradient based TO (a), and a manual design method based on the electric circuit analogy (b) [97].

### 2.2.3. Other fluid channel TO methods

Aside from density based TO, other methods to perform fluid channel TO have also been investigated. Klarbring et al. [44] have applied a ground structure approach to the topology optimization of flow networks. This approach is similar to a truss structure for solid mechanics. For each truss, or channel segment in this case, the design variable is the cross sectional area. A pipe flow network model was used governed by Hagen-Poiseuille flow. The objective of the optimization was to minimize a measure that translates to dissipation or pressure drop. An example result can be seen in Figure 2.9. First a ground structure is created by generating a randomly distributed set of nodes, which are only connected to neighbouring nodes. Then, a pressure was prescribed to the top node, and uniform outflow was prescribed to 499 other nodes. Poiseuille flow and a ground structure have also been applied in conjunction with a genetic algorithm by Aragón et al. [6].

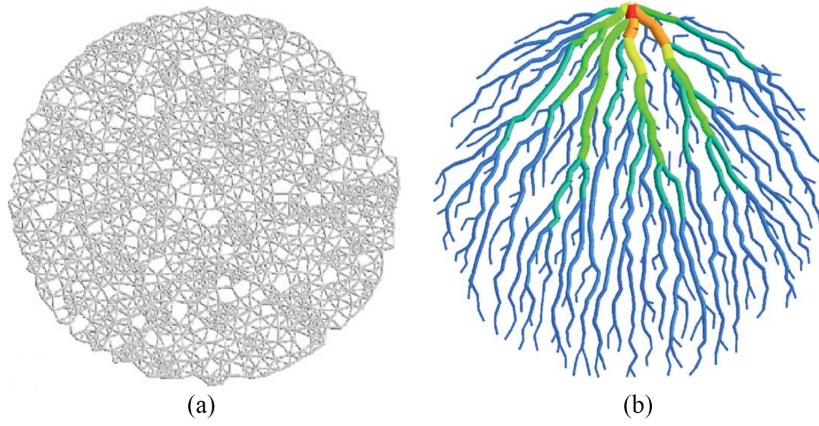


Figure 2.9: Ground structure (a) and optimized result (b) for an arterial tree-type two-dimensional network [44].

## 2.3. Thermofluid topology optimization

Calculating the effects of the flow velocities on the temperature distribution in a domain is done with the advection-diffusion equation:

$$\rho(\mathbf{x}) C(\mathbf{x}) \frac{\partial T}{\partial t} = \nabla \cdot (\boldsymbol{\kappa} \nabla T) - \rho(\mathbf{x}) C(\mathbf{x}) (\nabla \cdot (\mathbf{v} T)) + s \quad (2.6)$$

This equation, sometimes also called the convection-diffusion equation, represents the thermal energy balance in a system with conductive and convective heat transfer. The left hand side contains the volumetric rate of change of energy at any point  $\mathbf{x}$  in the system, with  $\rho(\mathbf{x})$  being the local density, and  $C(\mathbf{x})$  the local specific thermal capacity. The right hand side consists of a conduction term, a convection term, and a source term  $s$ . The convection term describes the transport of thermal energy through bulk movement of fluid, where  $\mathbf{v}$  is the fluid velocity. When the fluid velocity is zero, the equation reduces to the basic thermal energy balance equation for diffusion. Note that the density  $\rho$ , and heat capacity  $C$  are dependent on coordinates  $\mathbf{x}$ , since the domain consists of both solids and fluids.

The discretization<sup>1</sup> of the advection-diffusion equation results in the following system of equations:

$$(\mathbf{K}_{T,d} + \mathbf{K}_{T,c}) \boldsymbol{\theta} = \mathbf{q}_T, \quad (2.7)$$

with a diffusion matrix  $\mathbf{K}_{T,d}$ , a convection matrix  $\mathbf{K}_{T,c}$ , temperature vector  $\boldsymbol{\theta}$ , and thermal load vector  $\mathbf{q}_T$ . In the following parts of this thesis the matrix  $(\mathbf{K}_{T,d} + \mathbf{K}_{T,c})$  will simply be denoted with  $\mathbf{K}_T$ .

### 2.3.1. Stabilization

An important factor in solving the advection-diffusion equation is the dimensionless Péclet number:  $Pe = \frac{L_c v \rho C}{\kappa}$ , where  $L_c$  is a characteristic length scale,  $v$  the fluid velocity,  $\rho$  density,  $C$  thermal capacity, and  $\kappa$  the thermal conductivity. In situations where some physical quantity is being transported by flow, the Péclet number represents the ratio of advective transport to the rate of diffusive transport. In the case of this thesis the physical quantity is heat. Difficulties arise when the Péclet number is bigger than one, i.e. the advection dominates. The truncation error in the standard Galerkin discretization method will then lead to oscillations in the solution. An example of this can be seen in Figure 2.10. In this example, the model problem can be written as:

$$v \frac{dT}{dx} - \alpha \frac{d^2 T}{dx^2} = s(x) \quad \text{in } ]0, L[ \quad (2.8)$$

$$T = 0 \quad \text{at } x = 0 \text{ and } x = L, \quad (2.9)$$

where eq. (2.8) is the scalar advection-diffusion equation with  $T$  the temperature,  $v$  the advection velocity,  $\alpha$  the diffusivity constant, and  $s$  a source heating term. For  $L = 1$  and a uniform source term of  $s = 1$ , solutions

<sup>1</sup>See Zienkiewicz [98] or Donea and Huerta [28] for a step by step derivation.

are plotted for different Péclet numbers. The mesh Péclet number is:

$$Pe = \frac{vh}{2\alpha}, \quad (2.10)$$

with  $h$  being the element size. Figure 2.10 clearly shows oscillations for  $Pe > 1$ . One remedy for this problem is to add an extra stabilization term to the discretized system of equations that adds artificial thermal diffusion in the streamline upwind direction. For more details, see for example Donea and Huerta [28].

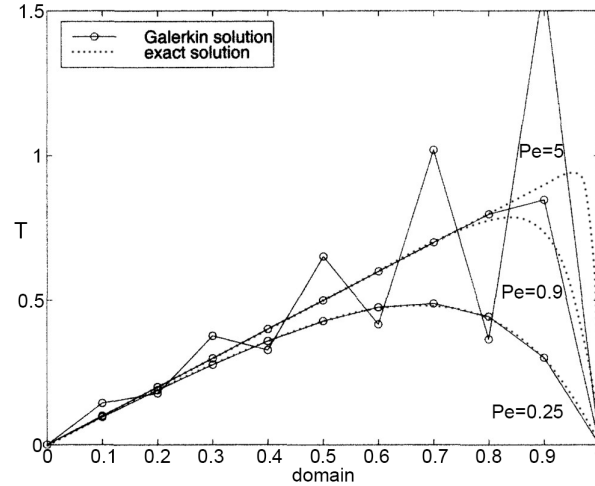


Figure 2.10: Example of oscillations in advection-diffusion solutions for high Péclet numbers [28]. The 1-D domain consists of 10 elements and is subject to a uniform source heating term. For  $Pe > 1$  oscillations will occur in the Galerkin solutions of transported physical quantity  $T$ .

Unfortunately, this streamline upwind (SU) scheme is not always sufficient. In Part II of this thesis, a case is described where cooling channels run through a glass like material with very low thermal conductivity. This situation is highly sensitive to the oscillations described above, and hence a second stabilization term is applied that adds a degree of crosswind diffusion [40, 78]. Diffusion orthogonal to the streamlines is added with a diffusivity coefficient  $\tilde{\alpha}$  such that:

$$\tilde{\alpha} = \max\{0, |v|h^{3/2} - \alpha\}, \quad (2.11)$$

where  $\alpha$  is the original diffusivity of the fluid, i.e.  $\frac{\kappa}{\rho C}$ ,  $h$  is the mesh element size, and  $v$  the local fluid velocity. More recent crosswind diffusion or “shock capturing” methods base the value of  $\tilde{\alpha}$  on the gradient of the temperatures  $\nabla T$ , and therefore are nonlinear [27]. Nonlinear methods can provide higher accuracy, however the linear method was chosen as to avoid the additional complexity associated with nonlinear FEM.

### 2.3.2. Examples from literature

The extension of topology optimization to thermofluid problems is a fairly recent one; next is a selection of work done on thermofluid TO. In 2009 Dede [21] coupled the commercial FEM package COMSOL with an MMA algorithm to optimize the topology of a heatsink-like device, see Figure 2.11. The two objectives were to minimize mean temperature in the domain, and secondly to minimize the pressure drop in the flow channels. Similarly, Yoon [89], also optimized the topology of a heat dissipating body, considering both laminar flow and thermal conduction and convection. In 2013, Matsumori [52] used density-based TO to design 2-D heat exchangers. Koga et al. [45] also used TO to develop 2-D heat sinks, but a subsequent 3-D simulation was done to evaluate the 2-D layout. A similar procedure was applied by Yaji et al. [85] using the level-set method.

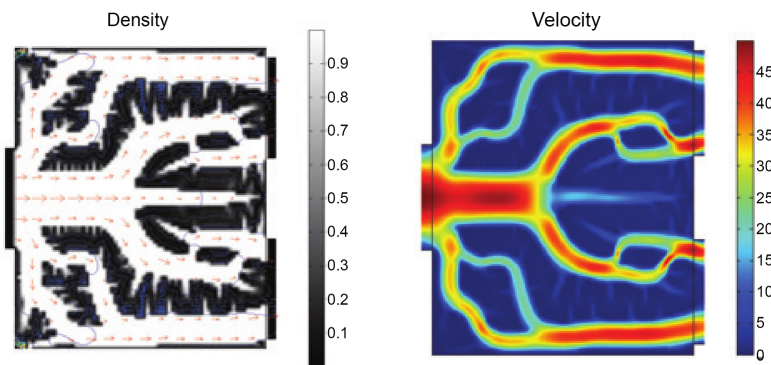


Figure 2.11: Thermofluid TO for minimum average temperature and pressure drop by Dede et al. [21]. Left the densities, right the flow velocities. Channels branch out across the domain to cool as much as possible.

In 2015, both Dede et al. [22] and Alexandersen et al. [3] applied full 3-D topology optimization to generate heat sink devices cooled by forced and natural convection respectively, see Figure 2.12(a). Yaji et al. [85] applied a level set TO method to the design of heat exchangers, shown in Figure 2.12(b). Pizzolato et al. [63] performed a full 3-D transient topology optimization of a heat exchanger used for Latent Heat Thermal Energy Storage, while Pietropaoli et al. [61] applied full 3-D TO to increase the performance of a turbulator device. Lastly, Yaji et al. [86] investigated large-scale TO for heat exchangers. Running bespoke Fortran code on a supercomputer at Nagoya University, a heat exchanger topology was optimized with a full 3-D transient model. The fluid dynamics were described by the Lattice-Boltzmann equation. The results feature highly complex configurations.

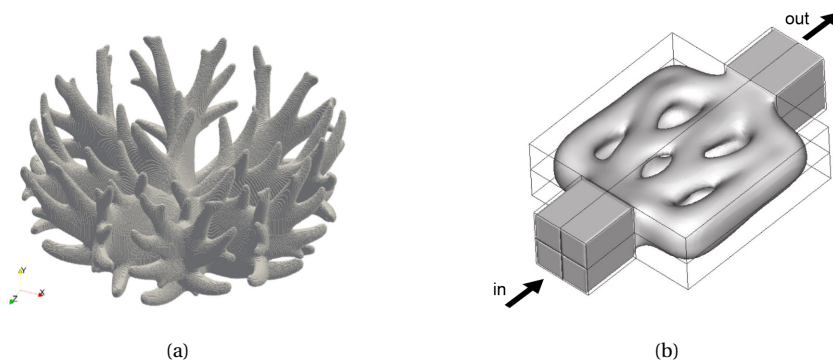


Figure 2.12: (a) A heatsink optimized to dissipate heat via natural convection from Alexandersen et al. [3] in 2016. (b) Design for a heat exchanger by Yaji et al. [85].

The general approach to thermofluid problems is to use a one way coupling from the fluid physics to the heat transfer physics. Depending on the Reynolds number and corresponding flow regime, the fluid velocity field is solved using a discretization of the full or simplified Navier-Stokes equations, or in some cases the Lattice Boltzmann method (LBM). As described in Section 2.3, the fluid velocity field at the nodes of the FEM mesh is used in solving the advection-diffusion equation, and the corresponding temperature distribution is found. In cases with natural convection, a two way coupling is required, as the temperature will also have an effect on the fluid movement [3].

## 2.4. Feature mapping in thermofluid topology optimization

Aside from (thermo)mechanical TO, feature mapping has also been used in thermofluid TO by Yu et al. [90] in 2019, utilizing the MMC method. Figure 2.13 shows a result from Yu et al. where thermal compliance and pressure drop are minimized. The fluid model is based on Darcy-Brinkman flow through porous media similar to examples shown in Section 2.2.2.

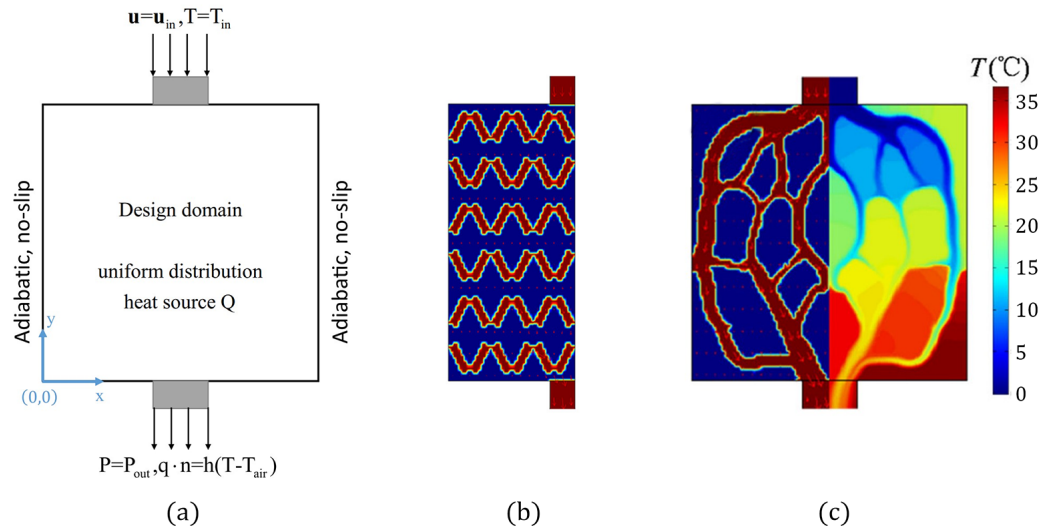


Figure 2.13: Thermofluid TO result from Yu et al. [90] using the MMC method. (a) shows the problem setup, (b) the initial layout of components (left/right symmetry), and (c) the resulting topology when optimized for minimal temperature and pressure drop.

The advantage in this approach mainly lies in the ability to control high level features of the topology, as explained in Section 2.1.3. However, since the fluid flow is still modeled using Stokes and Darcy flow, there are no computational speed gains in this area compared to density based TO.

### 2.4.1. Velocity mapping

The next chapter describes in detail the GSP method, a novel method for thermofluid TO in which the fluid channel topology is described by a ground structure of straight channels that is projected onto a structured grid FEM mesh. This method bears resemblance to feature mapping methods like MMC and MMV in the sense that a high-level topology is mapped onto a so called "Ersatz material model". Similar to MMC/MMV, the cavities or voids formed by the fluid channels are projected onto the structured FEM mesh. An important difference however, is that with the GSP method the layout remains fixed and only channel widths can vary.

The motivation for a ground structure based method was already briefly covered in the introduction. The aim in developing this method was to reduce the computation time compared to a pure density based approach. In density based thermofluid TO the solving of the pressures and fluid velocities is significantly heavier in terms of computation than the thermal physics, or mechanical physics if applicable. This holds true even when turbulence and inertial effects in the fluid flow are neglected. Using the new ground structure based method, computation time is reduced by simplifying the fluid flow problem. Instead of solving the Stokes equation with FEM, the flow velocities are now found by solving for the pressures in a network of straight channels with Poiseuille flow (i.e. fully developed pipe flow). This network consists of a connected graph where the pressures defined at the nodes/vertices are the degrees of freedom (DoFs) of the system. When the network flow is solved, the velocities are mapped to the FEM mesh similar to the density mapping. Depending on the resolution and "connectedness" of the ground structure, this can result in a significant reduction in the number of DoFs compared to the discretized Stokes equation where each node of the FEM mesh has at least three or four DoFs for a 2-D or 3-D model respectively. Additionally, the use of a high-level topology description allows for feature control benefits similar to other feature mapping methods.

# 3

## Description of the GSP method

This chapter provides a detailed explanation of the GSP (Ground Structure Projection) method. After giving an overview of the different steps in the GSP method routine in Section 3.1, the computing of the flow rates in a pipe flow network will be explained in Section 3.2. In Section 3.3 both the channel geometry and flow velocity projection will be discussed in depth.

### 3.1. GSP method routine

As already mentioned, the GSP method involves a combination of a fluid channel ground structure used to determine flow rates, and an FEM mesh that uses projected flow velocities in order to compute the resulting temperatures. This is best illustrated with Figure 1.2 where the ground structure is projected onto the structured grid FEM mesh, also called the “Ersatz material model” [4]. The projection step involves the use of analytical functions which are determined beforehand.

The entire optimization routine is shown in Figure 3.1 (extended from Figure 2.1). For each iteration of the optimization algorithm the model has to be evaluated to determine the current objective value and sensitivities. The cooling channel *half* widths, which are the design variables of the problem, are updated each iteration based on the design sensitivities. Given a new set of channel widths, the flow rate is calculated in all channels using the Hagen-Poiseuille law and a network flow representation of the channels. The next step is to project the flow velocities and material properties onto a structured grid finite element mesh. The performance is then evaluated by solving the discretized advection-diffusion equation, and the sensitivities are computed with the so called adjoint method.

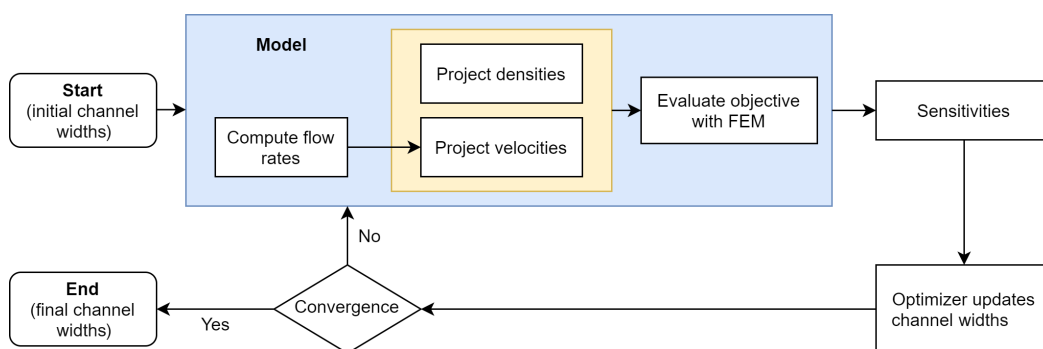


Figure 3.1: Schematic overview of the steps in the GSP method.

### 3.2. Computing flow rates

The first step in the process is to find the volumetric flow rate in all channel segments of the channel network. A network of channels can be represented by a circuit analogous to an electrical circuit. Similar to electric circuits, the flow and pressure drop in a pipe or channel network are governed by Kirchoff’s first and second law, which state respectively that: 1. The total flow into any junction equals the total flow out of that junction;

and 2. Between any two junctions, the pressure drop is independent of the path taken. For incompressible laminar flow, the Hagen-Poiseuille equation can be assumed, which describes the relation between pressure drop and flow rate in a long cylindrical pipe of constant cross section. Based on this relation, a system of linear equations can be set up. The system of equations in Eq. 3.1 describes the flow in the simple network of Figure 3.2. Here  $\mathbf{B}$  is a matrix describing the connectivity between the nodes and pipe sections,  $\mathbf{D}$  is a diagonal matrix containing the pipe conductivities (reciprocal of hydraulic resistance, i.e.  $d_i = \frac{\pi r_i^4}{8\mu L_i}$ ), vector  $\mathbf{p}$  contains the pressures, “load vector”  $\mathbf{q}_F$  represents the flow entering or leaving the network at each node, and finally  $\mathbf{q}_c$  are the flow rates inside the channels. After applying boundary conditions to obtain  $\tilde{\mathbf{K}}_F$  and  $\tilde{\mathbf{q}}_F$ , the pressures are found by solving for  $\mathbf{p} = \tilde{\mathbf{K}}_F^{-1} \tilde{\mathbf{q}}_F$ , and the channel flow rates can be found subsequently by taking  $\mathbf{q}_c = \mathbf{DBp}$ .

$$\underbrace{\begin{bmatrix} 1 & 0 \\ -1 & 1 \\ 0 & -1 \end{bmatrix}}_{\mathbf{K}_F := \mathbf{B}^T \mathbf{D} \mathbf{B}} \underbrace{\begin{bmatrix} d_1 & 0 \\ 0 & d_2 \end{bmatrix}}_{\mathbf{D}} \underbrace{\begin{bmatrix} 1 & -1 & 0 \\ 0 & 1 & -1 \end{bmatrix}}_{\mathbf{B}} \underbrace{\begin{bmatrix} p_1 \\ p_2 \\ p_3 \end{bmatrix}}_{\mathbf{p}} = \underbrace{\begin{bmatrix} 1 & 0 \\ -1 & 1 \\ 0 & -1 \end{bmatrix}}_{\mathbf{q}_F} \underbrace{\begin{bmatrix} q_{c,1} \\ q_{c,2} \end{bmatrix}}_{\mathbf{q}_c} \quad (3.1)$$

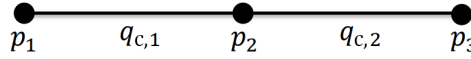


Figure 3.2: A very simple flow network of two pipe/channel segments and three nodes. Pressures  $p_1, p_2, p_3$  are evaluated at the nodes. The flow rates in the channel segments are represented by  $q_{c,i}$ .

Since the GSP method is still restricted to 2-D, the channels can be seen as having a constant width throughout the depth dimension. For this reason, a slightly modified version of the Hagen-Poiseuille equation was used [70] which describes flow and hydraulic resistance in pipes with rectangular cross section:

$$q_c = \left[ 1 - 0.63 \frac{h}{w} \right] \frac{h^3 w}{12\mu L} \Delta p, \quad (3.2)$$

where  $w$  is the channel width,  $h$  the channel height,  $\mu$  the dynamic viscosity, and  $L$  the channel length.

### 3.3. Projection onto FEM model

The material properties and fluid flow rates have to be transferred to an FEM model in order to calculate the final temperature distribution. To do this, the material properties and flow velocities are mapped or projected onto a structured grid mesh via analytical functions that relate a given channel's location, orientation, width, and flow rate to density values and velocity values for nearby elements.

#### 3.3.1. Channel geometry projection

The channels of the ground structure must be represented by the density distribution of the FEM mesh. To determine the densities of the elements in the FEM model there needs to be a set of analytical functions that calculate the “coverage” of individual elements by channel segments of the ground structure. These functions have to be differentiable since they are used in a gradient based TO algorithm. This coverage value is dependent on the location, orientation, and width of the channels.

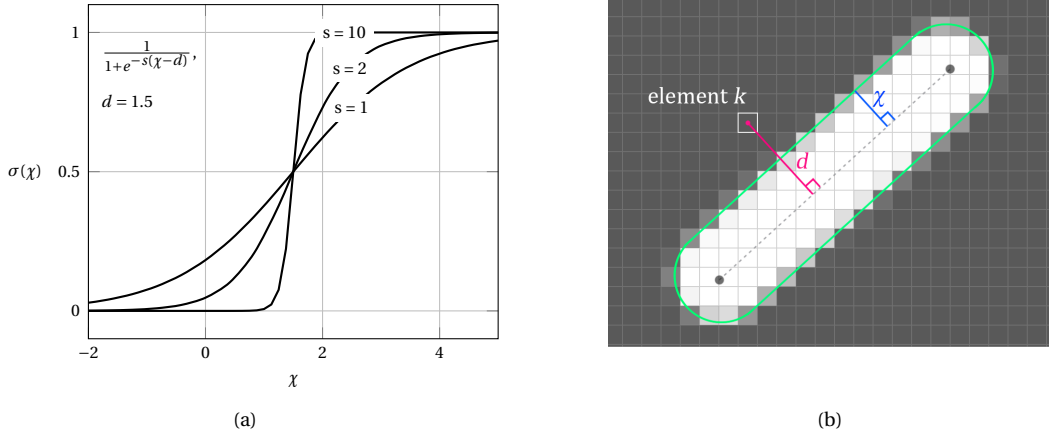


Figure 3.3: The sigmoid functions in (a) are used to map the channel geometry to individual element densities in (b). The value of  $d$  is determined beforehand, while  $\chi$  is a design variable optimized during the optimization routine. Since  $\chi < d$  in figure (b), the marked element  $k$  is not covered by the channel geometry.

Figure 3.3(b) shows the projection of a single channel segment. The shortest distance from the center line of the channel segment to the center point of a particular element is denoted by  $d$ , while  $\chi$  represents half the width of the channel segment. These quantities are used to determine the coverage of an element with the help of sigmoid functions. A predefined maximum channel width limits the area of influence of individual channel segments such that coverage is only computed for elements within this area. The sigmoid function  $\sigma(s(\chi - d)) = \frac{1}{1+e^{-s(\chi-d)}}$  gives a smoothed step function that tends to 1 for  $\chi > d$  and tends to 0 for  $\chi < d$ . The constant  $s$  is an external parameter that determines the sharpness of the sigmoid function, see Figure 3.3(a). A higher value of  $s$  will result in a projection with sharper edges, whereas a low value of  $s$  has a smoothing effect which reduces the aliasing or “staircasing” in diagonal edges. All results produced in this thesis were generated with an  $s$  value of 20, and millimeters as an internal length scale.

For a given channel segment with half width  $\chi_i$  and shortest distance  $d_{i,k}$  to some element  $k$ , the corresponding sigmoid function is

$$\sigma(s(\chi_i - d_{i,k})). \quad (3.3)$$

To ensure that the sigmoid function crosses zero, the function is adjusted slightly by subtracting its value at  $\chi_i = 0$ , i.e.  $\sigma(-sd_{i,k})$ . The function is subsequently divided by  $(1 - \sigma(-sd_{i,k}))$  to raise the righthand asymptote back to one, resulting in the coverage function for a single channel segment to a single element:

$$c_{i,k} = \frac{\sigma(s(\chi_i - d_{i,k})) - \sigma(-sd_{i,k})}{1 - \sigma(-sd_{i,k})}. \quad (3.4)$$

This coverage function has to be determined for every channel and corresponding nearby elements. However, at an intersection of channels there can be multiple channel segments overlapping on a single element. The maximum coverage of one element cannot exceed one, therefore all coverage values of the particular element are used as arguments in a smooth maximum function:

$$c_k = S_\alpha(c_{i,k}), \quad (3.5)$$

with  $S_\alpha$  defined as:

$$S_\alpha(y_1, \dots, y_n) = \frac{\sum_{i=1}^n y_i e^{\alpha y_i}}{\sum_{i=1}^n e^{\alpha y_i}}. \quad (3.6)$$

Finally, the element densities  $\rho_k$  are found by taking  $\rho_k = 1 - (1 - \varepsilon) \cdot c_k$ , where  $\varepsilon$  is a small number ( $\varepsilon \ll 1$ ) such that a minimum density of  $\varepsilon$  is guaranteed. The element density can then be used to interpolate material

properties such as the thermal conductivity  $\kappa$ .

The process of determining the coverage/density functions is done only once for a given ground structure and FEM mesh, before the optimization routine. Evaluating the functions to find the density values is done every iteration during optimization.

### 3.3.2. Velocity projection

Finding the element velocities is done in a similar way to the element densities. Based on the ground structure and FEM mesh, a set of analytical functions are generated that relate the location, orientation, and width of a given channel segment to a dimensionless velocity vector at the center of a nearby element. A dimensionless parabolic flow profile  $\tilde{f}_{nd}(d)$  is generated with a magnitude that ranges from 0 at the edges, to 1 in the center, while the width scales with design variable  $\chi$  such that  $\tilde{f}_{nd}(d) = 1 - (\frac{d}{\chi})^2$ . Negative values for  $|d| > \chi$  are removed by taking  $f_{nd} = \frac{1}{2}(\tilde{f}_{nd} + |\tilde{f}_{nd}|)$ . Figure 3.4 shows how this flow profile is overlaid on the channel and sampled at element center points. Analogous to the element densities which are multiplied with the thermal conductivity  $\kappa$ , the dimensionless element velocities are multiplied with the centerline flow velocity  $v_{max}$  in the corresponding channel.

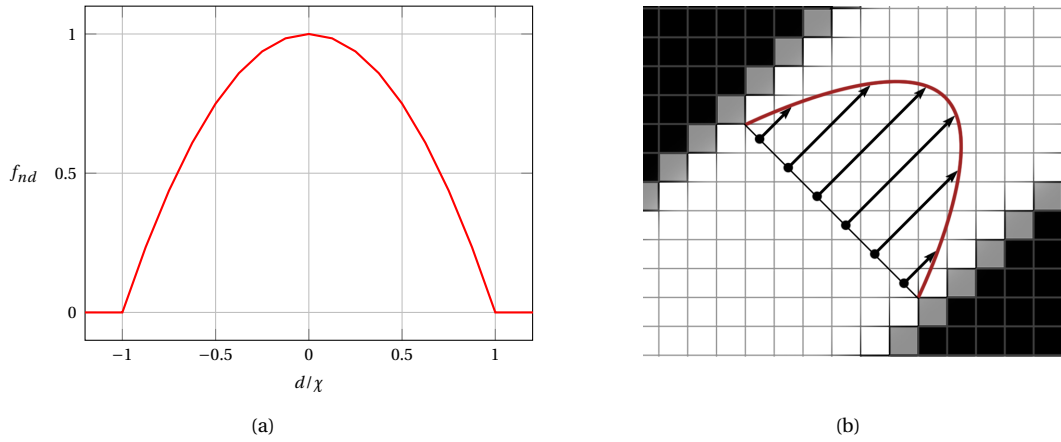


Figure 3.4: Projection of velocities. Figure (a) shows a dimensionless laminar flow profile. This flow profile is sampled at element center points in (b) to generate velocity vectors based on channel orientation and flow rate.

It should be noted that the assumption of a parabolic flow profile has its limits. In actual rectangular channels the flow profile is parabolic across the channel width if the channel aspect ratio is below one [66, 80], i.e. width is smaller than height. However, the shape of the flow profile will start to deviate from a parabola for aspect ratios above one; the flow profile will gradually “flatten”. This also means that  $\frac{v_{max}}{v_{avg}}$ , the ratio of centerline velocity to average velocity, changes for varying channel aspect ratios. For rectangular channels,  $\frac{v_{max}}{v_{avg}}$  ranges from 1.5 for very wide channels, to 2 for near square channels [38]. Given the geometry of the problems in this thesis, it is assumed that the majority of the projected channels are wide, i.e. a ratio of width to height above one. Consequently, for most channels,  $\frac{v_{max}}{v_{avg}}$  will be somewhere between 1.5 and 2. For this reason, a base ratio of  $\frac{v_{max}}{v_{avg}} = 1.5$  is used, after which a correction factor is applied to match the results of a commercial FEM package. The validity of the assumptions are tested in Chapter 4 on validation.

A heuristic approach is used to create smooth channel to channel transitions. When multiple channels cover a single element  $k$  at a channel junction, the resultant velocity  $\mathbf{v}_k$  is taken as the following weighted average:

$$\mathbf{v}_k = \frac{\sum_{i=1}^n (f_{nd,i} \cdot q_{c,i} \cdot \Phi_i) \cdot \mathbf{v}_{k,i}}{\sum_{i=1}^n (f_{nd,i} \cdot q_{c,i} \cdot \Phi_i)} \quad (3.7)$$

over all channel segments  $i$  that cover element  $k$ . The weights  $f_{nd,i}$ ,  $q_{c,i}$ , and  $\Phi_i$  serve different purposes. Using dimensionless velocity  $f_{nd,i}$  itself as a weighting factor causes high centerline velocities to be weighted stronger than slow boundary velocities; this ensures that centerline velocities remain high through strongly angled channel connections, see Figure 3.5(a). Channel flow rate  $q_i$  gives a stronger weight to channel segments with

a high flow rate, such that low flow side branches do not cause velocity “dips” in a high flow main branch. Finally, the weight  $\Phi_i$  is a custom value for which holds:

$$\Phi_i = \begin{cases} 1, & d_{\text{ext},i} = 0 \\ 1 - \frac{d_{\text{ext},i}}{\chi_i}, & 0 < d_{\text{ext},i} \leq \chi_i \end{cases}, \quad (3.8)$$

where the variable  $d_{\text{ext},i}$  denotes the extension beyond the outer ends of the channel segment, as illustrated in Figure 3.5(b): distance  $d_{\text{ext},i}$  is measured from the dotted line. When  $d_{\text{ext},i} = \chi_i$ , the outermost value for  $d_{\text{ext},i}$  is reached and  $\Phi_i$  is zero. Hence, weights  $\Phi$  reduce the influence of one channel segment on the next channel segment. An example where weights  $\Phi$  come into use is when a wide channel  $i$  transitions into a thinner channel  $j$  and flow velocities increase. Weights  $\Phi_i$  and  $\Phi_j$  then work together to create a linear interpolation between the velocities of the two channels. Figure 3.6 shows the corresponding resulting flow fields for both the angled and straight case. While the projected flow fields are visually smooth, there is still room left for improvement. For example, the upper right corner of Figure 3.6(a) shows flow with stream lines slightly deviating from the shape of the channel. Also, the straight channel transition in Figure 3.6(b) only features horizontally oriented velocity vectors, whereas in reality, flow would also move from the edges towards the center of the channel.

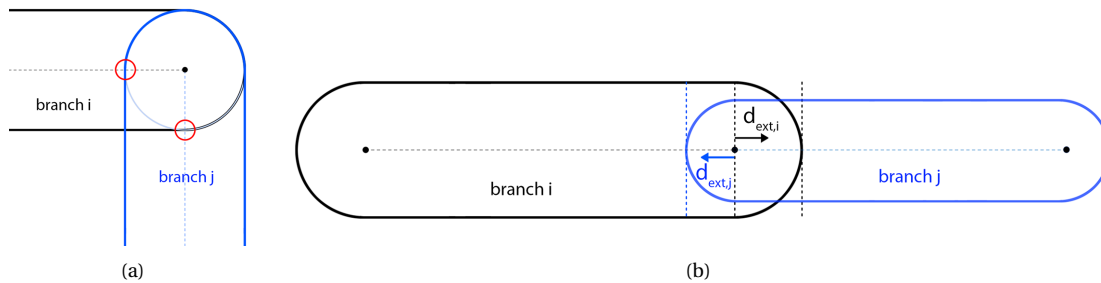


Figure 3.5: (a) Junction where channels are connected at an angle. Red circles highlight areas where both zero velocity and maximum velocity overlap. (b) Junction where a big and small channel meet. Variables  $d_{\text{ext}}$  represent the overlap of one channel onto the next, and are used to reduce the mutual influence of projected velocities.

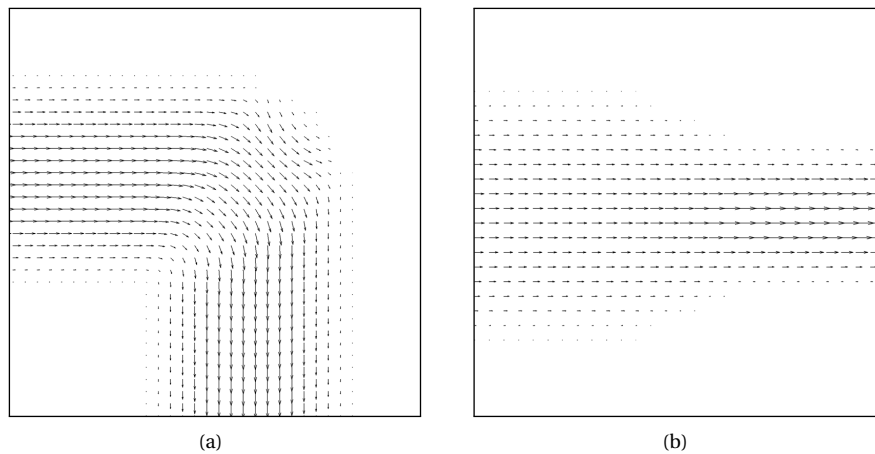


Figure 3.6: Projected flow fields corresponding to the two cases in Figure 3.5. (a) shows the flow field for a 90 degree angled junction, and (b) shows the flow field for a straight channel junction with decreasing channel width.

The following sections describe additional steps taken to further smoothen the velocity field and ensure local mass conservation. In Chapter 4, the end result of the projection procedure is validated with comparisons against a commercial FEM package. Furthermore, in Appendix C on Validation, additional examples are shown, including a visual example of projected velocity vectors for a Y-split channel layout.

### Thin channels

For very thin channels the projection can result in discontinuous flow due to aliasing artifacts. Figure 3.7 shows how the projection of a thin channel onto a structured grid can result in significant sampling artifacts. The red line represents a thin channel; when an element center point is nearby, the resulting projected element coverage will be higher. Since velocities are projected using the same basic idea, the artifacts are the same for the flow projection. This artifact will be most pronounced when a channel runs directly on top of a grid line of the FEM mesh. In such a situation, a channel that is too thin can result in zero flow being projected.

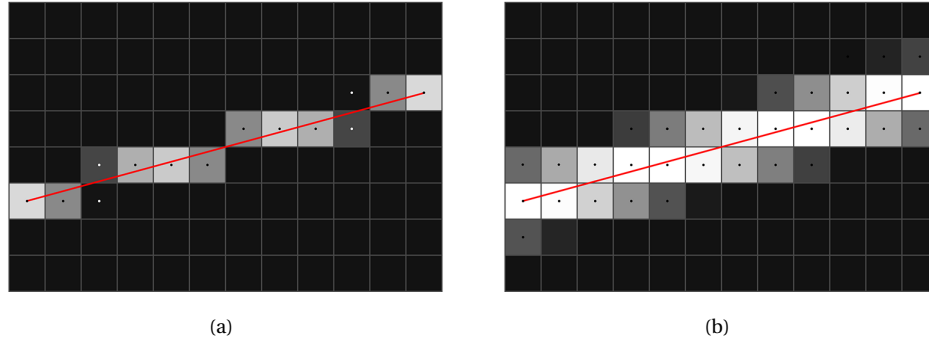


Figure 3.7: Projection of a thin channel causes density aliasing or discontinuous projection, visible in (a). When channel projection has a minimum width of two elements, the projection will be more consistent.

To ensure a continuous flow projection and a smooth objective response function, the minimum projected width of a channel is  $2h$ , where  $h$  is the mesh element height or width. Below this width, the flow is artificially restricted by multiplying the flow rate with a factor  $c_{\text{thin}} = \frac{w}{w+0.5h}$ , with  $w$  the actual channel width. Hence,  $c_{\text{thin}}$  will approach zero for very thin channels, thus reducing projected velocities.

### 3.3.3. Flow correction

As explained in previous sections, the velocities are projected onto the structured grid FEM mesh using *a priori* knowledge of laminar flow profiles. In contrast to a finite element based solver, this approach does not guarantee a continuous divergence-free flow field. Hence, the velocity mapping procedure can give nonphysical flow in certain areas, such as unwanted local sources or sinks. The previous section already showed artifacts for thin channels, but aliasing can occur at the outer edges of any diagonal channel. Apart from being nonphysical, discontinuities in the flow field can exacerbate oscillation issues described in Section 2.3.1. In addition to this, the flow velocities at junctions where channels overlap are not automatically projected correctly with Equation 3.7. To ensure a continuous, divergence-free velocity field, the projected velocities are corrected with additional operators.

The first operator is a heuristic “blurring” or “averaging” filter where each velocity vector is averaged with the surrounding velocity vectors. Used values were chosen to minimally alter the flow profiles, while still providing some smoothing effect on the velocity field. The following filtering kernel is used:

$$\begin{pmatrix} \frac{1}{40} & \frac{1}{40} & \frac{1}{40} \\ \frac{1}{40} & 1 & \frac{1}{40} \\ \frac{1}{40} & \frac{1}{40} & \frac{1}{40} \end{pmatrix},$$

such that the x and y-components of velocity vector  $\mathbf{v}$  are updated accordingly:

$$v_{x,i}^{\text{new}} = \frac{\sum_{j=1}^9 w_j v_{x,j}}{\sum w_j}, \quad (3.9)$$

where  $w_j$  are the values from the above filtering kernel. The same is done for  $v_y$ .

While the blurring filter already reduces the local divergence of the velocity field, a second operator is introduced to further reduce local divergence by applying the Helmholtz decomposition [32]. Helmholtz’s

theorem, also known as the fundamental theorem of vector calculus, states that any sufficiently smooth vector field  $\mathbf{v}$  can be decomposed as:

$$\mathbf{v} = \mathbf{a} + \nabla\phi, \quad (3.10)$$

where  $\nabla \cdot \mathbf{a} = 0$ , i.e.  $\mathbf{a}$  is divergence free, and  $\phi$  is a scalar potential function such that  $\nabla\phi$  is irrotational (curl free). The projection of the vector field  $\mathbf{v}$  onto its divergence free part  $\mathbf{a}$  is implicitly defined by applying the divergence operator to both sides of Equation 3.10:

$$\nabla \cdot \mathbf{v} = \nabla^2\phi, \quad (3.11)$$

which is a Poisson equation that can be solved (with given boundary conditions) for  $\phi$ , after which the divergence free field  $\mathbf{a}$  is found by taking  $\mathbf{a} = \mathbf{v} - \nabla\phi$ . This result can also be obtained by using a relaxation scheme where the velocity field is repeatedly incremented with the gradient of its divergence [16, 30]. Figure 3.8 shows nine cells of a 2-D grid where velocity vector  $\mathbf{v}$  is updated based on the divergence values at the surrounding corner nodes. For the purpose of compactness, velocity components  $v_x$  and  $v_y$  are temporarily denoted as  $u$  and  $v$  respectively, see Eq. 3.12.

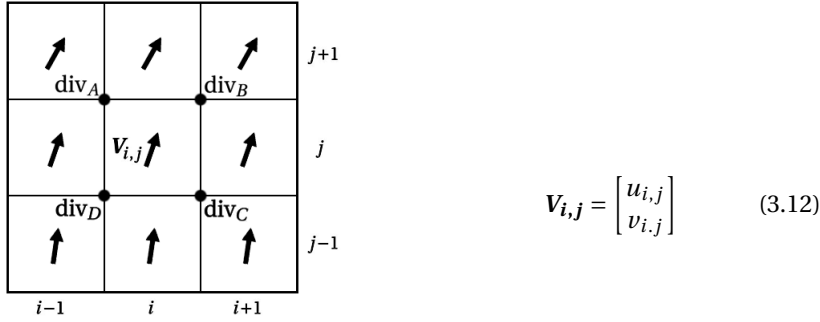


Figure 3.8: Divergence is calculated at four nodes around velocity vector  $\mathbf{v}_{i,j}$ . The divergence values are used to update  $\mathbf{v}_{i,j}$  and direct it towards a high divergence area.

The divergence values at the surrounding nodes are calculated as follows:

$$\begin{aligned} \text{div}_A &: (u_{i,j+1} + u_{i,j}) - (u_{i-1,j+1} + u_{i-1,j}) + (v_{i-1,j+1} + v_{i,j+1}) - (v_{i-1,j} + v_{i,j}) \\ \text{div}_B &: (u_{i+1,j+1} + u_{i+1,j}) - (u_{i,j+1} + u_{i,j}) + (v_{i,j+1} + v_{i+1,j+1}) - (v_{i,j} + v_{i+1,j}) \\ \text{div}_C &: (u_{i+1,j} + u_{i+1,j-1}) - (u_{i,j} + u_{i,j-1}) + (v_{i,j} + v_{i+1,j}) - (v_{i,j-1} + v_{i+1,j-1}) \\ \text{div}_D &: (u_{i,j} + u_{i,j-1}) - (u_{i-1,j} + u_{i-1,j-1}) + (v_{i-1,j} + v_{i,j}) - (v_{i-1,j-1} + v_{i,j-1}). \end{aligned}$$

The gradient vector of the divergence is then calculated as

$$\mathbf{g} = \begin{bmatrix} (\text{div}_B + \text{div}_C) - (\text{div}_A + \text{div}_D) \\ (\text{div}_A + \text{div}_B) - (\text{div}_D + \text{div}_C) \end{bmatrix}. \quad (3.13)$$

Each iteration  $\mathbf{g}$  is added to  $\mathbf{v}$  such that

$$\mathbf{v}_{k+1} = \mathbf{v}_k + \frac{1}{8}\mathbf{g}_k. \quad (3.14)$$

A factor  $\frac{1}{8}$  is used to ensure stability. In practice this procedure is implemented as a matrix vector multiplication such that

$$\mathbf{v}_{k+1} = \mathbf{D}_{\text{div}}\mathbf{v}_k \quad (3.15)$$

where  $\mathbf{D}_{\text{div}}$  is in essence a “smoothing” filter matrix. This matrix is constructed in such a way that the velocity vectors at the boundaries of the domain are preserved. In each iteration the flow is directed from convergent areas to divergent areas. Figure 3.9 demonstrates the effect of applying anti-divergence operator  $\mathbf{D}_{\text{div}}$ . Figure 3.9(a) shows eight upward pointing velocity vectors which start and end abruptly. Figure 3.9(b) shows the result after ten iterations of the anti-divergence operator: vortices are generated that connect front to back and make the flow field continuous. Consequently, the local divergence at the start and end of the initial eight velocity vectors is reduced, and fluid no longer suddenly appears or disappears.

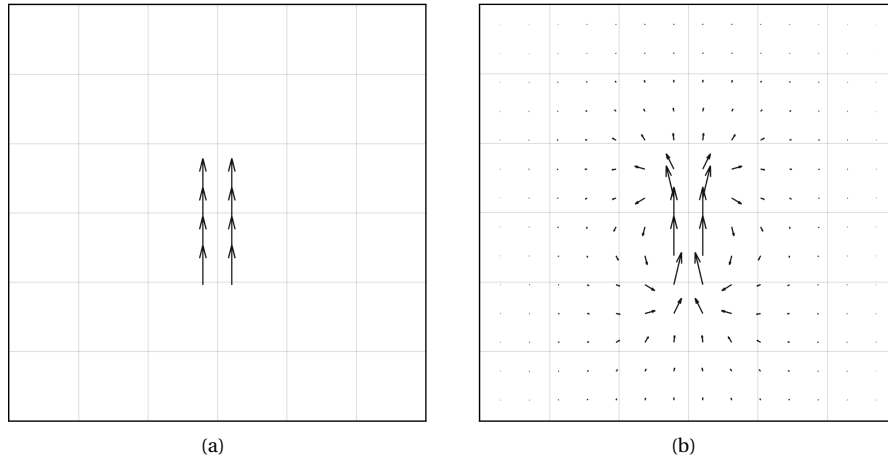


Figure 3.9: Result of applying the anti-divergence operator to a group of velocity vectors. Before (a) and after (b): the flow field is made continuous by connecting vectors front to back.

Figure 3.10 shows the effect of applying the anti-divergence operator on a junction with channels at a very sharp angle. Figure 3.10(a) indicates the area of interest with nonzero divergence; Figure 3.10(b) shows a close-up of the area when no filter is applied; Figure 3.10(c) shows the same close-up but after 30 iterations of the divergence filter. The initial projection in Figure 3.10(b) is imperfect, as the velocity vectors still point rightwards at the rightmost end of the junction. The correction in Figure 3.10(c) fixes this by redirecting the streamlines towards the two side branches.

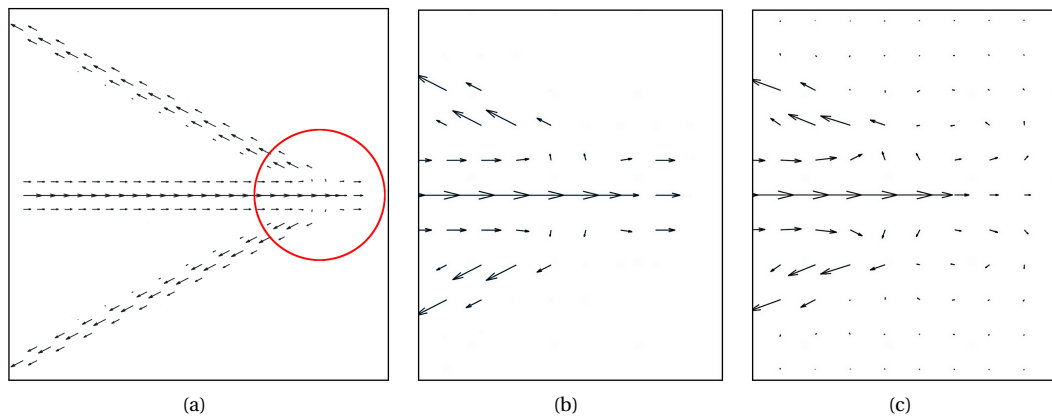


Figure 3.10: Anti-divergence operator applied to a junction of branches encircled in (a). Figure (b) is without the operator. Figure (c) shows the effect of the anti-divergence operator: outward pointing flow in (b) is reduced and turned around towards the two side branches.

Anti-divergence operator  $\mathbf{D}_{\text{div}}$  reduces discontinuities and is not computationally intensive. Too many iterations, however, should be avoided since undesirable swirling motion can occur. After the projected velocity field has undergone the corrections by the smoothing and anti-divergence operators, the effects on the heat transfer are determined by the FEM evaluation step. All TO results in this thesis use seven iterations of the divergence filter. This value was chosen through trial-and-error, based on a trade off between divergence

removal, computation time, and unwanted swirling motion. A parameter study for the optimal amount of iterations was out of the scope of this thesis.

It should be noted that the anti-divergence operator creates small amounts of flow around areas where big corrections are made, see Figure 3.10(c). Possible solutions for this unwanted artifact are weightings based on the local density  $\rho$ , or ideally, no-slip boundary conditions at channel walls. Currently, the boundary conditions for the anti-divergence operator are such that the velocities at the outer boundaries of the structured grid are preserved. In theory, the applied operator could be constructed to only operate on elements with nonzero flow. Regardless, the flow artifacts are small in magnitude, and correspondingly the effect on the temperature distribution is marginal, as will become clear in the next chapter.

### 3.4. Sensitivities

When a gradient based method is used, it is important to carefully consider the most efficient way to calculate the sensitivities. In an optimization problem there are multiple ways to derive the sensitivities, such as global finite differences, discrete derivatives, and continuum derivatives. In the case of density based topology optimization it is possible to avoid finite differences altogether. Additionally, since the amount of constraints is much lower than the amount of design variables, it is faster to use the so called adjoint method instead of the direct method to calculate sensitivities. A detailed overview of the sensitivities using the adjoint method can be found in Appendix A. In Section A.1, the sensitivities for a temperature objective are derived, where attention is given to the application of the chain rule. In Section A.2, sensitivities are derived for a hybrid 2-D/3-D model which is presented in Part II of this thesis. For the sensitivities of the hybrid model, difficulties lie in the coupling of a 2-D and 3-D FEM domain.



# 4

## Validation and optimization examples

In this chapter, the model used for the GSP method will be validated against a trusted commercial simulation package. A single channel and a grid of channels are tested. For the latter case, the Reynolds number is gradually increased to test the range of validity for the Stokes flow assumption. Additionally, a number of numerical optimization examples are shown. An optimization verification is done for a simple three branch flow divider. Subsequently, a more intricate ground structure is used for a flow divider where the optimization objective is to have an equal outlet flow rate across two outlet channels. This example demonstrates the optimization of a pure fluid flow problem using a pipe flow ground structure. Note that in this example the projection to an FEM mesh serves no purpose other than to demonstrate the projection itself, i.e. the element densities do not influence the flow as the flow equations are merely solved on the ground structure. Finally, a numerical example is shown where the advection-diffusion equation is introduced to solve a thermofluid problem. Here the objective will be the minimization of the average temperature throughout the entire domain.

### 4.1. Validation

Since a physical test setup was out of the scope of this thesis, the model could not be compared against experiments. Hence, the process is restricted to validation against a trusted FEM simulation software package, in this case COMSOL [17]. Two channel layouts are used, see Figure 4.1. To ensure that discrepancies between the GSP model and FEM model can be attributed to differences in the physics (i.e. governing equations) it is important to use a similar setup with regards to FEM specifics such as mesh size and shape functions. A mapped mesh is used for the FEM model with the same structured grid of quadrilateral elements as used for the GSP model. Further details include a one-way coupling from the fluid to the thermal domain; linear shape functions; and a segregated step solver.

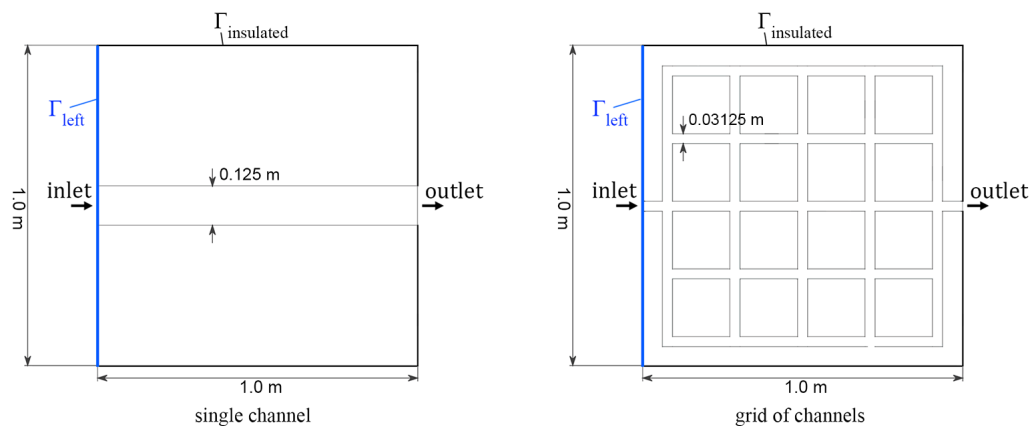


Figure 4.1: Two channel layouts used for validation purposes. For both setups, the temperatures on the left side are set at 0 K above ambient, while the remaining solid boundary is insulated.

### Single channel

For initial validation and verification of the GSP method implementation, a simple test was performed by simulating a single wide channel (0.125m x 0.01m) with an inlet flow of  $q_{in} = 15$  mL/min and comparing the results with an FEM solution. Problem setup is illustrated in Figure 4.1 with corresponding parameters listed in Table 4.1. Thermal and fluid Dirichlet boundary conditions are relative to ambient temperature and pressure. Note that with this flow rate the flow regime is still laminar, but the Reynolds number is out of the creeping flow range. However, since there are no branching channels or curved channels, any effects related to inertia can be ignored. Visual results for the temperature distribution can be seen in Figure 4.2. The maximum relative temperature difference in the entire domain was calculated as  $\frac{|T_{a,max} - T_{b,max}|}{T_{max}}$ , with  $a$  and  $b$  denoting the GSP and FEM models, and  $T_{max}$  being the global maximum temperature. Using a velocity correction factor of 1.07 (see Section 3.3.2), a relative difference of 0.75 % was found, based on an absolute temperature difference of 0.18 K. See Figure 4.2 for a visual comparison of the temperature distribution.

<b>Dimensions</b>	1.0 x 1.0 x 0.01 m, channel: w x h = 0.125 x 0.01 m
<b>Material properties</b>	Solid (aluminum), $\kappa = 205 \text{ W m}^{-1} \text{ K}^{-1}$
	Fluid (water), $\rho = 997 \text{ kg m}^{-3}$ , $\kappa = 0.55 \text{ W m}^{-1} \text{ K}^{-1}$ , $C = 4180 \text{ J kg}^{-1} \text{ K}^{-1}$
<b>Mesh</b>	linear elements, 128 x 128 quadrilaterals
<b>Boundary conditions</b>	Thermal: left side $\Delta T_{left} = 0 \text{ K}$ , outlet $\Delta T_{out} = \text{free}$ , remainder insulated, $10 \text{ W/m}^2$ surface load
	Fluid: inlet $q_{in} = 15 \text{ mL/min}$ (fully developed flow profile), outlet $p_{g,out} = 0 \text{ Pa}$ (gauge)

Table 4.1: Problem parameters for a single channel validation experiment between the GSP method and full FEM.

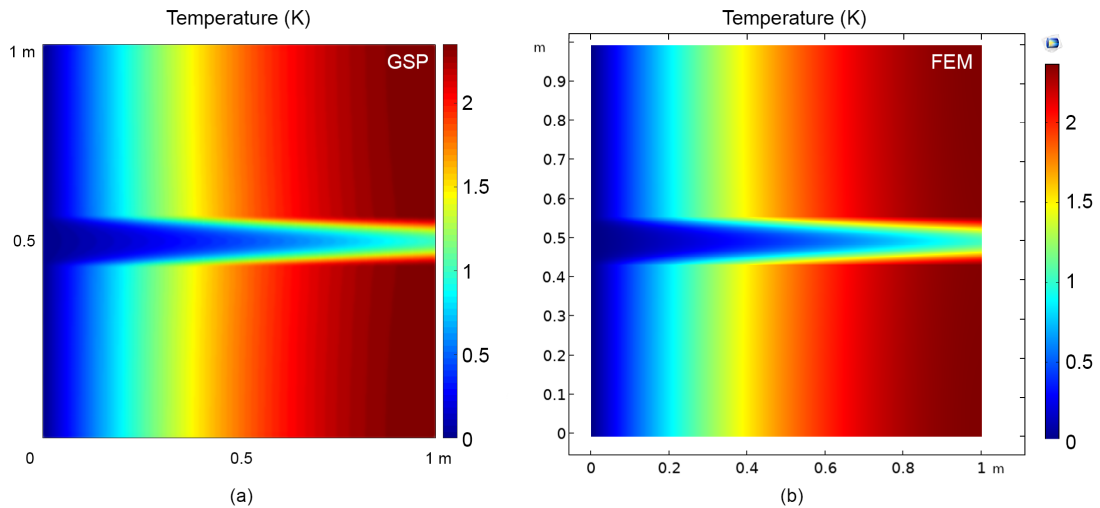


Figure 4.2: Comparison of temperature difference  $\Delta T = T - T_{ambient}$  in a setup with a single channel. Left using the GSP method, right FEM.

### Grid of channels

A more challenging test was performed with a structured grid of channels and comparing against an FEM implementation with a shallow channel approximation. The boundary conditions remain the same, apart from the inlet flow rate which is now 6 mL/min. Problem parameters are listed in Table 4.2. A visual comparison of the flow can be seen in Figure 4.3. The chosen inlet flow rate results in flow outside of the creeping flow regime, i.e. the Reynolds number exceeds one. However, the inclusion of the inertial term in the fluid equations only results in negligible velocity differences.

In Part II of this thesis, the cooling channel layout of an optical instrument is optimized. Cooling performance increases for higher inlet flow rates, and thus it is useful when the Stokes equations can be still be applied for flow outside of the creeping flow regime. To test the range of validity for the Stokes flow assumption, an additional experiment was carried out in COMSOL where the effect of the inertial term for the fluid equations was analyzed. Relative errors for creeping flow ( $q_{cr}$ ) versus laminar flow *with* the inertial term ( $q_{la}$ ) were evaluated for a number of sample points, see Figure 4.4(a). The relative errors are plotted as a function

of the inlet Reynolds number  $Re_{in}$  in Figure 4.4(b). One can observe for example that at point p3 the flow rate  $q_{cr}$  is smaller than  $q_{la}$  for higher Reynolds numbers. The Reynolds number is calculated as  $\frac{vL_c\rho}{\mu}$ , where a characteristic length scale  $L_c$  of two times the channel width is used [82]. For  $Re_{in} = 20$ , the errors are still well within the 5% margin. Furthermore, when a 3-D geometry is considered with finite channel depth, the viscous forces are more pronounced, resulting in a lower effective Reynolds number for equal inlet flow rates, and thus a smaller discrepancy between Stokes and full Navier-Stokes modeling.

<b>Dimensions</b>	1.0 x 1.0 x 0.01 m, channels: w x h = 0.03125 x 0.01 m
<b>Material properties</b>	Solid (aluminum), $\kappa = 205 \text{ W m}^{-1} \text{ K}^{-1}$
	Fluid (water), $\rho = 997 \text{ kg m}^{-3}$ , $\kappa = 0.55 \text{ W m}^{-1} \text{ K}^{-1}$ , $C = 4180 \text{ J kg}^{-1} \text{ K}^{-1}$
<b>Mesh</b>	linear elements, 128 x 128 quadrilaterals
<b>Boundary conditions</b>	Thermal: left side $\Delta T_{left} = 0 \text{ K}$ , outlet $\Delta T_{out} = \text{free}$ , remainder insulated, $10 \text{ W/m}^2$ surface load
	Fluid: inlet $q_{in} = 6 \text{ mL/min}$ (fully developed flow profile), outlet $p_{g,out} = 0 \text{ Pa}$ (gauge)

Table 4.2: Problem parameters for a grid of channels validation experiment between the GSP method and full FEM.

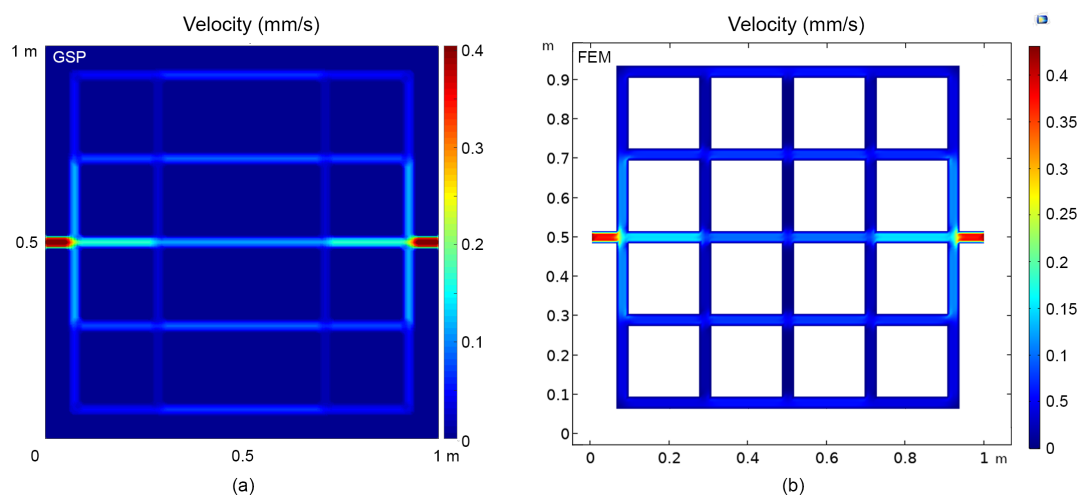


Figure 4.3: Comparison of flow velocities in a grid of channels with an inlet flow rate of 6 mL/min. (a) using the GSP method, (b) using FEM with shallow channel approximation.

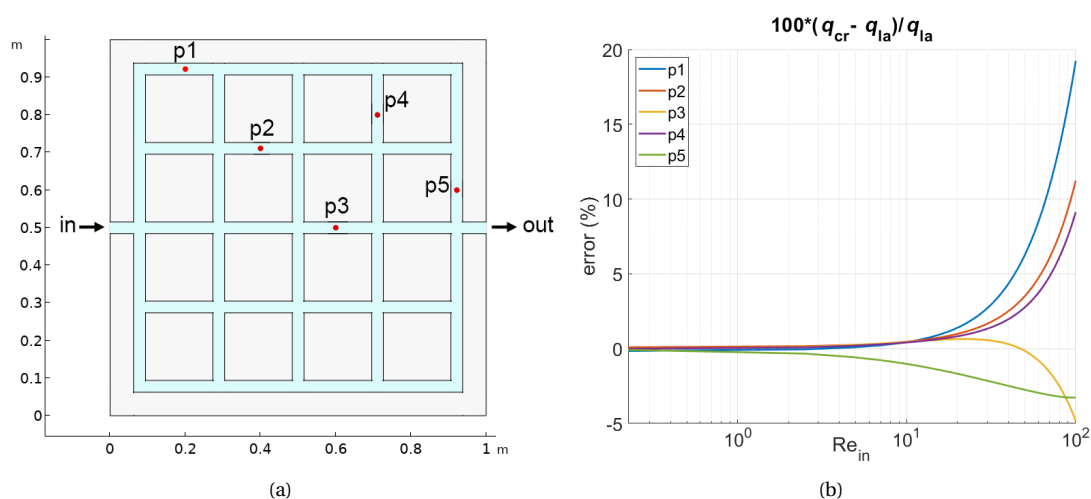


Figure 4.4: Additional experiment carried out to determine validity of Stokes assumption. Deviation of channel flow rate with Stokes approximation ( $q_{cr}$ ) compared to full Navier-Stokes laminar flow ( $q_{la}$ ), at points marked in (a). Figure (b) plots the deviation percentage as a function of the inlet Reynolds number.

Figures 4.5(a) and 4.5(b) show the resulting temperatures for the GSP and FEM models. A diagonal cut line (visible in Figure 4.5(c)) was used to sample and plot the temperatures across the domain in Figure 4.5(d). This allows for a quantification of the differences between the two models. The maximum relative temperature difference on the cut line was calculated as  $\frac{|T_a - T_b|}{T_{\max}}$ , with  $T_{\max}$  the maximum temperature on the cut line. A relative difference of 3% was found, based on an absolute temperature difference of 0.39 K. The discrepancy of 3% between the two models was found in the center region of a cooling channel. At the location of the largest error, the temperature is slightly higher for the GSP model compared to the FEM model. This can be due to a number of factors. The COMSOL FEM software package has a more sophisticated way of approximating 3-D shallow channel flow in 2-D: a drag term as a volume force is added which depends on local velocity and channel height [18]. In contrast, the GSP method assumes a parabolic flow profile and uses a correction factor to compensate for shallow channel drag. This can result in local flow differences. Additionally, the relatively low mesh resolution can introduce errors if the centerline of a channel is aligned with a grid element interfaces. Still, the issue occurs only locally and 3% is an acceptable error margin for the optimization model.

For both examples, a single channel and a grid of channels, the GSP model shows good agreement with the full FEM simulation, especially taking into account the simplifications made for the GSP model. Considering this, the results are sufficiently accurate for the GSP model to be used as a performance evaluation step in an optimization routine. Additional validation examples are shown in Appendix C. A Y-split channel structure is analyzed for different channel widths: here it becomes clear that very thin channels can present challenges when dealing with highly conductive solid material. Furthermore, qualitative examples of the velocity projection are shown, as well as a case with a narrowing channel.

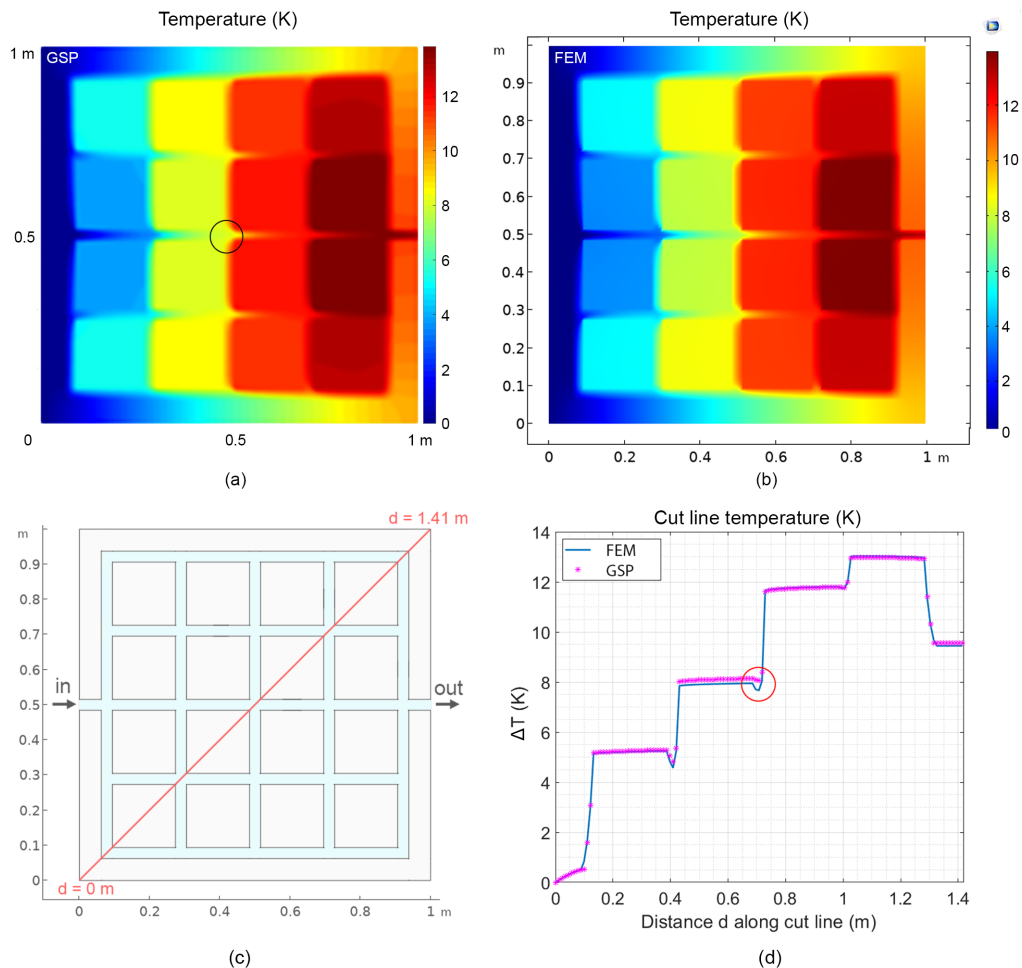


Figure 4.5: Comparison of temperature difference  $\Delta T = T - T_{\text{ambient}}$  using GSP (a) and FEM (b) for a grid of channels. Circled area in Figure (a) indicates location of largest error. Temperatures are sampled along cut line drawn in (b). Plot of temperatures in FEM and GSP models in (d); circled area indicates location of largest error.

## 4.2. Optimization example 1: Flow divider

The first numerical optimization example is a simple flow divider consisting of three ground structure branches in a square domain, see Figure 4.6. This example therefore functions as a sanity check for the GSP method. Since the objective concerns only flow, the projection step serves no other purpose than to demonstrate the GSP projection.

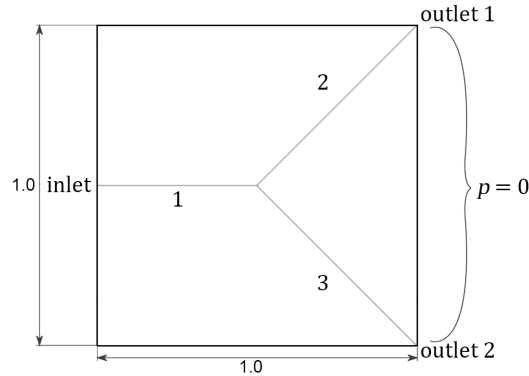


Figure 4.6: Simple three branch ground structure used to test the GSP method.

Since creeping flow is assumed, flow rate and pressure drop are linearly related. A domain thickness of 0.01, combined with an inlet flow rate of  $q_{\text{in}} = 10^{-8}$  and a dynamic viscosity of  $\mu = 10^{-3}$  are chosen such that the inlet Reynolds number  $\text{Re} < 1$ . Initially, the topology is only optimized for minimal pressure drop. The problem is stated as:

$$\begin{aligned} \min_{\chi} : h(\chi) &\equiv p_{\text{in}} - \frac{1}{2}(p_{\text{out},1} + p_{\text{out},2}) \\ \text{subject to} : \mathbf{K}_F(\chi)\mathbf{p} &= \mathbf{q}_F \\ &: 10^{-7} \leq \chi_i \leq 0.06 \end{aligned} \quad (4.1)$$

which states that the pressure objective is a function of design variables  $\chi$ , and is calculated as the inlet pressure minus the average of the outlet pressures. Also, the governing system of equations is based on Equation 3.1; and the design variables  $\chi$  have a lower bound of  $10^{-7}$  and an upper bound of 0.06. Figure 4.7 shows the results after 20 iterations of Matlab's built in fmincon interior-point algorithm, which is used in all problems from here on. Since this is a pressure drop minimization problem, the result should be maximum channel width for all branches, as this will minimize the hydraulic resistance. The optimization algorithm produced the expected results, with all design variables  $\chi$  (i.e. half width of channels) converging to the upper bound:  $\chi_i = 0.06$ .

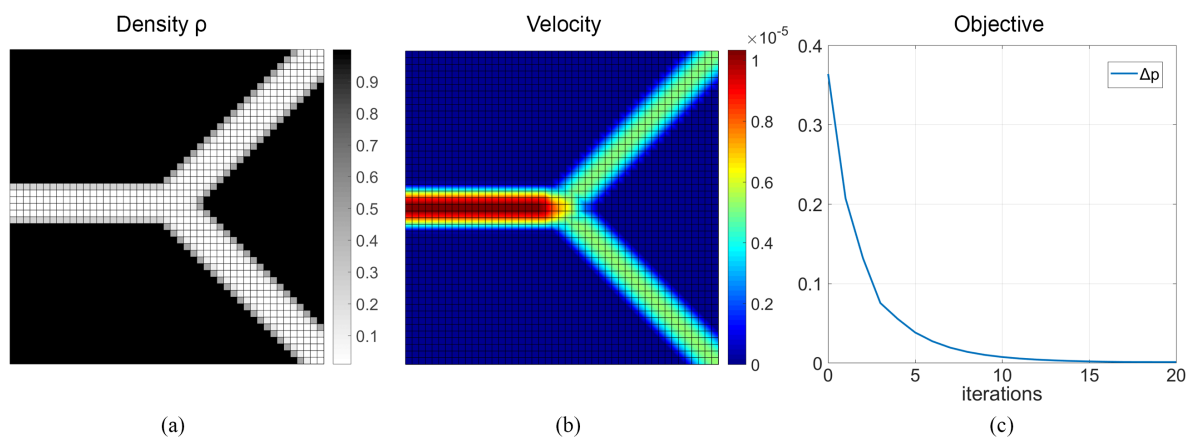


Figure 4.7: Results for minimizing pressure drop. (a) and (b) shows the projected densities and velocities respectively. History of the pressure drop objective  $\Delta p$  is plotted in (c).

Now, the test case is extended to minimize the flow rate  $q_2$  in the upper right channel branch. The problem is now stated as:

$$\begin{aligned} \min_{\chi} : h(\chi) &\equiv (p_{\text{in}} - \frac{1}{2}(p_{\text{out},1} + p_{\text{out},2})) + \alpha |q_{c,2}| \\ \text{subject to} : \mathbf{K}_F(\boldsymbol{\chi})\mathbf{p} &= \mathbf{q}_F \\ &: 10^{-7} \leq \chi_i \leq 0.06, \end{aligned} \quad (4.2)$$

where  $\alpha = 10^8$  is used to normalize the flow rate objective. With the chosen objectives, channel 1 and 3 (left and bottom right) are expected to reach the maximum channel width, whereas channel 2 should be constricted depending on the chosen weight  $\alpha$ . Again, the results (Figure 4.8) are as expected, with channel 1 and 3 widened to the upper bound of 0.06. The chosen objective weight  $\alpha$  favors a design with minimal flow through channel 2, and consequently the width of channel 2 is minimized to the lower bound of  $10^{-7}$ .

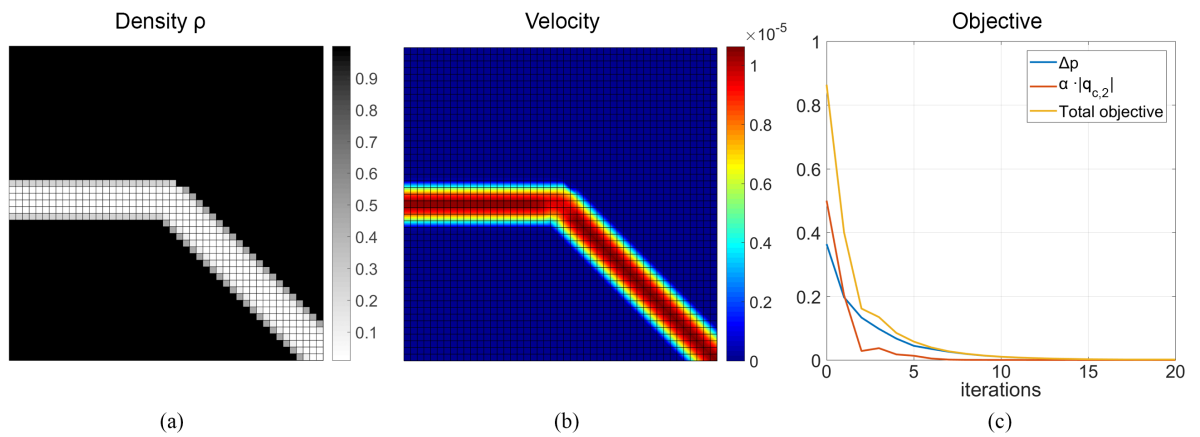


Figure 4.8: Results for minimizing flow in top right branch and also the pressure drop. In (a) the densities; (b) projected velocities; and (c) the pressure drop, flow rate, and total objective. To bring the objectives into the same range of (0, 1), the flow rate objective is normalized with  $\alpha = 10^8$ .

### 4.3. Optimization example 2: Minimizing pressure drop

In this numerical example a more complex ground structure is used. The objective is to minimize the pressure drop from inlet to outlets. Similar to the previous example, the projected densities serve no purpose in this example other than to demonstrate the GSP projection.

#### Problem setup

Figure 4.9 shows the initial ground structure generated by a Delaunay triangulation of 930 randomized nodes. Three extra nodes are positioned on the border; one for the inlet on the left, and two for the outlets on the right side. The Dirichlet boundary condition is satisfied by setting the outlet pressures to zero. Other numerical parameters are the same as the previous three branch experiment, i.e. a domain thickness of 0.01, an inlet flow rate of  $q_{\text{in}} = 10^{-8}$ , and a dynamic viscosity of  $\mu = 10^{-3}$ .

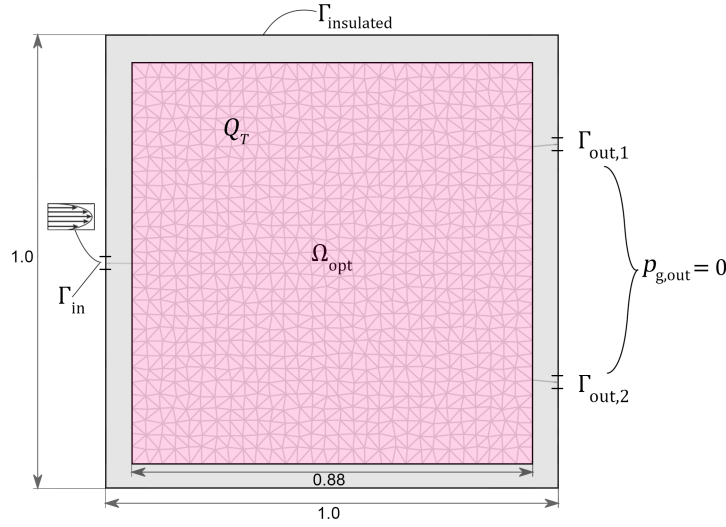


Figure 4.9: Boundary conditions and initial ground structure for a thermofluid topology optimization problem. Domain  $\Omega_{\text{opt}}$  contains the ground structure and coincides with the area of thermal load  $Q_T$ .

The objective and constraints are stated as follows:

$$\begin{aligned}
 \min_{\chi} : h(\chi) &\equiv p_{\text{in}} - \frac{1}{2}(p_{\text{out},1} + p_{\text{out},2}) \\
 \text{subject to} : \mathbf{K}_F(\chi)\mathbf{p} &= \mathbf{q}_F \\
 &: \sum_{i=1}^m \chi_i \leq \frac{m}{16.5} \chi_{\text{max}} \\
 &: 10^{-7} \leq \chi_i \leq 0.021
 \end{aligned} \tag{4.3}$$

A channel area limiting factor of  $\frac{1}{16.5}$  together with a maximum channel width of 0.042 are used to limit the amount of cooling channel area. These values were chosen based on the resulting designs, which feature sparse and clearly discernible channel layouts. Instead of a constraint on the channel area, an area/volume constraint directly on the densities can be implemented. However, this was omitted due to time considerations and absence of strict requirements on cooling channel area.

#### Results

The results in Figure 4.10 show how the available channel space is used to create two “bundles” of channels. Channels in the center of the bundles are wider, while longer channels at the edges of the bundles are thinner. The channels take the shortest path from inlet to outlet, which minimizes the hydraulic resistance. Clearly the results are dependent on the initial ground structure. A higher resolution and/or a more connected ground structure will yield a more optimal channel layout, i.e. a shorter path from inlet to outlets.

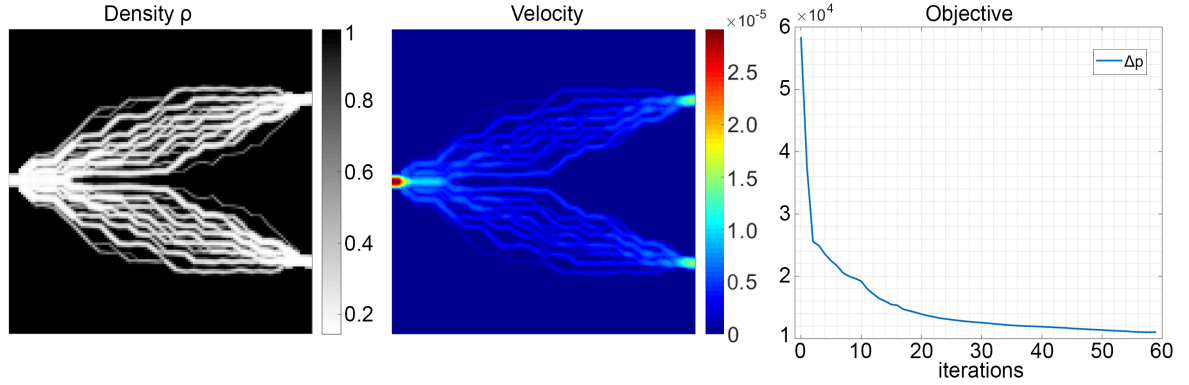


Figure 4.10: Results for optimization for minimal pressure drop. On the left, projected densities  $\rho$  show two bundles of channels. Velocities are visible in the middle image. On the right is the objective history, which shows good convergence. Final objective value is  $\Delta p = 1.1 \cdot 10^4$ .

### 4.4. Optimization example 3: Cooling device

In this numerical example, the objective is modified to also include the average temperature of the area to which heat load  $Q_T$  is applied. The projected densities and velocities will now be used in the advection-diffusion equation to determine the temperatures. Numerical parameters are chosen to create a convection dominated problem. Thermal conductivities for solid and fluid are  $\kappa_{\text{solid}} = 0.1$  and  $\kappa_{\text{fluid}} = 1$ . The optimization is run using Matlab's `fmincon` interior point algorithm with 60 iterations as the only termination criterion.

#### Problem setup

The same ground structure is used as in Figure 4.9. The optimization problem is now stated as:

$$\begin{aligned}
 \min_{\chi} : h(\chi) &\equiv \beta \left( p_{\text{in}} - \frac{1}{2}(p_{\text{out},1} + p_{\text{out},2}) \right) + \frac{1}{n} \sum_{i=1}^n T_i \\
 \text{subject to} : \mathbf{K}_F(\chi) \mathbf{p} &= \mathbf{q}_F \\
 &: \mathbf{K}_T(\chi) \boldsymbol{\theta} = \mathbf{q}_T \\
 &: \sum_{i=1}^m \chi_i \leq \frac{m}{16.5} \chi_{\text{max}} \\
 &: 10^{-7} \leq \chi_i \leq 0.021
 \end{aligned} \tag{4.4}$$

#### Results

Figure 4.11 shows three results for different weighting factors  $\beta$  for the pressure drop objective relative to the thermal objective. The thermal objective becomes more important as  $\beta$  decreases, and the results show designs with thinner, more numerous channels branching out across the entire domain. Evidently, the average temperature decreases for lower values of  $\beta$ . Some thin channels appear to be dead ends without flow, however this is expected since the fluid has a higher thermal conductivity than the solid material. Figure 4.12 shows the histories of the weighted objectives.

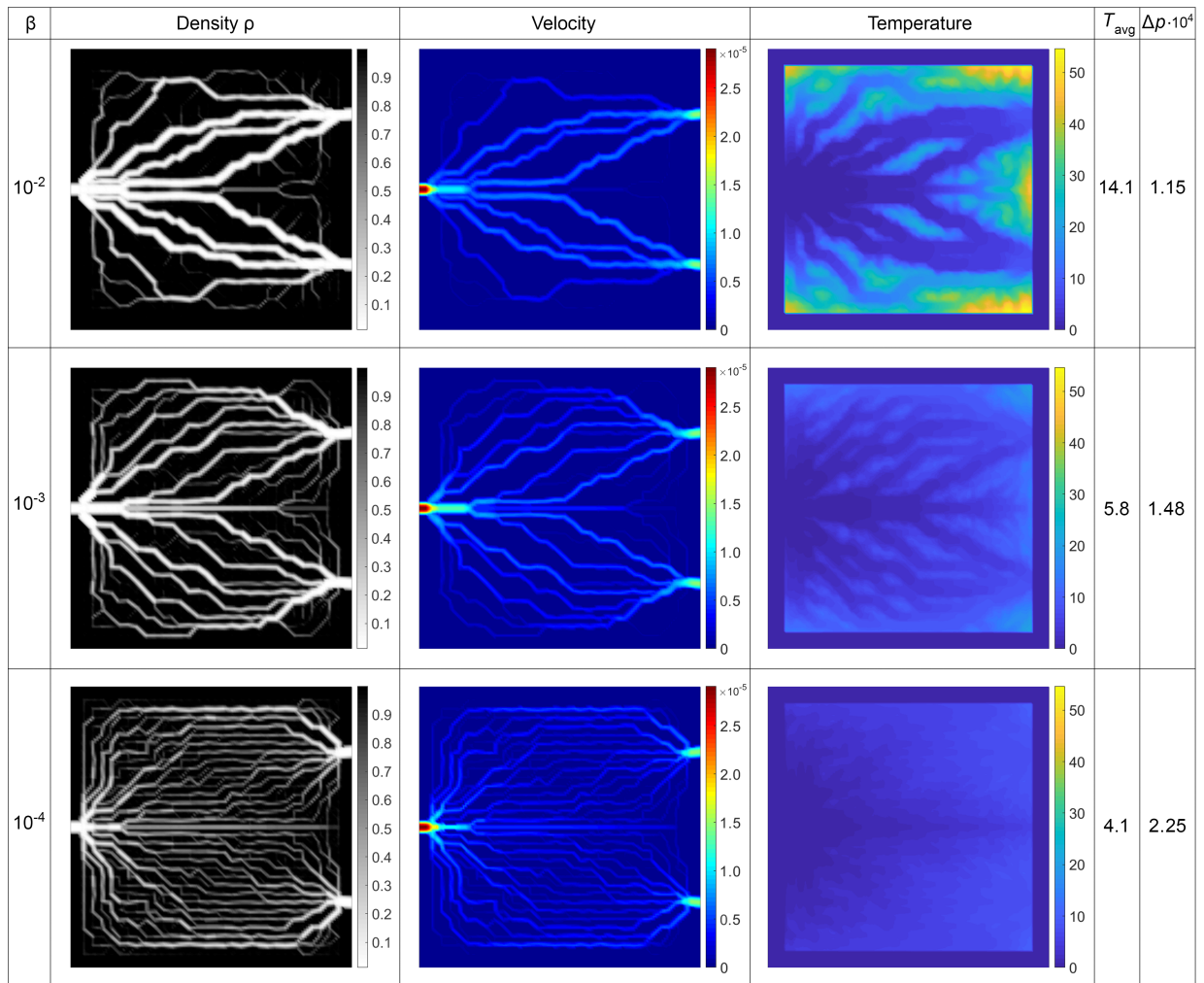


Figure 4.11: Results of a multi-objective thermofluid optimization using the GSP method. The designs are optimized for minimal average temperature  $T_{\text{avg}}$  and pressure drop  $\Delta p$ .  $\beta$  is the weight placed on the pressure drop objective: lower values of  $\beta$  lead to more intricate designs that perform better for  $T_{\text{avg}}$  and worse for  $\Delta p$ .

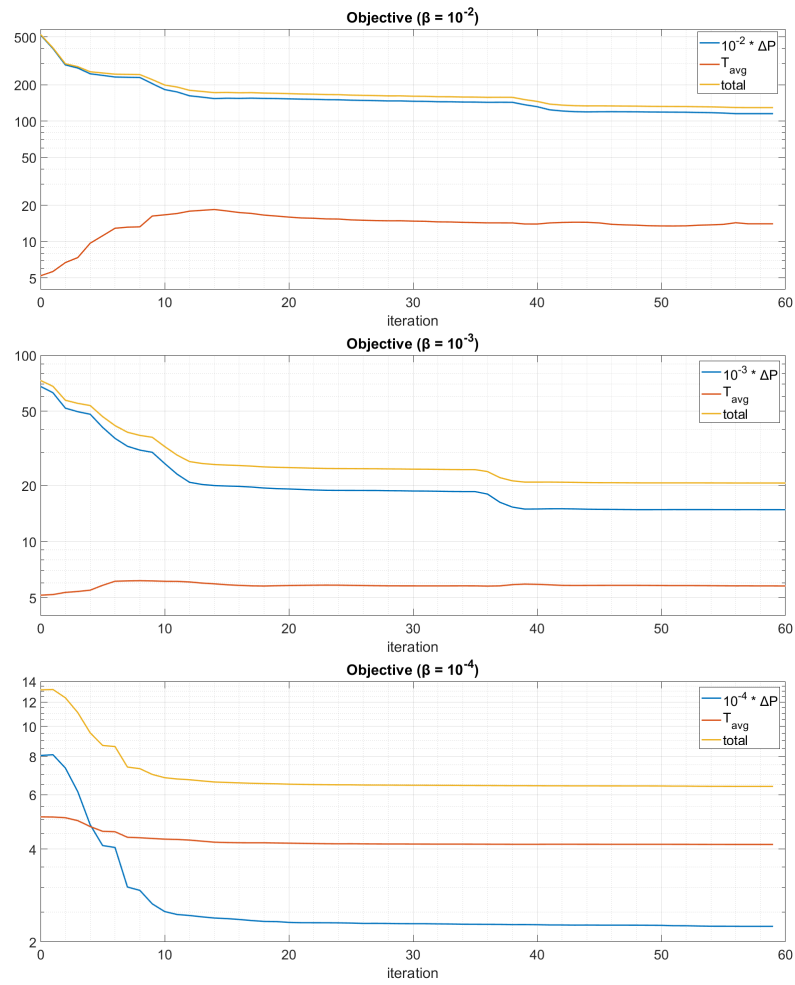


Figure 4.12: Objective histories for the thermofluid optimization problem. Three different weights  $\beta$  are shown. A lower value for  $\beta$  gives better cooling results at the cost of a greater pressure drop.

# 5

## Benefits and limitations

The GSP method works on the assumptions of pipe flow and a ground structure with a predefined layout and a specific coarseness. This approach carries benefits, but also comes with limitations. This chapter elaborates on the benefits and areas of applicability of the method, and on situations where a density based method would be better suited.

### 5.1. Benefits

Pipe flow assumes channels of constant cross section, with a diameter that is significantly smaller than the length of the channel. Thin channels used for cooling purposes or other transport phenomena can be found in a range of utilities. An example would be the field of microfluidics which deals with systems that manipulate and process fluids with channels at a microscopic scale. This means that in many cases creeping flow applies and the GSP method can potentially be of benefit.

#### Computation speed

When the number of DoFs increase with mesh refinement or an extension to 3-D models, the computation time will increase likewise. If Darcy-Stokes flow is used with density based thermo-fluid-(mechanical) TO, then the most computationally intensive part of the routine will be solving the flow. Hence, any simplification on that front will give a meaningful reduction in computation time. Discretizing the governing equations of Stokes flow (Eqs. 2.1 and 2.3) with appropriate boundary conditions results in the following system of equations<sup>1</sup>:

$$\begin{bmatrix} \mathbf{K} & \mathbf{G} \\ \mathbf{G}^T & \mathbf{0} \end{bmatrix} \begin{bmatrix} \mathbf{v} \\ \mathbf{p} \end{bmatrix} = \begin{bmatrix} \mathbf{f} \\ \mathbf{h} \end{bmatrix}. \quad (5.1)$$

This matrix system is solved for  $\mathbf{v}$  and  $\mathbf{p}$  which are the velocities in all directions and the pressures. This means that compared to the pipe flow network, finding the solution to a Stokes flow problem in 2-D requires solving at least three times as many DoFs, since velocities  $v_x$  and  $v_y$  have to be found simultaneously as well. In 3-D, also the z-component of the flow velocity has to be computed, whereas the pipe flow network still has only one DoF per node.

In addition to this, the discretization of Stokes flow gives rise to saddle point problems which require the so called LBB-condition to be met to guarantee stability, i.e. to avoid oscillations in the pressure field [28]. This stability problem can be solved by using quadratic elements, or when linear elements are used, with a stabilization term. Both methods significantly increase computation time. With the quadratic elements, midpoints are used for the velocities inside an element, see for example the Q2Q1 “Taylor Hood” element in Figure 5.1. Compared to the Q1Q1 element, this introduces another 5 velocity nodes in a quadrilateral element or 12 velocity nodes in a hexahedral element [83]. Furthermore, the bandwidth of the stiffness matrix increases with quadratic elements, which again increases computation time. If linear elements are used, a stabilization term is required which makes the stiffness matrix denser and thus solving slower. Comparing this to the network equations of Eq. 3.1 shows the obvious computational advantage of using the pipe flow simplification. For pipe flow networks, only a single DoF per node has to be solved; this is true for both 2-D

---

<sup>1</sup>See for example Donea & Huerta [28].

and 3-D networks. Assuming a structured grid mesh with quadrilateral or hexahedral and an equal amount of pressure nodes for both the GSP and Stokes flow approach, the reduction in DoFs can be calculated as follows. With a 2-D mesh of  $n$  by  $n$  elements, the GSP mesh will have  $m^2$  pressure nodes (where  $m = n + 1$ ) and an equal amount of DoFs. An FEM mesh consisting of Taylor-Hood elements will have  $m^2$  pressure DoFs and  $2 \cdot (2m - 1)(2m - 1)$  velocity DoFs. The ratio of FEM vs. GSP DoFs becomes  $\frac{9m^2 - 8m + 2}{m^2}$ , which for large  $m$  converges to 9. Likewise, the calculation for a 3-D mesh will amount to a factor 13 reduction in DoFs for hexahedral Taylor-Hood elements.

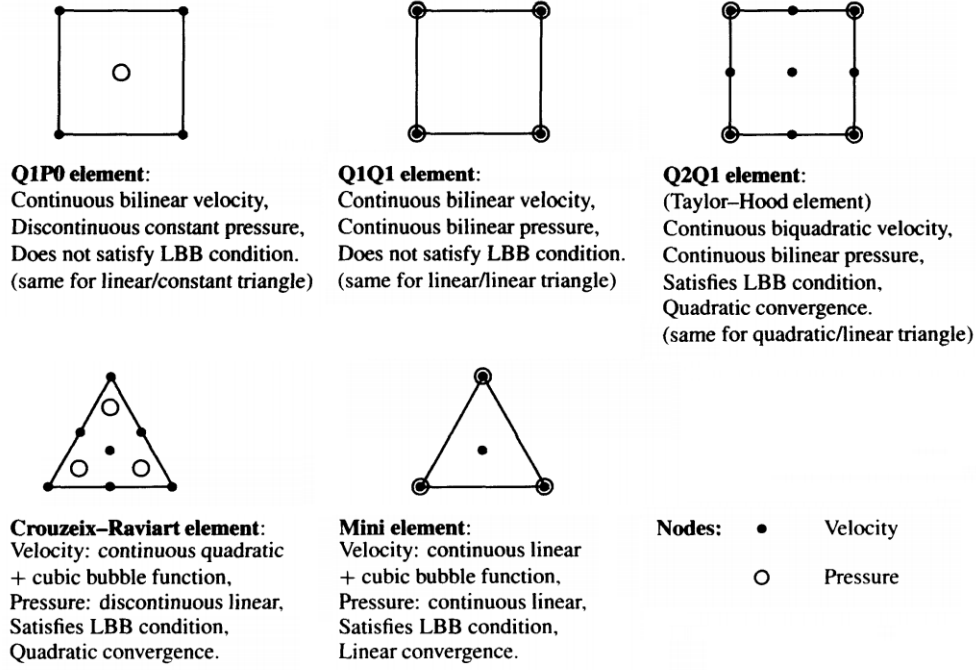


Figure 5.1: Examples of 2-D stable and unstable element types for solving Stokes flow, from [28], where stable elements satisfy the LBB conditions. Unstable elements require an additional stabilization term, whereas stable elements require extra DoFs to be solved.

Another computational advantage of the GSP method is due to the decoupling of the channel ground structure and the FEM mesh: the ground structure can be much more coarse than the FEM mesh. This might be useful in a situation where design constraints prohibit channels in certain parts of the domain. A ground structure can then be chosen that is adapted to a specific geometry and design domain and requires less DoFs for the fluid solve while still maintaining the numerical accuracy of a finer FEM mesh. Although specific timing tests or direct computational speed comparisons between the GSP method and other TO methods were not investigated, a computational advantage for the GSP method is expected considering the discussed details.

### Feature control

Similar to the MMC/MMV methods (see Section 2.1.3), having explicit knowledge about channel topology gives additional possibilities to control channel features over density based TO [35, 90]. Examples include control of structural complexity to satisfy manufacturing constraints such as channel curvature radius, or a maximum number of branches at channel junctions. Another example is maximum channel width; while not impossible with density based TO [33, 47], a maximum channel width constraint is trivial with the GSP method.

## 5.2. Limitations

With the assumptions of pipe flow also come limitations. This section describes some examples where limitations become apparent or where a different method might be better suited.

### Accuracy

The GSP method is intended as a tool for initial design purposes. Considering this, a solution within 5% of results produced by a commercial FEM package is acceptable. However, for highly accurate simulations or design refinement, a full FEM discretization of the fluid physics would be a better choice.

### Wide channels

The Hagen-Poiseuille equations assumes straight and long channels. This makes the GSP method unsuitable for situations as seen in Figure 2.11 for example, where channel widths are very big compared to the channel length. The assumption of a parabolic shaped flow profile does not hold in situations with very wide channels, and any local in-channel effects of the flow profile on the temperature would have to be taken into account.

### Ground structure dependence

All possible channel paths are restricted to the underlying ground structure. This has to be taken into account when using the GSP method. A coarse ground structure will be fast computationally but the resulting designs might not be optimal, whereas a fine and highly connected ground structure is slower and requires extra attention to avoid overlapping channels. Ideally, the ground structure has sufficient nodes and connections between nodes to accommodate all designs that would be possible in a Darcy-Stokes density based method. A fine ground structure with high connectivity poses no problems for mechanical TO, however when projecting fluid channels onto an FEM mesh care has to be taken to prevent crossing and overlapping channels. A possible solution to prevent crossing channels is to implement a constraint of the following form:

$$\sum_{i,j} \chi_i \cdot \chi_j < c \quad (\text{for every crossing pair } \{i,j\}), \quad (5.2)$$

with  $\chi$  being the design variables, i.e. half the channel width, and  $c$  some (small) constant. This constraint has been tested on an elementary ground structure as a proof of concept, but further investigations are required to give an indication of the feasibility in actual cases with high resolution ground structures.

Other solutions to prevent overlapping channels are non-overlapping constraints as seen in other geometry projection methods [75], or a form of collision detection as used in multibody dynamics engines [19].

### Higher Reynolds numbers

While the method described in this thesis assumes creeping flow, it is also possible to calculate the flow rate in pipe networks with higher Reynolds numbers or even turbulent flow. Pipe networks with high Reynolds flow are more complex to solve due to the nonlinear relation between pressure drop and flow rate. The hydraulic resistance in a pipe or branch is a lumped parameter that represents all head losses for the given branch geometry and flow conditions. In cases where inertia related effects have an influence, the hydraulic resistance has to account for minor losses due to junctions, channel curvature, entrance effects, etc. [64]. Before the advent of computers, the so called Hardy-Cross method [20] was used to iteratively determine flow rates inside networks. Nowadays, algorithms better suited to computing are used such as Newton-Raphson. An extension of the GSP method to high Reynolds laminar flow, or turbulent flow is an interesting avenue for future research.



# II

## Minimizing thermomechanical distortions in optical instruments

In this part of the thesis, the GSP method will be applied to an industrial case involving a POB mirror in an EUV photolithography machine. Fabrication of modern day computer chips requires exceptionally precise machinery in order to create nanometer scale integrated circuits. The design of photolithography machines has to account for all sorts of possible errors including misalignment issues due to thermal expansion. Predictability or reduction of these thermal errors is required to shrink the process nodes and to increase production output and profitability. By optimizing for temperature uniformity across the surface of a Projection Optics Box (POB) mirror, an attempt is made to minimize unwanted thermomechanical deformation.

The first chapter (Ch. 6) of this part provides a summary of relevant literature and information on thermomechanical TO and the optimization of optical instruments. Chapter 7 describes the POB mirror problem in detail and demonstrates the hybrid 2-D/3-D model used to simulate the fluid and thermal physics. Chapter 8 presents and discusses the optimization results for two different heat loads. Finally, in Chapter 9 an optimized design is transferred to the COMSOL simulation package to evaluate the thermomechanical deformation.



# 6

## Thermally induced optical aberration

Thermally induced optical aberration is a consequence of thermal expansion characterized by the coefficient of thermal expansion (CTE). To date there have been several studies on thermomechanical TO using different optimization methods. Early work on thermomechanical TO was done by Rodrigues and Fernandes [68] in 1995, who employed the homogenization method to minimize compliance of structures subjected to combined thermal and mechanical loads. Li et al. have approached the problem using the ESO method [48, 49]. The first application of the density-based method was by Sigmund [72], whereas Deng and Suresh [24] used the level-set method. The use of adjoint sensitivities in coupled thermomechanical problems has been covered by Cho and Choi [15]. Among other interesting applications, thermomechanical TO has also been used to optimize spacecraft thermal protection systems by Kim et al. [42] and Penmetsa et al. [59]. Lastly, Sigmund and Torquato [74] used topology optimization to generate structures with extreme or unusual thermal expansion behaviour. Since thermally induced optical aberration is a direct consequence of thermomechanical deformation, the findings of the above authors and others have been applied to topology optimization of optical instruments, which is discussed in the following section.

### 6.1. TO of optical instruments

Applying topology optimization to mirrors requires a reliable performance measure to evaluate the optimization results. A paper from 2003 by Park, Chang, and Youn [56] describes the topology optimization of a mirror in a multi-spectral camera for space-use. A type of pseudo 3-D topology optimization was applied where the mirror surface is the 2-D design domain and the TO algorithm optimally distributes material across this 2-D surface. Subsequently a 3-D FEM simulation was done where the densities from the 2-D distribution represent the thickness of the mirror. As a measure of optical performance the root mean square (RMS) error of the normal displacement components of the mirror surface was used. The mirror surface displacement itself was described using a special set of polynomials called Zernike polynomials.

Zernike polynomials are a sequence of polynomials that are orthogonal on the unit disk [12, 92]. Equation 6.1 shows how the wavefront or the deformation of the disk can be described as a sum of weights  $C_n^m$  and Zernike polynomials  $Z_n^m(r, \theta)$  using polar coordinates  $(r, \theta)$ . The Zernike polynomials are defined in Equation 6.2, where radius  $r$  is restricted to the unit circle ( $0 \leq r \leq 1$ ), and  $\theta$  is the azimuthal angle. The radial function,  $R_n^m(r)$ , is described by Equation 6.3. Lower order Zernike modes such as the piston mode ( $Z_0^0$ ), the tip/tilt mode ( $Z_1^{-1}, Z_1^1$ ), or parabolic surface deformations can sometimes be compensated for and hence do not necessarily diminish optical performance.

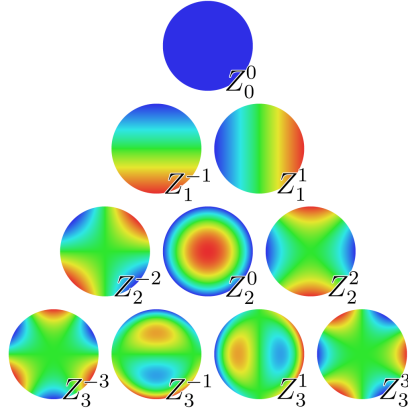


Figure 6.1: The first 13 Zernike polynomials, ordered vertically by radial degree and horizontally by azimuthal degree. [7]

$$W(r, \theta) = \sum_{n,m} C_n^m Z_n^m(r, \theta) \quad (6.1)$$

$$\begin{aligned} Z_n^m(r, \theta) &= R_n^m(r) \cos m\theta & \text{for } m \geq 0, \\ Z_n^{-m}(r, \theta) &= R_n^m(r) \sin m\theta & \text{for } m < 0 \end{aligned} \quad (6.2)$$

$$R_n^m(r) = \sum_{k=0}^{(n-m)/2} \frac{(-1)^k (n-k)!}{k! \left(\frac{n+m}{2} - k\right)! \left(\frac{n-m}{2} - k\right)!} r^{n-2k} \quad (6.3)$$

Using Zernike polynomials, rigid body modes were removed from the RMS error in the investigation by Park, Chang, and Youn. The resulting measure directly relates to the so called Strehl ratio, which is a parameter that represents the resolving ability of an optical system. The resolving ability of any optical system is limited by the “Airy-disk” [1], which is the image created by a perfect point light source. Instead of a point, the Airy disk is a finite sized disk of light with concentric circles. The Strehl ratio compares the peak light intensity of an Airy disk of an imperfect, aberrated optical system, to that of a perfect optical system where the resolution is only limited by diffraction over the system’s aperture. If the normal components of the mirror surface displacement are denoted as  $\hat{U}_n$ , the root mean square of  $\hat{U}_n$  is calculated as:

$$\text{RMS}_{\hat{U}_n} = \sqrt{\frac{\int_{\Omega} \hat{U}_n^2 d\Omega}{\int_{\Omega} d\Omega}} = \sqrt{\frac{\sum_{e=1}^{n_{se}} \int_{\Omega_e} \hat{U}_n^2 d\Omega}{\sum_{e=1}^{n_{se}} \int_{\Omega_e} d\Omega}}, \quad (6.4)$$

where the mirror surface domain is  $\Omega$ , and the surface elements range from  $e = 1$  tot  $e = n_{se}$ . The Strehl ratio is then defined as:

$$\text{Strehl ratio} \approx 1 - 4\pi^2 (\text{RMS}_{\hat{U}_n})^2. \quad (6.5)$$

A paper by Park, Lee, and Youn [57] extends the research from the above authors and applies it to the design of lightweight mirrors, also using the RMS error as a performance measure. Comparable work has been done on the topology optimization of reflective mirrors for high-power laser systems by Kim, Park and Youn [41]. Figure 6.2 shows some results from similar work by Qu et al. [67] who optimized space mirror design for minimum compliance under axial gravity, lateral gravity, and polishing pressure. Furthermore, Liu et al. [50] used TO on support ribs on the backside of a mirror. Resulting designs from the TO process were then used for a parametric optimization where only shape or size was optimized.

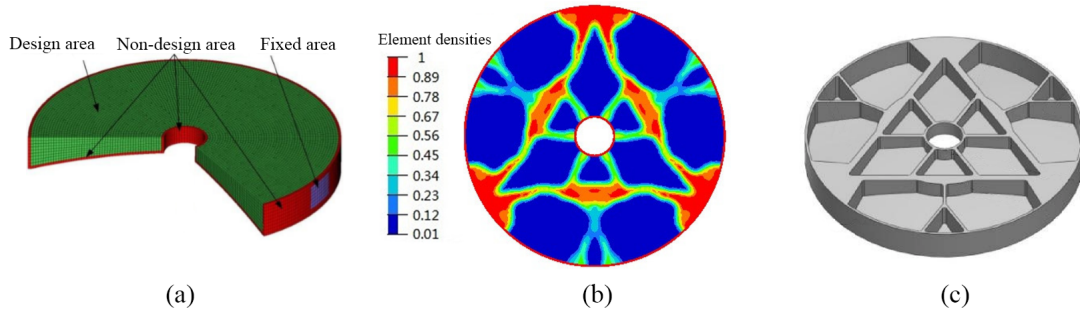


Figure 6.2: Results from Qu et al. [67]: (a) shows a 2/3 cutaway of the mirror design space; (b) shows the optimal density distribution; and (c) shows a practical interpretation from an engineer’s perspective.

In 2018, Koppen et al. [46] used ray transfer matrix analysis to define the objective function in terms of direct optical performance. This can be applied to a complete optical system consisting of multiple components. The topologies of all components are optimized simultaneously. Whereas the previous mentioned literature in this section used the 2-D surface of the mirror as the design domain, Koppen et al. have chosen to use a through thickness cross section of the mirror mount. This results in interesting compliant mechanism-like structures that keep the top surface flat under thermal loads. Figure 6.3 shows the initial setup of the optimization problem in (a). The objective is to minimize the mean squared error of the optical surface  $\Gamma$  under a heat load. Figure (b) shows the resulting optimized topology.

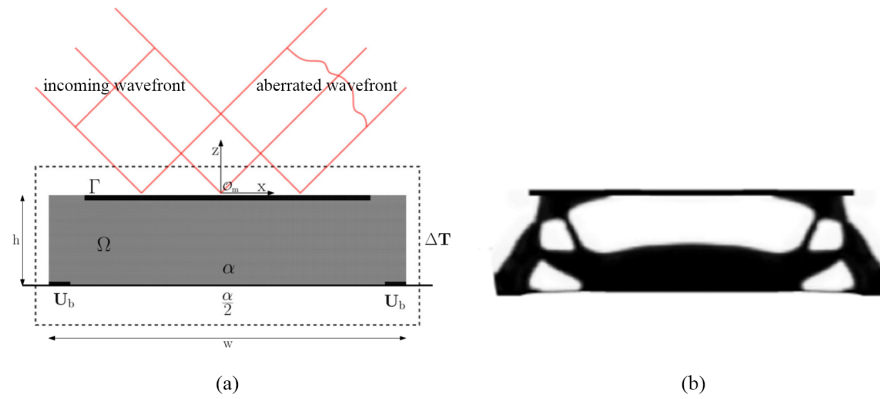


Figure 6.3: Figure of thermomechanical topology optimization from Koppen et al. [46]. (a) shows the setup of the optimization problem: domain  $\Omega$  is optimized to reduce the aberration of the outgoing wavefront when subjected to a thermal load. (b) shows the optimized topology.

As these examples from literature show, various tools and methods exist to evaluate and optimize the performance of optical instruments. Most research to date focuses on optimizing optical performance through thermomechanical topology optimization. The following chapters of this thesis deal with the optimization of the previously mentioned POB mirror. Instead of using thermomechanical TO, an investigation is made to improve the optical performance with thermofluid TO. The cooling channel layout is optimized with the GSP method. A number of concepts discussed above will be applied in evaluating the performance of the POB mirror. To reduce complexity, an optimization objective based on temperature uniformity is chosen as opposed to an objective directly related to deformations or optical performance. Details and reasoning behind this choice can be found in Section 7.1. In Chapter 9, an optimized design is analyzed for thermomechanical deformation. The mirror performance is evaluated by describing the deformation of the rectangular surface with polynomial surface fitting, analogous to the previously discussed Zernike polynomials.



## Problem description and model

In this chapter, a more detailed description of the POB mirror problem is provided. Section 7.1 explains the chosen objective. A hybrid 2-D/3-D model is introduced in Section 7.2, which is subsequently validated. As described in the introduction, the cooled POB mirror consists of a monolithic block of ultra low expansion glass (ULE glass) illustrated in Figure 7.1. Exact dimensions and shape are confidential, however, the mirror is constrained by a shoe-box model of  $0.8 \times 0.6 \times 0.1$  m. Since EUV lithography operates in vacuum conditions, heat transfer from the surface to the surroundings is minimal and incorporating it in the modeling does not impact the resulting designs; this mode of heat transfer is therefore neglected. The cooling channels have one inlet and one outlet and are located at least  $0.01$  m below the mirror surface such that boundary  $\Gamma_{\text{top}}$  is  $0.01$  m high. No hard constraints are placed on the available area for cooling channels or on the allowable pressure drop.

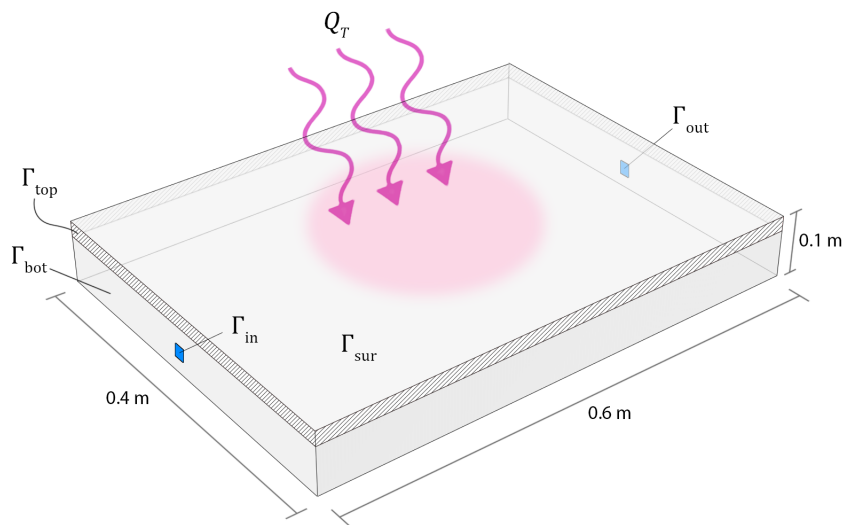


Figure 7.1: Shoebox model of the POB mirror.  $\Gamma_{\text{top}}$  and  $\Gamma_{\text{bot}}$  are separated based on the structure of the hybrid model. Thermal load  $Q_T$  represents the absorbed EUV radiation. Cooling channels run through the bottom slab 10 mm below the surface.

### 7.1. Optimization objective

The mirror device is made of a special kind of ultra low thermal expansion glass. By using a specific ratio of material components, it is possible to create a material that has zero thermal expansion around a specific “zero-crossing” temperature, see for example [39]. However, this means that the CTE is dependent on temperature.

To accurately model this, a nonlinear FEM model is required which increases the complexity of the FEM code and the topology optimization. A compromise was found by taking the temperature uniformity of the mirror surface as a proxy for thermal deformation. This is quantified by taking the mean square error (MSE) of all the nodal temperatures on the surface of the mirror. Evidently, temperature uniformity to thermal distortion is not a one-to-one relationship. However, depending on the boundary conditions, high temperatures and non-uniform heating will cause excessive mechanical distortions, whereas complete temperature uniformity would result in zero distortion. Hence, optimizing for temperature uniformity is a reasonable compromise to reduce complexity.

## 7.2. Hybrid model

Initially, a 2-D model similar to the numerical examples in Section 4.4 was investigated. The 2-D nature of this model means that the radiative heat transfer to the mirror surface is simulated through volumetric heating. In reality we are dealing with radiative heating onto a plate, and further conduction and convection from the plate into a heatsink below. Heating the top surface of this setup with two stacked slabs can yield drastically different temperature distributions as compared to the 2-D model. For example, the thickness of the mirror layer will smear out or “blur” the temperature profile such that the top surface has a more uniform temperature. For this reason and other possibly unforeseen effects the choice was made to create a 3-D model. A simplified representation of the custom 3-D model can be seen in Figure 7.2. The model consists of two layered slabs: the bottom slab contains the cooling channels while the top slab represents the mirroring layer. The bottom cooling slab is still modeled in 2-D as described in Part I, but the top slab is now a 3-D solid layer. The top and bottom slabs exchange heat through their shared rectangular interface based on heat transfer coefficients that are a function of the densities in the bottom layer. This setup is explained in more detail in the next section. The cooling channel topology of the bottom slab is optimized, while the objective function uses the temperatures on the top surface of the upper slab.

It is important to note that the dimensions of the shoebox model (Figure 7.1) will be slightly different as a consequence of using the hybrid model approach. Both the solid top slab, and the channel domain slab are 0.01 m thick. The remaining 0.08 m thick solid material underneath the mirror is ignored, as this would require an additional coupled 3-D FEM layer. Due to time restrictions, a compromise was made whereby the shoebox thickness is now taken as 0.02 m instead of 0.1 m. It is assumed that the remaining 0.08 m thick bottom slab has negligible influence on the top surface temperatures relative to the effect of the cooling channels directly below the surface. The increased surface area of the full thickness shoebox is expected to slightly reduce temperatures by means of additional surface to ambient heat transfer. In Chapter 9, the thermomechanical deformation for the full thickness shoebox model is evaluated using FEM. An optimized design is compared to a reference design and a non-cooled design. The results give an indication of whether the assumptions for the hybrid model and objective are warranted. Additionally, in Section B.3 of Appendix B, a comparison is shown for two different thicknesses of the mirror, confirming the prediction of raised temperatures for the thinner mirror.

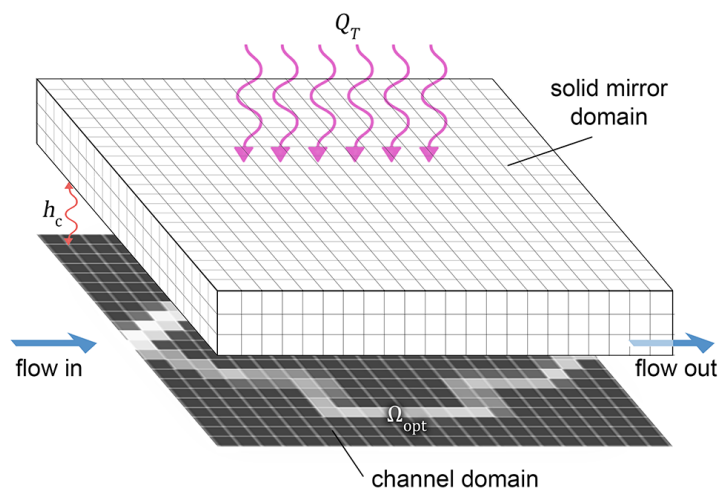


Figure 7.2: Hybrid 2-D/3-D model. EUV radiation is represented by thermal load  $Q_T$  on the solid mirror domain. Heat transfer coefficients  $h_c$  couple the solid mirror domain to the channel domain.

### 7.2.1. Coupling of cooling slab and mirror slab

As mentioned previously, the heat transfer coefficients on the interface are determined based on the local densities of the bottom slab. This is done via the following process. Using nodal densities  $\bar{\rho}_i$  obtained through averaging the element densities, first the nodal thermal conductivity  $\bar{\kappa}_i$  for node  $i$  is calculated by interpolating between  $\bar{\kappa}_{\text{solid},i}$  and  $\bar{\kappa}_{\text{fluid},i}$  with:

$$\bar{\kappa}_i = \bar{\rho}_i \cdot \bar{\kappa}_{\text{solid},i} + (1 - \bar{\rho}_i) \bar{\kappa}_{\text{fluid},i}, \quad (7.1)$$

where  $\bar{\kappa}_{\text{solid}}$  and  $\bar{\kappa}_{\text{fluid}}$  are the nodal thermal conductivities for the solid material and the cooling fluid. Subsequently, the diffusion heat transfer coefficient for stationary material (solid or liquid) is calculated as:

$$\bar{h}_{c,\text{stat},i} = \frac{\bar{\kappa}_i}{0.5 t_{\text{bot}}}, \quad (7.2)$$

with  $t_{\text{bot}}$  being the thickness of the bottom slab. The heat transfer coefficient for the *moving* fluid is

$$\bar{h}_{c,\text{mov},i} = \frac{\text{Nu} \cdot \bar{\kappa}_{\text{fluid},i}}{t_{\text{bot}}} \cdot \sigma(\gamma(|\bar{\mathbf{v}}_i| - v_{\text{act}})), \quad (7.3)$$

where Nu is the Nusselt number for laminar flow in wide rectangular channels (Nu = 0.568) [53], and  $\sigma(\gamma(|\bar{\mathbf{v}}_i| - v_{\text{act}}))$  is a sigmoid function that operates as a smoothed Heaviside step function and activates  $h_{\text{mov}}$  when the activation velocity  $v_{\text{act}}$  is reached. Sharpness factor  $\gamma$  determines the steepness of  $\sigma$ . Since the heat transfer coefficient of laminar flow does not depend on the flow velocity,  $\gamma$  is only used to discriminate between stationary and moving fluid, and can therefore be chosen arbitrarily large. The final local heat transfer coefficient is then calculated as:

$$\bar{h}_{c,i} = \bar{\rho}_i \cdot \bar{h}_{c,\text{stat},i} + (1 - \bar{\rho}_i) \bar{h}_{c,\text{mov},i}. \quad (7.4)$$

A diagonal matrix  $\mathbf{C}(\boldsymbol{\rho}, \mathbf{v})$  is created with the heat transfer coefficients multiplied with the element surface area  $hb$  on the diagonal:

$$\mathbf{C}(\boldsymbol{\rho}, \mathbf{v}) = hb \cdot \begin{bmatrix} \bar{h}_{c,1} & & \\ & \ddots & \\ & & \bar{h}_{c,n} \end{bmatrix}. \quad (7.5)$$

Matrix  $\mathbf{C}$  is used in the following equations:

$$\mathbf{K}_{\text{top}} \boldsymbol{\theta}_{\text{top}} = \mathbf{q}_T - \mathbf{C}_L(\boldsymbol{\rho}, \mathbf{v})(\boldsymbol{\theta}_{\text{bot,ext}} - \boldsymbol{\theta}_{\text{top}}) \quad (7.6)$$

$$\mathbf{K}_{\text{bot}} \boldsymbol{\theta}_{\text{bot}} = \mathbf{C}(\boldsymbol{\rho}, \mathbf{v})(\boldsymbol{\theta}_{\text{bot}} - \boldsymbol{\theta}_{\text{top,int}}), \quad (7.7)$$

where  $\boldsymbol{\theta}_{\text{top}}$  are the temperatures of the entire top slab, and  $\boldsymbol{\theta}_{\text{top,int}}$  the top slab temperatures on the coupled interface. The temperatures in the bottom slab are denoted with  $\boldsymbol{\theta}_{\text{bot}}$ , with  $\boldsymbol{\theta}_{\text{bot,ext}}$  an extended vector of the same size as  $\boldsymbol{\theta}_{\text{top}}$  containing only temperatures of the bottom slab. Finally  $\mathbf{C}_L$  is an enlarged version of  $\mathbf{C}$ :

$$\mathbf{C}_L = \begin{bmatrix} \mathbf{C} & \mathbf{0} \\ \mathbf{0} & \mathbf{0} \end{bmatrix} \quad (7.8)$$

Equations 7.7 are solved by creating a coupled matrix system of equations to solve for the temperatures in the top and bottom slab simultaneously:

$$\underbrace{\begin{bmatrix} \mathbf{K}_{\text{top}} + \mathbf{C}_L & -\mathbf{C}_W \\ -\mathbf{C}_W^T & \mathbf{K}_{\text{bot}} + \mathbf{C} \end{bmatrix}}_{\mathbf{K}_H} \underbrace{\begin{bmatrix} \boldsymbol{\theta}_{\text{top}} \\ \boldsymbol{\theta}_{\text{bot}} \end{bmatrix}}_{\boldsymbol{\theta}_H} = \underbrace{\begin{bmatrix} \mathbf{q}_F \\ \mathbf{0} \end{bmatrix}}_{\mathbf{q}_H}, \quad (7.9)$$

with  $\mathbf{C}_W = [\mathbf{C} \quad \mathbf{0}]^T$ .

### 7.2.2. Validation

A test setup with a grid of channels is used to compare the hybrid model to an FEM model. Figure 7.3 shows the test setup, and Table 7.1 lists the chosen problem parameters. In COMSOL, the mirror is modelled as a stack of two rectangular slabs with a rectangular cooling water inlet indicated with the red circle in the inset in Figure 7.3(b). The results of the comparison can be seen in Figure 7.4. Figures 7.4(a) and 7.4(b) show the top surface temperatures relative to ambient for the hybrid and FEM models. Temperatures are sampled along the cut line shown in 7.4(c) and plotted in 7.4(d) for a quantitative comparison. The maximum relative difference along the cut line is 1.6% based on a temperature deviation of 5.2 K and a global maximum of 336.5 K. For the GSP model the projected flow velocity was multiplied by a factor 1.1. This was done to adjust the maximum temperature to correspond to the FEM model. Reasoning behind this correction factor is explained in Section 3.3.2.

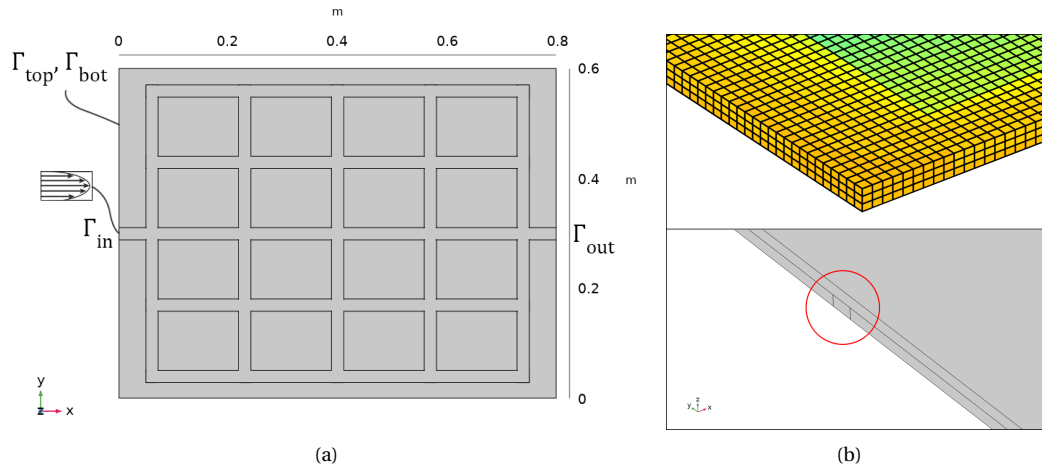


Figure 7.3: Setup for model validation. Figure (b) shows the top slab in Matlab and the model in COMSOL with the fluid channel entrance encircled.

<b>Dimensions</b>	0.8 x 0.6 x 0.02 m, top slab 0.01 m thick, channel width 0.01 m
<b>Material properties</b>	Solid (ULE glass), $\rho = 2210 \text{ kg m}^{-3}$ , $\kappa = 1.31 \text{ W m}^{-1} \text{ K}^{-1}$ , $C = 767 \text{ J kg}^{-1} \text{ K}^{-1}$
	Fluid (water), $\rho = 997 \text{ kg/m}^3$ , $\kappa = 0.6 \text{ W m}^{-1} \text{ K}^{-1}$ , $C = 4180 \text{ J kg}^{-1} \text{ K}^{-1}$
<b>Mesh</b>	COMSOL: physics controlled mesh (Element size: "Finer"), 398650 linear elements
	Matlab: linear elements, 144 x 96 quadrilaterals + 144 x 96 x 3 hexahedra
<b>Boundary conditions</b>	Thermal: inlet $\Delta T = 0 \text{ K}$ , $\Gamma_{top}$ and $\Gamma_{bot}$ insulated, uniform heat flux $250 \text{ W/m}^2$ on $\Gamma_{sur}$
	Fluid: inlet flow rate $q_{in} = 6 \text{ mL/min}$ (fully developed flow profile), outlet $p_{g,out} = 0 \text{ Pa}$

Table 7.1: Problem parameters for validation of the hybrid model.

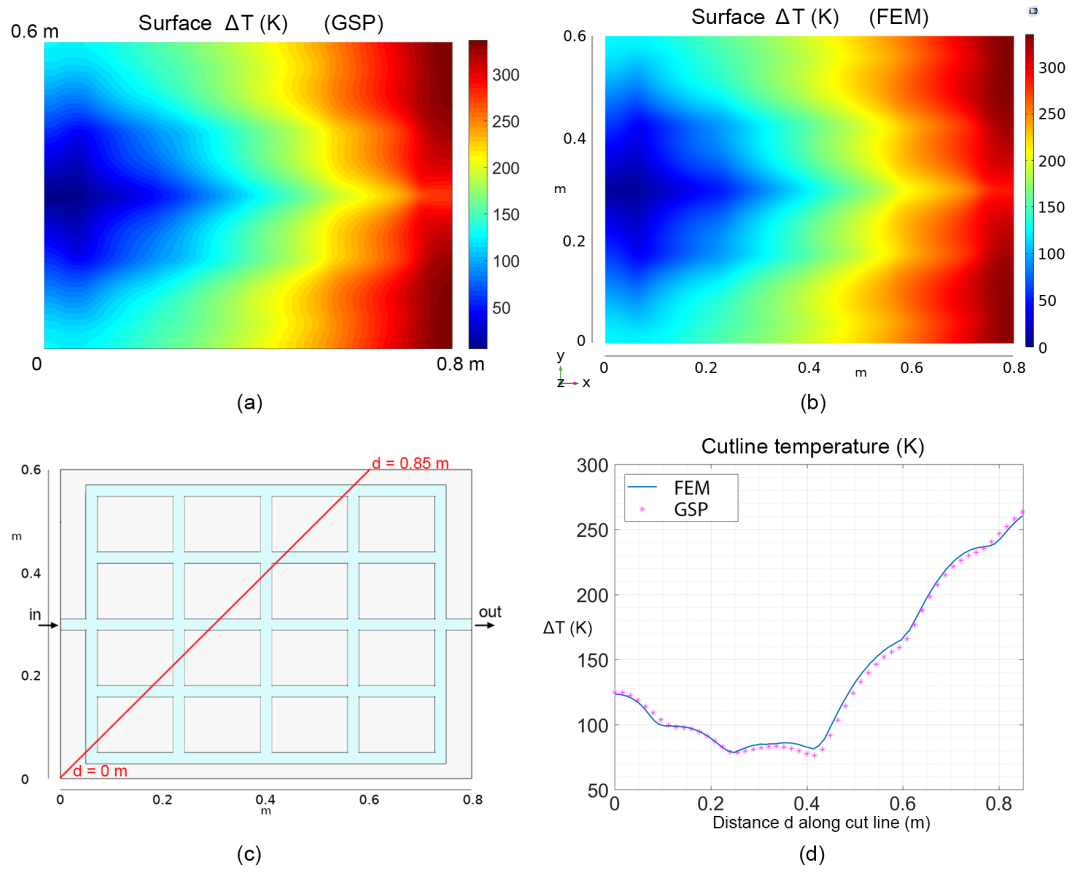
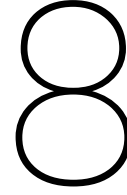


Figure 7.4: Comparison of temperature difference  $\Delta T = T - T_{\text{ambient}}$  for a hybrid 2-D/3-D GSP model versus a full 3-D FEM mode: (a) and (b) show the surface temperatures for the GSP and FEM models respectively. (c) Shows a cut line along which temperatures are sampled. In (d), the sampled temperatures along the cut line are plotted.





## POB mirror optimization results

In this chapter, the optimization results are shown and interpreted for the POB mirror subjected to two different heat loads: a single circular spot, and a dipole, both with a heat flux of  $250 \text{ W/m}^2$ . In Section 8.3 the practical utility of the designs is discussed as well as the prospect of a multi-objective optimization. Finally, Section 8.3.1 provides a glimpse of the performance gains that can be achieved when higher flow rates are used.

Based on observations, certain choices have been made in obtaining the results. In the absence of strict requirements on channel width and area, a maximum channel width of 16 mm and a channel area constraint factor of  $\frac{1}{9.5}$  (see Equations 8.1) are chosen to ensure minimal channel overlap and sparse designs. To allow for greater freedom in design, initially only the temperature uniformity objective is optimized for. At some point during the optimization process, the pressure drop objective is introduced to ensure that a clearly discernible channel layout is generated. This is done at 40% progress (after 48 iterations), as this value produced satisfactory results and good objective convergence, see Section B.1. No strict requirements on inlet flow rate were given, therefore a flow rate of  $10^{-7} \text{ m}^3/\text{s}$  or 6 mL/min was chosen to guarantee flow in the Stokes flow regime while still providing cooling capacity. Additional problem parameters are listed in Table 8.1. Furthermore, seven iterations of the divergence filter described in Section 3.3.3 were used, as well as an averaging filter with the kernel from the aforementioned section. Other details include a projection sharpness of  $s = 20$  (see Figure 3.3(a)), and a velocity correction factor of 1.1.

<b>Dimensions</b>	0.6 x 0.4 x 0.02 m, top slab 0.01 m thick
<b>Material properties</b>	Solid (ULE glass), $\rho = 2210 \text{ kg m}^{-3}$ , $\kappa = 1.31 \text{ W m}^{-1} \text{ K}^{-1}$ , $C = 767 \text{ J kg}^{-1} \text{ K}^{-1}$
	Fluid (water), $\rho = 997 \text{ kg/m}^3$ , $\kappa = 0.6 \text{ W m}^{-1} \text{ K}^{-1}$ , $C = 4180 \text{ J kg}^{-1} \text{ K}^{-1}$
<b>Mesh</b>	linear elements, 144 x 96 quadrilaterals + 144 x 96 x 3 hexahedra
<b>Ground structure</b>	Delauny triangulation of 30 x 21 nodes, 1791 branches
<b>Boundary conditions</b>	Thermal: inlet $\Delta T = 0 \text{ K}$ , $\Gamma_{\text{top}}$ and $\Gamma_{\text{bot}}$ insulated, heat flux of $Q_T = 250 \text{ W/m}^2$
	Fluid: inlet flow rate $q_{\text{in}} = 6 \text{ mL/min}$ (fully developed flow profile), outlet $p_{g,\text{out}} = 0 \text{ Pa}$

Table 8.1: Problem parameters and boundary conditions for the POB mirror optimization routine.

### 8.1. Use case 1: Circular heat load

In the first use case, a single circular spot with radius  $r_Q = 0.095$  m is heated with a prescribed heat flux of  $250$  W/m<sup>2</sup>, see Figure 8.1. Some padding is added around the mirror domain for practical implementation reasons. The padding has a minimal density to reduce heat transfer to the boundaries. Boundary  $\Gamma_{\text{pad}}$  has ambient temperatures prescribed with the exception of outlet  $\Gamma_{\text{out}}$ . The optimization problem is stated as follows:

$$\begin{aligned}
 \min_{\chi} : h(\chi) &\equiv \frac{1}{n} \sum_{i=1}^n (T_i - T_{\text{avg}})^2 + \alpha(p_{\text{in}} - p_{\text{out}}) \\
 \text{subject to} : \mathbf{K}_F(\chi)\mathbf{p} &= \mathbf{q}_F \\
 &: \mathbf{K}_H(\chi)\boldsymbol{\theta}_H = \mathbf{q}_H \\
 &: \sum_{i=1}^m \chi_i \leq \frac{m}{9.5} \chi_{\text{max}} \\
 &: 1 \mu\text{m} \leq \chi_i \leq 8 \text{ mm}
 \end{aligned} \tag{8.1}$$

As a base measure the temperature uniformity is first evaluated without any flow resulting in a temperature uniformity of  $\text{MSE} = 218.1 \text{ K}^2$  (see Section B.2 in Appendix B for an image of the temperature distribution). Hereafter, an inlet flow of  $6 \text{ mL/min}$  is introduced and the GSP method is applied to optimize the topology. Figure 8.2 shows the results for a range of pressure drop objective weights  $\alpha$ . The temperature uniformity performance for the three different weightings are visible in the last column. As expected, the MSE performance improves when smaller emphasis is placed on the pressure drop objective. The optimized designs also yield a significant improvement over the reference design. However, the actual design principles are not entirely obvious at first sight. Looking at the results, it appears that for higher values of  $\alpha$  the cooling channels converge to the right of the circular heat load. On the left side and in the center of the heat load, the channels are thinner. A possible explanation for this behavior is that the surface area of the cooling channels is maximized in areas where temperature is high. Since the cooling fluid is moving and simultaneously acquiring heat from left to right, the hottest part of the mirror surface is shifted rightwards. Keeping this in mind, it makes sense to reduce heat uptake on the left side of the heated spot by minimizing channel surface area, while at the same time maximizing heat uptake on the right side of the center by maximizing channel surface area.

### 8.2. Use case 2: Dipole

The second use case has two circular spots with a prescribed heat flux of  $250 \text{ W/m}^2$ , see Figure 8.3. Temperature uniformity is first evaluated without flow, which results in an MSE value of  $135.9 \text{ K}^2$ . When fluid flow is introduced, the channel layout is optimized for temperature uniformity and pressure drop. Apart from the dipole heat load, the optimization problem is unchanged from Eq. 8.1. Figure 8.4 shows the results for the reference design and the optimized designs with different pressure objective weights.

Again as expected, temperature uniformity improves when less emphasis is placed on the pressure drop objective. The resulting topologies appear to follow the same design principles as the circular heat load case. In all three optimized topologies the cooling channels coalesce and widen right underneath the hottest areas on the right side of the dipole. The topology for  $\alpha = 10^2$  has less clearly defined channels. An attempt was made to remove the leftover thin channels for  $\alpha = 10^2$  using a form of gray penalization on intermediate channel widths. However, this did not give the desired results. Further research could focus on a penalty on a specific range of small channel widths, or the use of filters and projections similar to density based TO [34, 96].

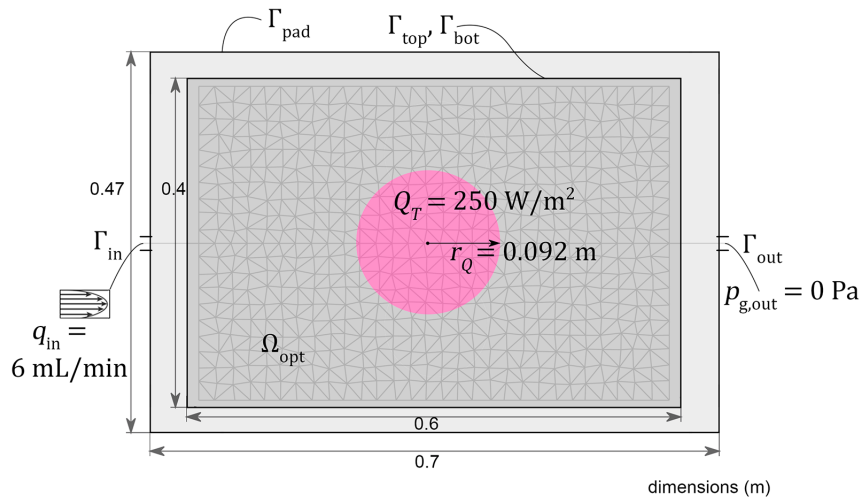


Figure 8.1: Problem setup and boundary conditions for the POB mirror optimization with a circular heat load. Outlet pressure  $p_{g,out}$  is gauge pressure, i.e. relative to ambient pressure.

$\alpha$	Density $\rho$	Velocity (mm/s)	Temperature (K)	MSE	$\Delta p$
ref				39.2	75.9
$10^4$				21.1	27.5
$10^3$				18.9	40.2
$10^2$				13.9	71.0

Figure 8.2: Reference design and optimized designs for a POB mirror subject to an circular heat load. Density fields, velocities, and temperature distributions ( $T - T_{ambient}$ ) are shown for different pressure drop objective weights  $\alpha$ . The two columns on the right show the resulting objective values. As pressure drop objective weight  $\alpha$  decreases, the temperature uniformity (MSE) improves.

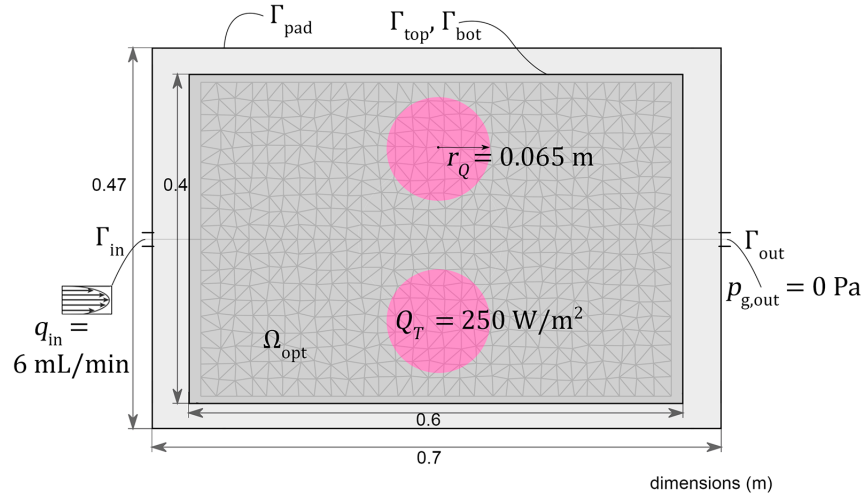


Figure 8.3: Problem setup and boundary conditions for the POB mirror optimization with a dipole heat load. Outlet pressure  $p_{g,out}$  is gauge pressure, i.e. relative to ambient pressure.

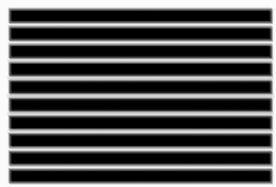
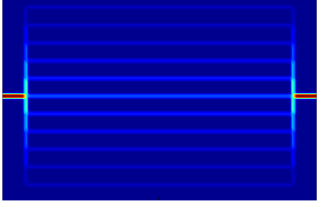
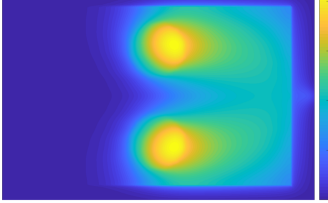
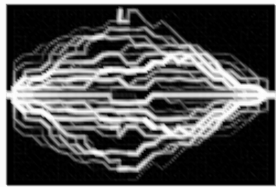
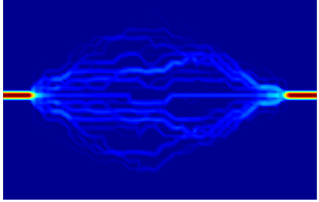
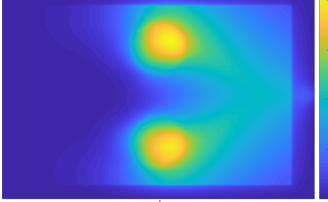
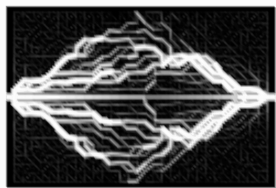
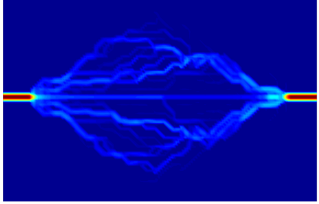
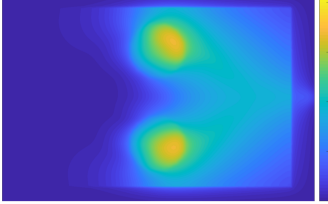
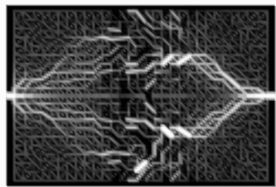
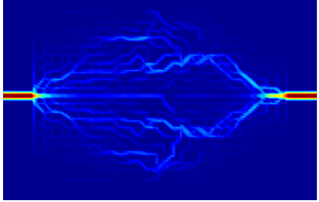
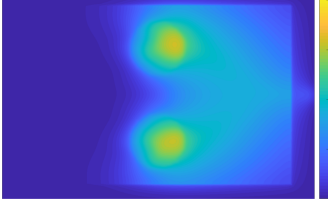
$\alpha$	Density $\rho$	Velocity (mm/s)	Temperature (K)	MSE	$\Delta p$
ref				35.5	75.9
$10^4$				27.1	32.1
$10^3$				20.1	36.0
$10^2$				17.8	75.3

Figure 8.4: Reference design and optimized designs for a POB mirror subject to a dipole heat load. Density fields, velocities, and temperature distributions ( $T - T_{ambient}$ ) are shown for different pressure drop objective weights  $\alpha$ . The two columns on the right show the resulting objective values. As pressure drop objective weight  $\alpha$  decreases, the temperature uniformity (MSE) improves.

### 8.3. Practical use and multi-objective optimization

The designs seen in the previous sections are very much tailored to the specific heat load in question. Even better results could most likely be acquired if the flow inlets and outlets are also located at favorable positions, e.g. inlets directly below heated spots. In practice however, the mirror device will be used for a number of different heat loads, and the cooling channel layout has to work well for all situations. Considering this, it would be useful to do a multi-objective optimization. Time restrictions did not allow this to be implemented; the code would have to be extended to run multiple simulations in a single iteration, and the computation of the sensitivities would also have to be adjusted. However, it is possible to give an educated guess about what a multi-objective optimized design will look like.

Applying the same design strategy to a multi-objective optimization will most likely result in a straightforward, “diluted” design. The expected result would be a design where most channel surface area is placed underneath the spots that are hottest on average for a number of different heat loads. Hence, if there are numerous of distinct heat loads that have to be accounted for, the optimized design will probably not differ much from a channel layout that keeps the mirror the coolest under a full uniform heat load. It could still be possible to gain some performance in terms of temperature uniformity versus a standard straight cooling channel layout. However, one must consider that the actual performance gain in terms of thermomechanical distortions might be negligible. Other possible solutions are discussed in the conclusions and recommendations.

#### 8.3.1. Increasing the cooling capacity

While the optimized designs offer improved temperature uniformity over a non-optimized design, the final performance can still be improved considerably by increasing the inlet flow. This is a simple consequence of lowered maximum temperatures. Unfortunately, as of now the GSP method only works with Stokes flow, and any increase of the flow velocity will result in inaccurate results. Regardless of the inaccuracies, an experiment with higher inlet flows might still provide valuable insight into potential performance gains. Another optimization was therefore done using the Stokes flow equations, but with a flow rate outside of the Stokes flow regime. Figure 8.5 shows an example of the circular heat load case where the inlet flow is increased to 600 mL/min. Increasing the thermal capacity of the water by a hundred fold will yield the same results. Compared to the creeping flow results, the highest temperatures are much lower now. As a consequence, the MSE is reduced to  $0.61 \text{ K}^2$ , which is a significant improvement over the creeping flow results.

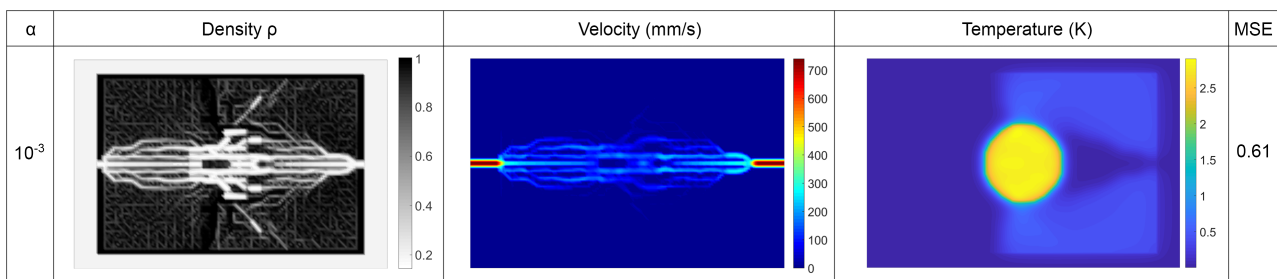


Figure 8.5: Topology optimization results for a POB mirror subject to a circular heat load and a high inlet flow (600 mL/min). Stokes flow equations are used which assume creeping flow, thus the resulting velocities are inaccurate. Despite inaccuracies, the results show the potential for performance gains with higher inlet flow.

The design in Figure 8.5 suggests that for high flow rates it is beneficial to create wide channels directly underneath the heat load, while simultaneously reducing channel width in other areas. With the high flow rate, the cooling fluid hardly heats up, and there is no significant smearing effect on the surface temperatures. Raised temperatures are very much concentrated in the direct heat load area. It does appear that the optimizer generated some sideways channel branches to disperse warmer cooling fluid towards unheated areas, thereby increasing temperature uniformity. However, the properties of the problem make it such that a leftover heat imprint remains. A problem that becomes clear from this experiment, is that the lower limit of the surface temperature is bounded by the fact that the heat has to be conducted through the thickness of the mirror layer; i.e. there will always be a temperature gradient from the top surface to the cooling channels based on Fourier’s law of thermal conduction. This means that when the flow speed (or the thermal capacity of the fluid) is increased, there will still be a remnant heat imprint.

**Cooled water**

An unsuccessful attempt was made to remove the leftover heat imprint by cooling down the fluid to below ambient temperatures. For flow velocities in the creeping flow regime, the cooled water resulted in a worse temperature uniformity performance compared to ambient temperature cooling fluid. This was primarily the result of the cooling fluid quickly warming up to ambient temperature when traversing the mirror domain, and as a result inlet temperatures were significantly colder than outlet temperatures. This phenomenon could be prevented by using a higher flow rate, however as previously explained, the current Stokes flow model is inaccurate at describing high Reynolds laminar flow.

## Finite Element Analysis of thermomechanical deformation

To evaluate the performance of optimized designs in terms of thermomechanical deformation, an optimized design was transferred to COMSOL using the 'Image to Curve' module. The optimized design is compared to a mirror with no flow, and a mirror with a reference design with seven parallel channels. The channel layouts can be seen in Figure 9.1. The outside dimensions of the mirror are based on the shoebox model in Figure 7.1. Thermal load  $Q_T$  is a uniform boundary heat flux of  $250 \text{ W/m}^2$  on the circled area with a radius of  $0.095 \text{ m}$ ;  $\Gamma_{\text{sur}}$  has a heat transfer coefficient of  $0.2 \text{ W/(m}^2\text{K)}$  and all other surfaces  $0.8 \text{ W/(m}^2\text{K)}$ . The cooling channels have a fixed height of  $0.01 \text{ m}$  and are restricted to  $0.01$  to  $0.02 \text{ m}$  below the mirror surface. Inlet flow rate is  $6 \text{ mL/min}$ .

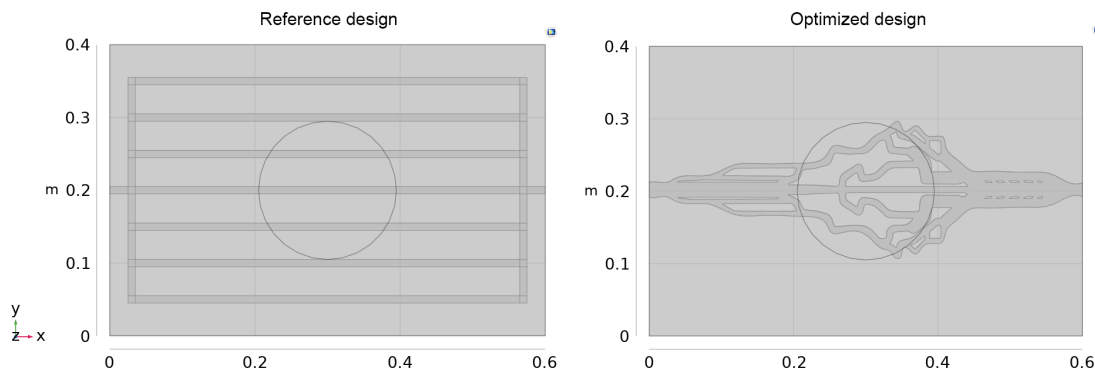


Figure 9.1: Channel layouts for a reference design and an optimized design generated with the GSP method. The circled area is subject to a heat load.

The resulting temperature distribution for the three designs can be seen in Figure 9.2. With a maximum temperature of  $15.0 \text{ K}$ , the optimized design gives the best results in terms of cooling performance. Note that increasing the thickness of the mirror from  $0.02 \text{ m}$  in the hybrid model to  $0.1 \text{ m}$  in the COMSOL model (as discussed in Section 7.2) results in a larger outer surface area, which in turn decreases the average temperatures in the block. This effect is most pronounced in the mirror setup without flow, however when active cooling is introduced the effect is small ( $1 \text{ K}$ ) since heat transfer now primarily occurs through the cooling fluid instead of the outer surface area.

A one-way coupling from the thermal domain to the mechanical domain is used to calculate the thermomechanical deformation. A constant coefficient of thermal expansion (CTE) is used of  $\alpha_T = 10^{-6} \text{ K}^{-1}$ . Since the surface is rectangular, the mechanical deformation is not described using Zernike polynomials (see Section 6.1). Instead, Matlab's curve fitting toolbox is used to fit a second order polynomial surface of the form:  $p_1x^2 + p_2y^2 + p_3xy + p_4x + p_5y + p_6$ . A second order polynomial is used because zeroth, first, and second order mechanical deformations can be compensated for by adjusting other components in the photolithography

machine. Figure 9.2 shows the second order surface fits together with the raw surface deformation at the mesh nodes plotted as a point cloud. Subsequently, the root mean square (RMS) of the residuals between the point cloud data and the fitted surface is used as a measure of performance. The optimized design has a 20% reduction in the RMS residual surface deformation compared to the reference design. The results suggest that temperature uniformity and/or a lower maximum temperature appear to transfer well to the residual deformation performance. It should be noted that the actual ULE glass material has a proprietary composition with a temperature dependent CTE. Therefore, the optimized design cannot be transferred directly to the actual POB mirror. Nonlinear finite element analysis, which takes a temperature dependent CTE into account, is advised for further investigations.

During a separate experiment (Section B.3) it was also observed that a thicker mirror will result in more predictable, local thermal expansion, whereas a thin design will tend to bulge upwards as a whole. This is likely due to the increased mechanical stiffness that comes with a thicker base slab.

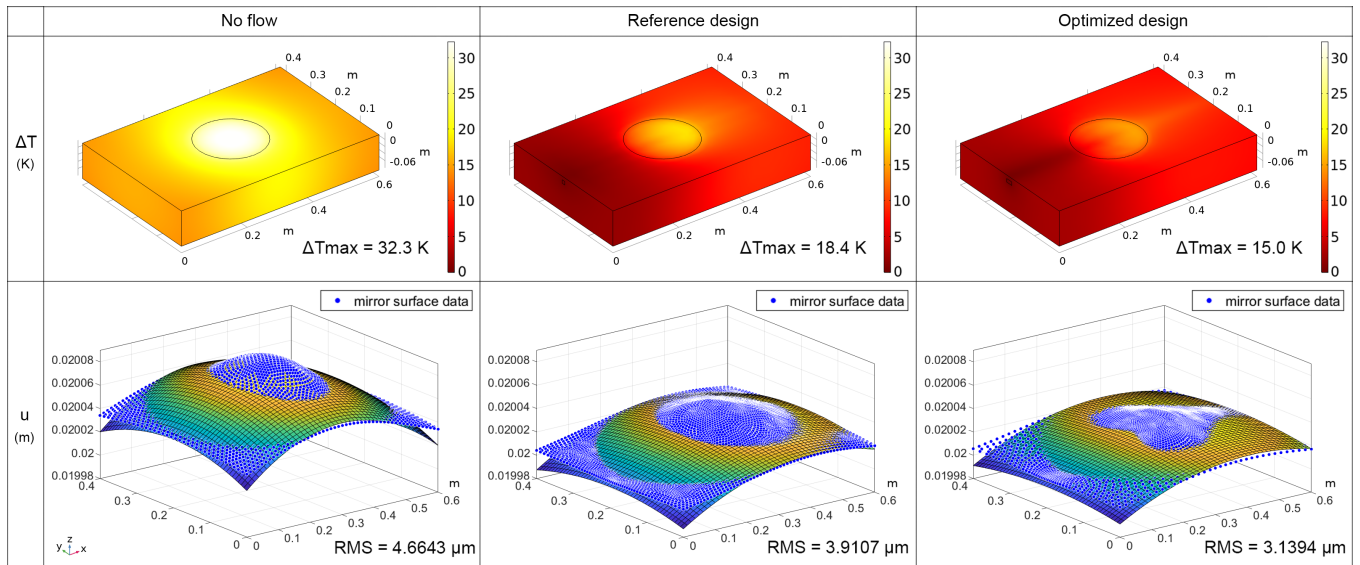


Figure 9.2: Temperature distributions and deformations for the POB mirror for three different designs. Top row shows the temperature relative to ambient temperature. Bottom row show the raw surface deformation as a point cloud, together with a fitted second order polynomial surface. Of the three designs the optimized design has a lowest maximum temperature, and the RMS of the residual deformation is the smallest.

# 10

## Conclusion and recommendations

### 10.1. Ground Structure Projection method

In this thesis, a new thermofluid TO method has been presented. Instead of solving the Stokes equation and changing FEM-element density directly, the GSP method uses a pipe flow network to compute flow velocity and subsequently projects the flow and geometry onto a structured grid FEM mesh. An averaging and a divergence reduction operator are applied to the projected flow field, after which the advection-diffusion equation is solved to find the temperature distribution. Spurious oscillations in the solution, associated with high Péclet advection-diffusion, are removed with the help of streamline upwind and crosswind stabilization terms, as well as the smoothing effect of the filter operators on the flow field.

Validation efforts show that the GSP method can reproduce temperature distributions that closely match solutions generated by a commercially available FEM package. Using a 128x128 element structured grid, local relative errors remained under 5% compared to an FEM solution. Applied to a problem of average temperature minimization in a heatsink device, the GSP method produces expected results and converges well. Similarly, an improved cooling channel layout was generated for an optical device. When analyzed with FEM, the optimized cooling channel layout resulted in a 20% reduction of the RMS surface deformation error compared to a reference design.

For the design of cooling channel layouts governed by Hagen-Poiseuille flow, the GSP method provides a number of benefits over density-based thermofluid TO. The strong reduction in the amount of DoFs required to solve the fluid physics translates to significantly faster computation compared to an FEM discretization of Stokes flow. This advantage would increase if the GSP method is extended to 3-D. Additionally, using an explicit description of the channel topology makes it possible to control high level features of the topology. Potential examples of feature control include channel curvature radius constraints, or branching constraints. Taking the above into account, the GSP method is best suited as a tool for initial design purposes. The computational advantage over density based TO, and the added explicit feature control allow for rapid generation of designs. Refinement for a final design and high accuracy simulations should be done using a full FEM discretization of the governing physics.

Care should be taken when applying the GSP method in its current form to problems with high thermally conductive solid materials. Very thin fluid channels with a width at or below mesh element size are not resolved properly. This results in too much diffusive heat transfer across the channel. Possible solutions to this problem would be density filtering and projection to remove the thinnest channels, or a form of gray penalization directly on the channel width design variables. It should be noted that this phenomenon occurs with any structured grid density based method if channel width is at or below element size.

Furthermore, the GSP method should only be applied to problems with low Reynolds flow and relatively thin and long channels, i.e. flow that can be reasonably approximated with pipe flow. While it is not necessary to restrict flow strictly to the creeping flow regime, it is advisable to only apply the GSP method to flow with Reynolds numbers below 20. To guarantee accuracy for higher Reynolds flow, a different fluid solver would be required that takes into account inertial effects and nonlinear relations between pressure drop and flow rate.

## 10.2. Projection Optics Box mirror

In cooperation with ASML, an investigation was done to improve the optical performance of a POB mirror using the developed TO method. The GSP method was used in combination with a hybrid model of the mirror where the channel domain was modeled in 2-D and the top layer in 3-D. For both a circular and a dipole heatload, the TO resulted in improved temperature uniformity and lower maximum temperatures over a reference design. Transferring an optimized and a reference design to COMSOL showed that thermomechanical deformation likewise improved in the optimized design.

Despite the apparent performance gains a few remarks have to be made. The GSP method is restricted to the creeping flow regime, which means that the channel layout for the actual mirror will have to be different when higher flow rates are used. At higher velocities inertial forces come into play and the fluid will not flow into side branches as freely as with creeping flow. However, certain design strategies might yet be distilled from the results generated by the GSP method. When designing the cooling channel layout for a system with creeping flow, it could be beneficial to have a slightly smaller channel width when entering a heated area, and a larger width on the exit side of the heated area. On the other hand, if the flow rate is high enough the cooling water will not heat up as much and there won't be a significant "smearing" effect of the surface temperatures. In such a case it would be preferable to increase channel width directly underneath heated areas, while minimizing channel width as much as possible in unheated areas. Furthermore, the Reynolds number can be lowered artificially in real life with parallel micro-channels which would increase the accuracy and utility of high inlet flow designs generated with the GSP method. Nevertheless, with a channel layout that is restricted to a level plane, the end result will be sub-optimal.

### Alternative solutions

While this thesis has shown that TO can provide performance improvements for specific heat loads, it is unknown how much TO can improve performance for a range of different heat loads simultaneously. A multi-objective optimization might yield a practical design that performs better than a reference design, however there are crucial obstacles that limit the potential gains. The POB mirror will be used for tens, if not hundreds of different heat loads that vary greatly in orientation and position. A channel layout optimized for this many use cases will likely be very generic. As such, performance gains over a reference design will most likely be marginal. Additionally, when new heat loads are introduced, the design would have to be changed. It is therefore recommended that ASML looks into other solutions that can cool locally and/or on demand.

Instead of a single optimized design, a more appropriate solution might be to have a grid/array of cooling units. This could be realized in multiple ways, for example by having a monolithic block with separate cooling channel in/outlets into every cooling cell. The flow rate into every cell can be adjusted dynamically, or be kept constant while the fluid is heated or cooled accordingly. Settings can either be controlled in real time, or be calculated beforehand with a parameter optimization on an accurate thermo-fluid-mechanical model. A third option would be to replace the cooling channels with an array of Peltier elements.

## 10.3. Future work

A number of aspects can benefit from extra research. The ground structures used in this thesis only have non-crossing pipe connections. Because of this, the resulting designs are dependent on the initial ground structure and still have room to be optimized further. For a more connected ground structure, measures have to be taken to avoid crossing and overlapping channels. This is feasible through the use of non-overlapping constraints or other forms of collision detection. A different approach to increasing the design freedom could be a "morphable" ground structure. In the current GSP implementation, the ground structure nodes are fixed. However, the nodes could be allowed to shift slightly during optimization, thus giving a greater range of possible designs.

Also requiring attention are the leftover gray/intermediate densities that remain under some circumstances. Penalization on intermediate channel widths has been tested during the making of this thesis. However, unlike gray density values, intermediate channel widths are not necessarily undesirable. Further work is needed for better results.

Furthermore, computational speed gains can be achieved by revising the initial phase where the "coverage" functions are generated. Before the optimization iterations start, the software routine has to determine the analytical coverage functions that couple the cooling channels to the mesh elements. At the time of writing this is done via brute force by iterating over every mesh element and every channel segment. This can be done much faster by making use of a rasterization algorithm in 2-D [14], or a voxel traversal algorithm in 3-D [5].

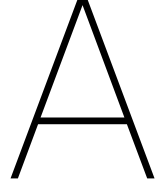
The channel geometry can be rasterized/voxelized to limit the search space for finding elements affected by specific channel segments. As for 3-D TO, the GSP method should be easily extendable to the third dimension. Obviously a greater range of problems can be solved in 3-D, and at the same time the computational advantage over Darcy-Stokes TO becomes larger.

Lastly, the concept of velocity mapping used in the GSP method could also prove useful in conjunction with other computational fluid dynamics methods or higher Reynolds laminar pipe flow. The velocity mapping itself can be improved by additional work on the divergence removal operator and a more sophisticated approximation of rectangular and shallow channel flow profiles.

Concerning the POB mirror, if TO investigations are continued, future work could be focused on a number of aspects. Significant performance gains should be possible when switching to 3-D TO such that cooling channels can move closer or further away from the surface depending on how much cooling capacity is needed in a specific area. Combined with pre-heating of unlit areas and/or air conditioning, it should be possible to get a high degree of temperature uniformity. Another approach to influence heat uptake in selected areas is to locally change the heat transfer coefficient by forcing the cooling fluid to mix. Static mixers can be placed in cooling channels underneath hot areas to reduce the temperature of the boundary layers of the flow and thereby increasing the heat transfer coefficient.

Another aspect that could benefit from future work is the optimization objective. While the chosen objective of temperature uniformity appears to translate well to thermomechanical deformation, it would make more sense to directly optimize for minimal optical aberration. For this purpose a thermomechanical coupling could be introduced in a 3-D model, with an objective based on the residual deformation. The temperature dependent thermal expansion coefficient of ULE glass would require TO with nonlinear finite element modeling. Furthermore, the introduction of transient physics and transient TO would be valuable, since ideally the POB mirror performs well in the transient phase immediately after the EUV heat load is activated. Finally, a practical design would require a multi-objective optimization for the most frequent heat loads.





# Sensitivity analysis

The sensitivities for the various responses are calculated using the adjoint method [36]. All stabilization terms are included in the sensitivities, however for brevity the thermal stiffness matrix  $\mathbf{K}_T$  is not expanded in the following derivation of sensitivities.

## A.1. Temperature response sensitivities

The 2-D model is based on the following equations:

$$\mathbf{K}_T \boldsymbol{\theta} = \mathbf{q}_T \quad (\text{A.1})$$

$$\mathbf{K}_F \mathbf{p} = \mathbf{q}_F, \quad (\text{A.2})$$

where it holds that:

$$\mathbf{K}_T \equiv \mathbf{K}_T(\boldsymbol{\rho}(\boldsymbol{\chi}), \mathbf{v}(\boldsymbol{\chi})) \quad (\text{A.3})$$

$$\mathbf{K}_F \equiv \mathbf{K}_F(\boldsymbol{\chi}). \quad (\text{A.4})$$

Given a response  $h(\boldsymbol{\theta})$ , using the adjoint method we introduce an augmented response function  $h^*(\boldsymbol{\theta})$  where we add the model equations multiplied with adjoint vectors  $\boldsymbol{\lambda}_1$  and  $\boldsymbol{\lambda}_2$ :

$$h^* = h + \boldsymbol{\lambda}_1^T (\mathbf{q}_T - \mathbf{K}_T \boldsymbol{\theta}) + \boldsymbol{\lambda}_2^T (\mathbf{q}_F - \mathbf{K}_F \mathbf{p}). \quad (\text{A.5})$$

Since the added terms in augmented response  $h^*$  are equal to zero, the derivatives w.r.t. the design variables remain unchanged, such that:

$$\frac{dh}{d\chi_i} = \frac{dh^*}{d\chi_i} = \quad (\text{A.6})$$

$$= \frac{\partial h}{\partial \chi_i} + \frac{\partial h}{\partial \boldsymbol{\theta}} \frac{d\boldsymbol{\theta}}{d\chi_i} + \boldsymbol{\lambda}_1^T \left[ \frac{d\mathbf{q}_T}{d\chi_i} - \left( \frac{d\mathbf{K}_T}{d\chi_i} \boldsymbol{\theta} + \mathbf{K}_T \frac{d\boldsymbol{\theta}}{d\chi_i} \right) \right] + \boldsymbol{\lambda}_2^T \left[ \frac{d\mathbf{q}_F}{d\chi_i} - \left( \frac{d\mathbf{K}_F}{d\chi_i} \mathbf{p} + \mathbf{K}_F \frac{d\mathbf{p}}{d\chi_i} \right) \right],$$

where three terms are crossed out because response  $h$  and loads  $\mathbf{q}_T$ ,  $\mathbf{q}_F$  are not explicit functions of the design variables. Since  $\mathbf{K}_F$  and  $\mathbf{K}_T$  are dependent on densities  $\boldsymbol{\rho}$  and velocities  $\mathbf{v}$ , the derivatives  $\frac{d\mathbf{K}_F}{d\chi_i}$  and  $\frac{d\mathbf{K}_T}{d\chi_i}$  can be expanded. Removing terms that are zero and expanding said derivatives, we get:

$$\begin{aligned}
&= \frac{\partial h}{\partial \boldsymbol{\theta}} \frac{d\boldsymbol{\theta}}{d\chi_i} - \boldsymbol{\lambda}_1^\top \left[ \left( \frac{\partial \mathbf{K}_\Gamma}{\partial \boldsymbol{\rho}} \frac{d\boldsymbol{\rho}}{d\chi_i} + \frac{\partial \mathbf{K}_\Gamma}{\partial \mathbf{v}_x} \left( \frac{d\mathbf{v}_x}{d\chi_i} + \frac{\partial \mathbf{v}_x}{\partial \mathbf{p}} \frac{d\mathbf{p}}{d\chi_i} \right) + \frac{\partial \mathbf{K}_\Gamma}{\partial \mathbf{v}_y} \left( \frac{d\mathbf{v}_y}{d\chi_i} + \frac{\partial \mathbf{v}_y}{\partial \mathbf{p}} \frac{d\mathbf{p}}{d\chi_i} \right) \right) \boldsymbol{\theta} + \mathbf{K}_\Gamma \frac{d\boldsymbol{\theta}}{d\chi_i} \right] \\
&- \boldsymbol{\lambda}_2^\top \left[ \left( \frac{d\mathbf{K}_F}{d\chi_i} \right) \mathbf{p} + \mathbf{K}_F \frac{d\mathbf{p}}{d\chi_i} \right]
\end{aligned}$$

Rearranging to group together all terms with state vector derivatives  $\frac{d\boldsymbol{\theta}}{d\chi_i}$  and  $\frac{d\mathbf{p}}{d\chi_i}$  gives:

$$\begin{aligned}
&= - \boldsymbol{\lambda}_1^\top \left( \frac{\partial \mathbf{K}_\Gamma}{\partial \boldsymbol{\rho}} \frac{d\boldsymbol{\rho}}{d\chi_i} + \frac{\partial \mathbf{K}_\Gamma}{\partial \mathbf{v}_x} \frac{d\mathbf{v}_x}{d\chi_i} + \frac{\partial \mathbf{K}_\Gamma}{\partial \mathbf{v}_y} \frac{d\mathbf{v}_y}{d\chi_i} \right) \boldsymbol{\theta} + \left( \frac{\partial h}{\partial \boldsymbol{\theta}} - \boldsymbol{\lambda}_1^\top \mathbf{K}_\Gamma \right) \frac{d\boldsymbol{\theta}}{d\chi_i} \\
&- \boldsymbol{\lambda}_2^\top \frac{d\mathbf{K}_F}{d\chi_i} \mathbf{p} - \left( \boldsymbol{\lambda}_2^\top \mathbf{K}_F + \boldsymbol{\lambda}_1^\top \left( \frac{\partial \mathbf{K}_\Gamma}{\partial \mathbf{v}_x} \frac{\partial \mathbf{v}_x}{\partial \mathbf{p}} + \frac{\partial \mathbf{K}_\Gamma}{\partial \mathbf{v}_y} \frac{\partial \mathbf{v}_y}{\partial \mathbf{p}} \right) \boldsymbol{\theta} \right) \frac{d\mathbf{p}}{d\chi_i}
\end{aligned} \tag{A.7}$$

To avoid calculating the state vector derivatives we set

$$\begin{aligned}
&\frac{\partial h}{\partial \boldsymbol{\theta}} - \boldsymbol{\lambda}_1^\top \mathbf{K}_\Gamma = \mathbf{0}, \\
&\boldsymbol{\lambda}_2^\top \mathbf{K}_F + \boldsymbol{\lambda}_1^\top \left( \frac{\partial \mathbf{K}_\Gamma}{\partial \mathbf{v}_x} \frac{\partial \mathbf{v}_x}{\partial \mathbf{p}} + \frac{\partial \mathbf{K}_\Gamma}{\partial \mathbf{v}_y} \frac{\partial \mathbf{v}_y}{\partial \mathbf{p}} \right) \boldsymbol{\theta} = \mathbf{0}
\end{aligned}$$

such that the adjoint vectors become

$$\boldsymbol{\lambda}_1 = \mathbf{K}_\Gamma^{-\top} \left( \frac{\partial h}{\partial \boldsymbol{\theta}} \right)^\top, \quad (\text{substitute } \boldsymbol{\lambda}_1 \text{ into A.9}) \tag{A.8}$$

$$\boldsymbol{\lambda}_2 = \mathbf{K}_F^{-\top} \left( -\boldsymbol{\lambda}_1^\top \left( \frac{\partial \mathbf{K}_\Gamma}{\partial \mathbf{v}_x} \frac{\partial \mathbf{v}_x}{\partial \mathbf{p}} + \frac{\partial \mathbf{K}_\Gamma}{\partial \mathbf{v}_y} \frac{\partial \mathbf{v}_y}{\partial \mathbf{p}} \right) \boldsymbol{\theta} \right)^\top, \tag{A.9}$$

Adjoint vectors  $\boldsymbol{\lambda}_1$  and  $\boldsymbol{\lambda}_2$  are then used in eq. A.7 so that we get the final result:

$$\frac{dh}{d\chi_i} = -\boldsymbol{\lambda}_1^\top \left( \frac{\partial \mathbf{K}_\Gamma}{\partial \boldsymbol{\rho}} \frac{d\boldsymbol{\rho}}{d\chi_i} + \frac{\partial \mathbf{K}_\Gamma}{\partial \mathbf{v}_x} \frac{d\mathbf{v}_x}{d\chi_i} + \frac{\partial \mathbf{K}_\Gamma}{\partial \mathbf{v}_y} \frac{d\mathbf{v}_y}{d\chi_i} \right) \boldsymbol{\theta} - \boldsymbol{\lambda}_2^\top \frac{d\mathbf{K}_F}{d\chi_i} \mathbf{p} \tag{A.10}$$

### A.1.1. Implementation challenges

The end result  $\frac{dh}{d\chi_i}$  is a scalar value obtained with a vector-matrix-vector product. However, calculating Equation A.10 or adjoint vector  $\boldsymbol{\lambda}_2$  can be challenging since matrix to vector derivatives such as  $\frac{\partial \mathbf{K}_\Gamma}{\partial \boldsymbol{\rho}}$  and  $\frac{\partial \mathbf{K}_\Gamma}{\partial \mathbf{v}_x}$  (eq. (A.9)) are ambiguous. Focusing on the computation of  $\boldsymbol{\lambda}_2$  in Equation A.9, care should be taken when calculating the following term:

$$\boldsymbol{\lambda}_1^\top \left( \frac{\partial \mathbf{K}_\Gamma}{\partial \mathbf{v}_x} \frac{\partial \mathbf{v}_x}{\partial \mathbf{p}} \right) \boldsymbol{\theta} \quad (\text{similar for } \mathbf{v}_y). \tag{A.11}$$

We know that Equation A.7 must be a scalar value, and the following term from eq. (A.7):

$$\boldsymbol{\lambda}_1^\top \left( \frac{\partial \mathbf{K}_\Gamma}{\partial \mathbf{v}_x} \frac{\partial \mathbf{v}_x}{\partial \mathbf{p}} \right) \boldsymbol{\theta} \frac{d\mathbf{p}}{d\chi_i} \tag{A.12}$$

can be written using index notation for vectors  $\mathbf{v}_x$  and  $\mathbf{p}$  as:

$$\boldsymbol{\lambda}_1^\top \frac{\partial \mathbf{K}_\Gamma}{\partial v_{x,j}} \frac{\partial v_{x,j}}{\partial p_k} \boldsymbol{\theta} \frac{dp_k}{d\chi_i}. \tag{A.13}$$

Hence eq. (A.11) can be seen as a row vector of the form:

$$\boldsymbol{\psi}_x^\top := \left[ \boldsymbol{\lambda}_1^\top \frac{\partial \mathbf{K}_T}{\partial \mathbf{v}_x} \frac{\partial \mathbf{v}_x}{\partial p_1} \boldsymbol{\theta} \quad \boldsymbol{\lambda}_1^\top \frac{\partial \mathbf{K}_T}{\partial \mathbf{v}_x} \frac{\partial \mathbf{v}_x}{\partial p_2} \boldsymbol{\theta} \quad \boldsymbol{\lambda}_1^\top \frac{\partial \mathbf{K}_T}{\partial \mathbf{v}_x} \frac{\partial \mathbf{v}_x}{\partial p_3} \boldsymbol{\theta} \quad \dots \quad \boldsymbol{\lambda}_1^\top \frac{\partial \mathbf{K}_T}{\partial \mathbf{v}_x} \frac{\partial \mathbf{v}_x}{\partial p_n} \boldsymbol{\theta} \right], \quad (\text{A.14})$$

such that  $\boldsymbol{\psi}_x^\top \frac{d p_k}{d \chi_i}$  would yield the same result as eq. (A.13). Note that  $\frac{\partial \mathbf{K}_T}{\partial \mathbf{v}_x} \frac{\partial \mathbf{v}_x}{\partial p_k}$  represents a sum of matrices:

$$\frac{\partial \mathbf{K}_T}{\partial \mathbf{v}_x} \frac{\partial \mathbf{v}_x}{\partial p_k} = \frac{\partial \mathbf{K}_T}{\partial v_{x,j}} \frac{\partial v_{x,j}}{\partial p_k}. \quad (\text{A.15})$$

Stencils are used for  $\frac{\partial \mathbf{K}_T}{\partial v_{x,j}}$  and  $\frac{\partial \mathbf{K}_T}{\partial v_{y,j}}$ , so that calculating the values of  $\boldsymbol{\psi}_x$  is performed by selecting the appropriate values from  $\boldsymbol{\lambda}_1$  and  $\boldsymbol{\theta}$  on the basis of a predetermined list that contains the corresponding element indices.

Now calculating adjoint vector  $\boldsymbol{\lambda}_2$  becomes easy:

$$\boldsymbol{\lambda}_2 = -\mathbf{K}_F^{-\top} (\boldsymbol{\psi}_x + \boldsymbol{\psi}_y). \quad (\text{A.16})$$

Similar procedures are used for calculating other parts of eq. (A.10).

Finally, the anti-divergence operator described in Section 3.3.3 requires the chain rule to be applied: if seven iterations of the operator are used on the velocities, then accordingly seven iterations are used on the sensitivities of the velocities.

## A.2. Hybrid model

The hybrid model of two stacked slabs used in Part II has its own difficulties. The advection-diffusion implementation described by Donea & Huerta [28] uses nodal temperatures combined with velocities at the element centers. The hybrid model however, transfers heat based on only nodal velocities, densities, and temperatures. The element center velocities and densities are therefore averaged to generate nodal values. Taking the derivative of the objective w.r.t the element densities  $\boldsymbol{\rho}$  or the element velocities  $\mathbf{v}$  has to account for this averaging step in the chain rule. This is solved by introducing an additional set of stencils determined beforehand. Depending on the location of an element (sides, corners, center) a different stencil will be used to compute the derivative of a response to an element density or velocity. Recalling Equation 7.9:

$$\underbrace{\begin{bmatrix} \mathbf{K}_{\text{top}} + \mathbf{C}_L & -\mathbf{C}_W \\ -\mathbf{C}_W^\top & \mathbf{K}_{\text{bot}} + \mathbf{C} \end{bmatrix}}_{\mathbf{K}_H} \underbrace{\begin{bmatrix} \boldsymbol{\theta}_{\text{top}} \\ \boldsymbol{\theta}_{\text{bot}} \end{bmatrix}}_{\boldsymbol{\theta}_H} = \underbrace{\begin{bmatrix} \mathbf{q}_F \\ \mathbf{0} \end{bmatrix}}_{\mathbf{q}_H},$$

matrix  $\mathbf{C}$  is a diagonal matrix which contains the heat transfer coefficients that couple the two slabs. Thus  $\mathbf{C}$  is indirectly (via nodal densities  $\bar{\boldsymbol{\rho}}$  and nodal velocities  $\bar{\mathbf{v}}$ ) a function of element densities  $\boldsymbol{\rho}$  and element velocities  $\mathbf{v}$ , i.e.  $\mathbf{C} = \mathbf{C}(\bar{\boldsymbol{\rho}}(\boldsymbol{\rho}), \bar{\mathbf{v}}(\mathbf{v}))$ . Taking the derivative to an element density  $\rho_i$  will result in a stencil:

$$\frac{\partial \mathbf{C}}{\partial \rho_i} = \frac{\partial \mathbf{C}}{\partial \bar{\boldsymbol{\rho}}_{\text{rel}}} \frac{d \bar{\boldsymbol{\rho}}_{\text{rel}}}{d \rho_i} \quad (\text{A.17})$$

where  $\frac{\partial \mathbf{C}}{\partial \bar{\boldsymbol{\rho}}_{\text{rel}}}$  is a 4x4 diagonal matrix containing the derivatives with regards to selected relevant nodal densities  $\bar{\boldsymbol{\rho}}_{\text{rel}}$ , and  $\frac{d \bar{\boldsymbol{\rho}}_{\text{rel}}}{d \rho_i}$  is a 4x4 matrix which changes depending on the location (sides, corners, center) of the element in question. Equation A.17 becomes:

$$\frac{\partial \mathbf{C}}{\partial \rho_i} = \begin{bmatrix} \frac{\partial \mathbf{C}_a}{\partial \bar{\rho}_a} & 0 & 0 & 0 \\ 0 & \frac{\partial \mathbf{C}_b}{\partial \bar{\rho}_b} & 0 & 0 \\ 0 & 0 & \frac{\partial \mathbf{C}_c}{\partial \bar{\rho}_c} & 0 \\ 0 & 0 & 0 & \frac{\partial \mathbf{C}_d}{\partial \bar{\rho}_d} \end{bmatrix} \begin{bmatrix} \frac{\partial \bar{\rho}_a}{\partial \rho_i} & 0 & 0 & 0 \\ 0 & \frac{\partial \bar{\rho}_b}{\partial \rho_i} & 0 & 0 \\ 0 & 0 & \frac{\partial \bar{\rho}_c}{\partial \rho_i} & 0 \\ 0 & 0 & 0 & \frac{\partial \bar{\rho}_d}{\partial \rho_i} \end{bmatrix}, \quad (\text{A.18})$$

where  $\{a, b, c, d\}$  denote the four corners of an element. As an example, since an element along the top boundary will influence two top boundary nodes with half of its value, and two center nodes with a quarter of

its value,  $\frac{d\bar{\rho}_{\text{rel}}}{d\rho_i}$  becomes:

$$\frac{d\bar{\rho}_{\text{rel}}}{d\rho_i} = \begin{bmatrix} 1/2 & 0 & 0 & 0 \\ 0 & 1/2 & 0 & 0 \\ 0 & 0 & 1/4 & 0 \\ 0 & 0 & 0 & 1/4 \end{bmatrix}. \quad (\text{A.19})$$

# B

## Additional data

### B.1. POB-mirror convergence plots

Convergence plots of the two topology optimization cases (circular and dipole heat load) described in Chapter 8. Different pressure drop objective weights  $\alpha$  are shown: lower values of  $\alpha$  yield results with better temperature uniformity.

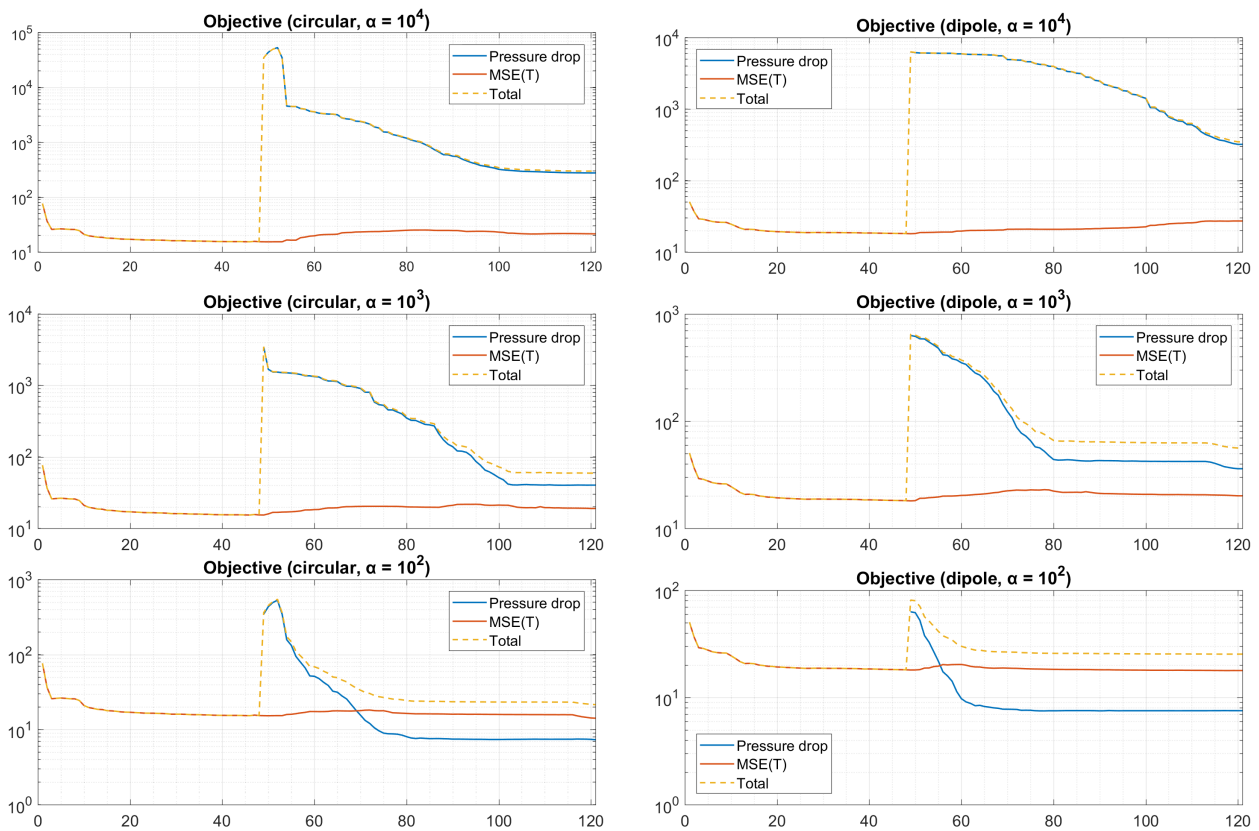


Figure B.1: Convergence plots for POB-mirror. Pressure drop objective is scaled with  $\alpha$ . Circular heat load on the left, dipole heat load on the right.

## B.2. Temperature distribution with zero flow

Temperature distributions of the POB mirror with zero flow, subject to a circular and dipole heat load as described in Chapter 8.

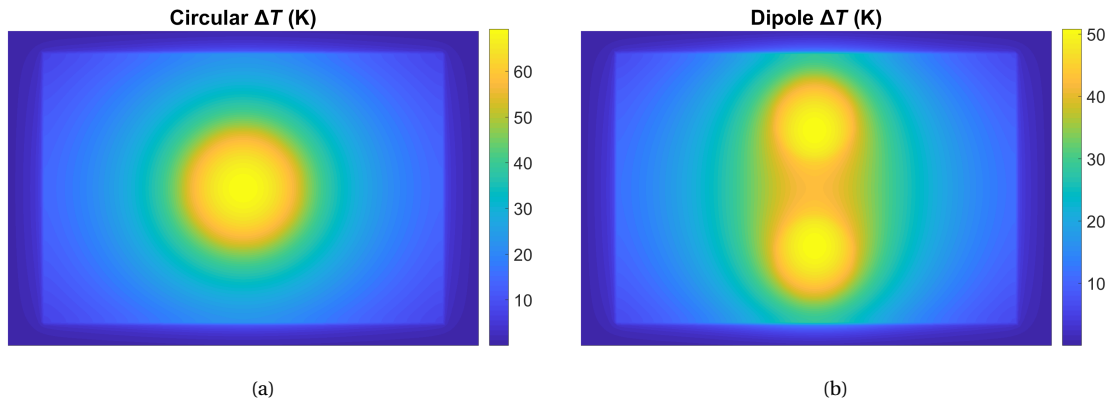


Figure B.2: Temperature distribution with no flow. Left circular heat load, right dipole heat load.

## B.3. Shoebox model thickness comparison

To validate the assumptions made in Section 7.2, a test was performed with a varying thickness bottom slab. Figure B.3(a) shows the temperature distribution of a thin shoebox model: 0.02 m thick (0.01 m top layer, 0.01 m cooling channel layer). Figure B.3(b) shows the full thickness shoebox model of 0.1 m thickness (0.01 m top layer, 0.01 m cooling channel layer, 0.08 m solid bottom layer). The top surface temperatures are roughly 1 K higher for the thin model compared to the thick model. This is likely a consequence of the increased surface to surroundings heat transfer for the thick model.

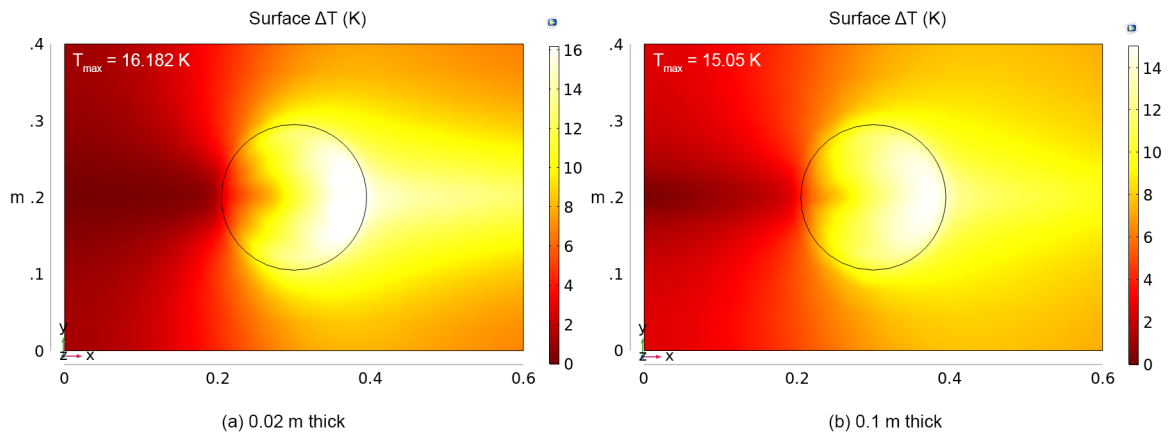


Figure B.3: Comparison of temperatures for two different thickness shoebox models. Increasing the thickness results in slightly lower temperatures and a more uniform temperature distribution.

# C

## Validation

This appendix contains additional GSP vs. FEM validation examples for a number of cases. A Y-split channel structure is compared for different channel widths and two different solid material thermal conductivities. Furthermore, a single tapered channel is tested.

### C.1. Y-split channel structure

A Y-split channel structure provides insight into whether diagonal and non-mesh aligned channels are properly handled by the GSP method. Different channel widths  $w$  are tested, namely 0.01, 0.02, 0.03, and 0.04 m. Boundary conditions for the experiment are shown in Figure C.1. Around the inlet a fixed length portion of the boundary has a prescribed temperature of 0 K. A  $1000 \text{ W/m}^3$  uniform volumetric heat load is applied over the entire domain.

#### C.1.1. Temperature comparison

Figures C.2 and C.3 show the resulting temperature distributions for varying channel widths for a low and high thermally conductive material respectively. The GSP model and FEM model show good agreement for the low thermally conductive solid material in Figure C.2. However, in Figure C.3 a discrepancy can be observed for the layout with the thinnest channels (channel width of 0.01 m). The high resolution FEM model has a mesh tailored to the geometry. Therefore, the channels form an insulating, low conductivity layer in the domain. The GSP model, however, uses a structured grid mesh, where the thinnest channels are represented by intermediate densities. As a consequence, the channels no longer form a low conductive layer within the domain, and the resulting temperatures are distributed more uniformly. Also, because of this, a lower maximum temperature is seen. The comparisons are quantified in Figure C.4.

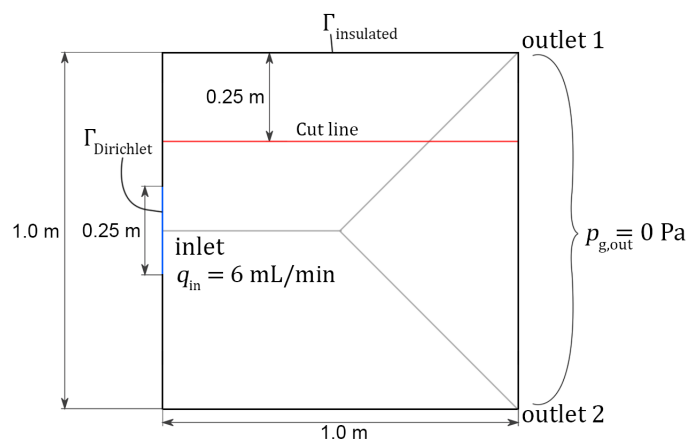


Figure C.1: Problem setup of Y-split channel validation. Prescribed temperature at  $\Gamma_{\text{Dirichlet}}$  is 0 K. Uniform volumetric heat load of  $1000 \text{ W/m}^3$ .

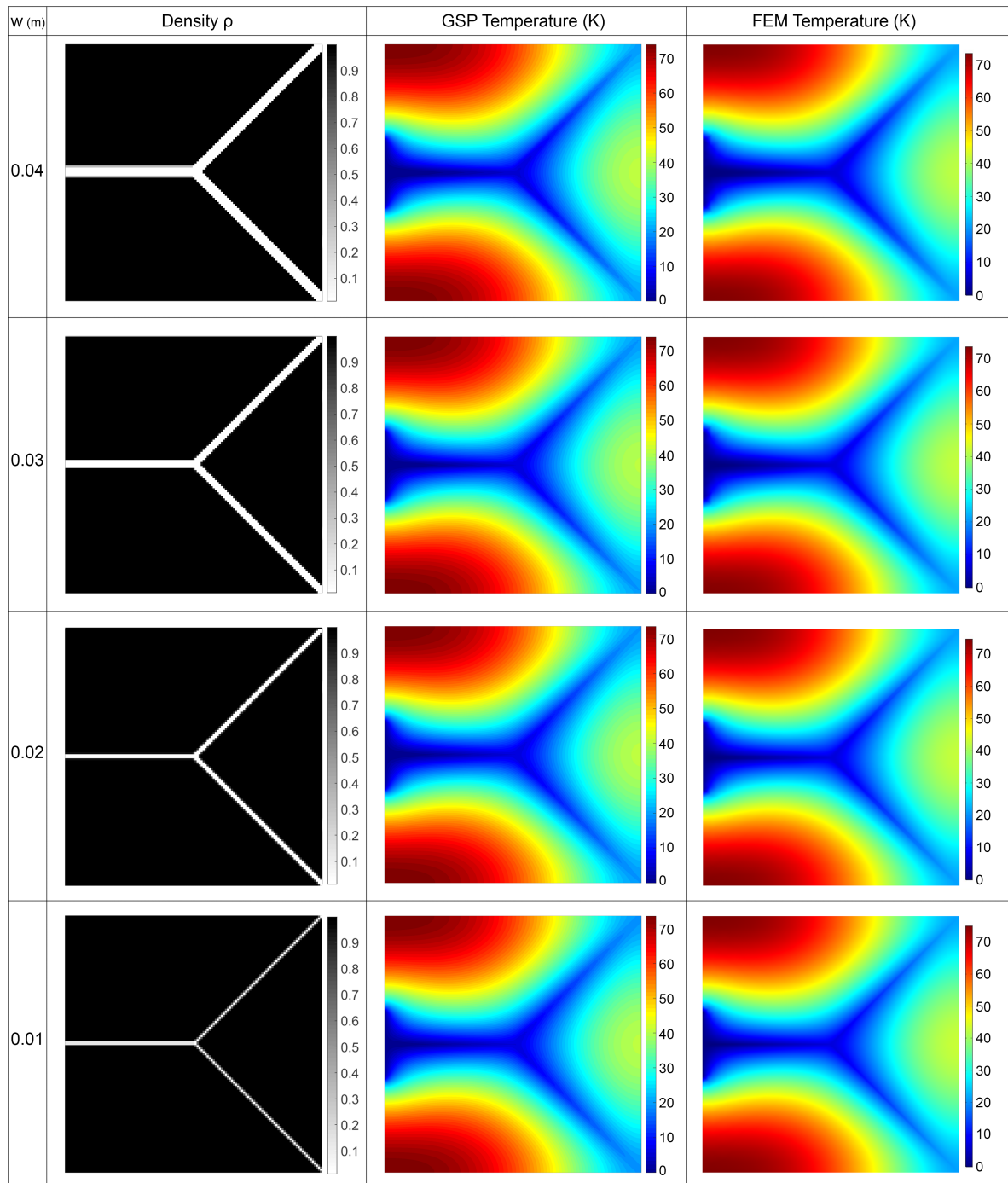


Figure C.2: GSP vs. FEM temperature comparison for a Y-split channel structure and low thermal conductive solid material ( $\kappa = 1.31 \text{ W m}^{-1} \text{ K}^{-1}$ ). Different channel widths  $w$  are shown. GSP and FEM models show good agreement.

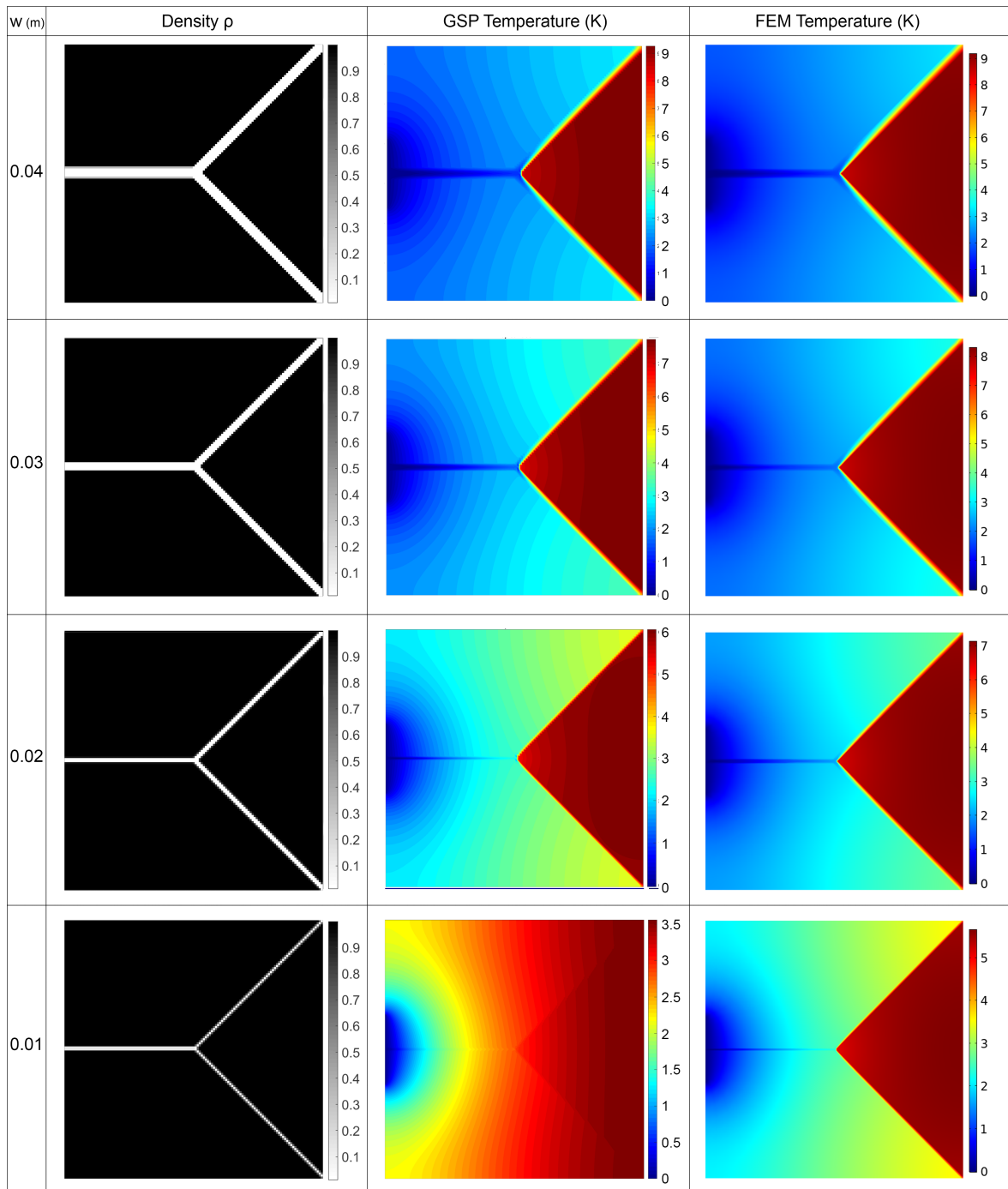


Figure C.3: GSP vs. FEM temperature comparison for a Y-split channel structure and high thermal conductive solid material ( $\kappa = 205 \text{ W m}^{-1} \text{ K}^{-1}$ ). Different channel widths  $w$  are shown. At smaller channel widths a discrepancy between the GSP and FEM models becomes visible. The GSP model cannot fully resolve the thin channels which results in a more diffuse temperature distribution and lower maximum temperatures.

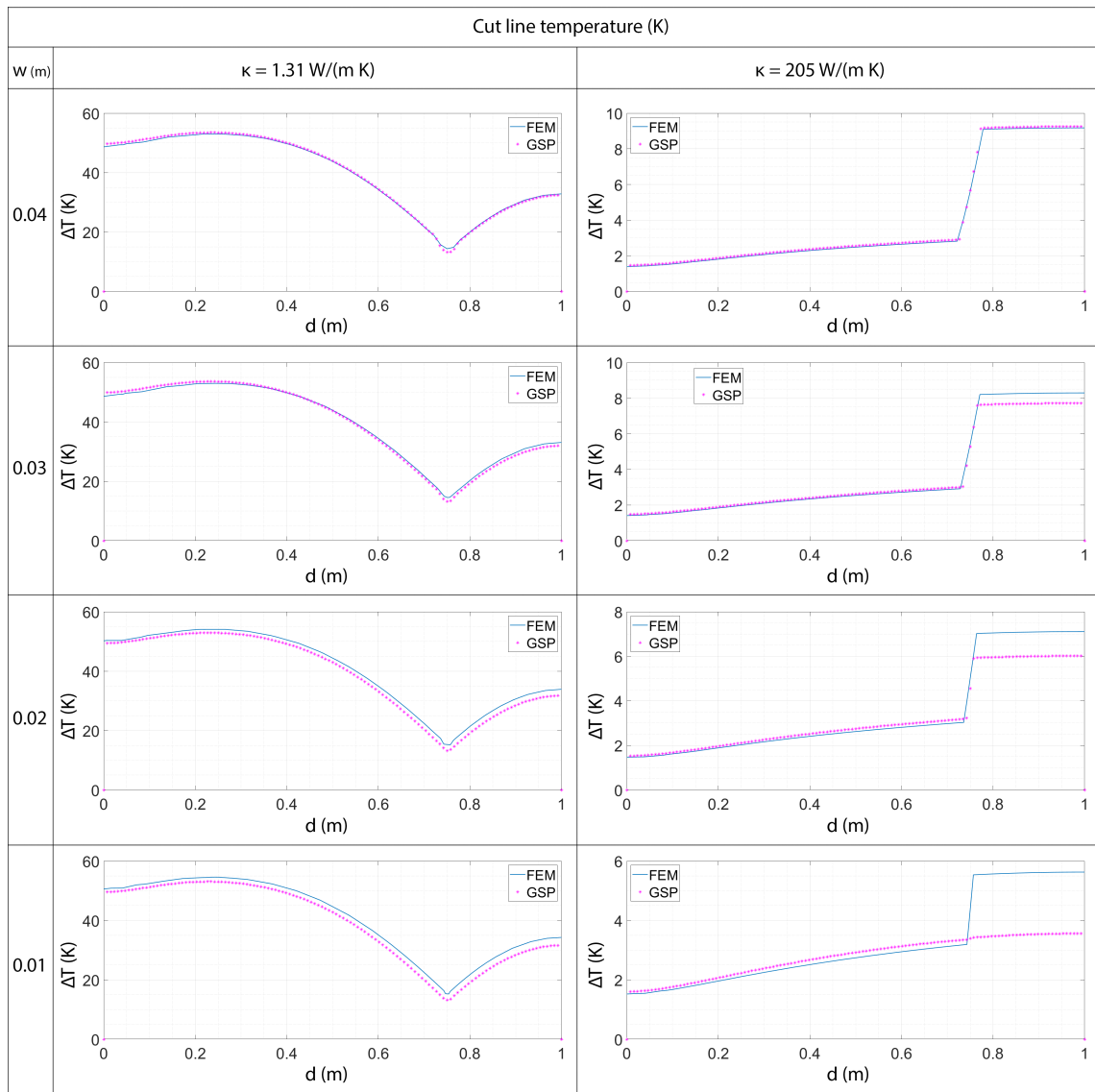


Figure C.4: Plotted temperatures of the GSP and FEM Y-split channel structure for different channel widths  $w$ . Temperatures are sampled along a cut line illustrated in Figure C.1. For the high thermal conductive material ( $\kappa = 205 \text{ W m}^{-1} \text{ K}^{-1}$ ) the GSP method starts to deviate significantly from the FEM model for thin channel widths.

### C.1.2. Velocity vectors

The velocity vectors of the flow are plotted in Figure C.5 to give a qualitative impression of the projected flow at the junction of the Y-split. Using the steps described in Chapter 3, a smooth transition is attained, comparable to the flow in the FEM model seen in Figure C.6. Note that the arrow scaling is different for the GSP- and FEM example.

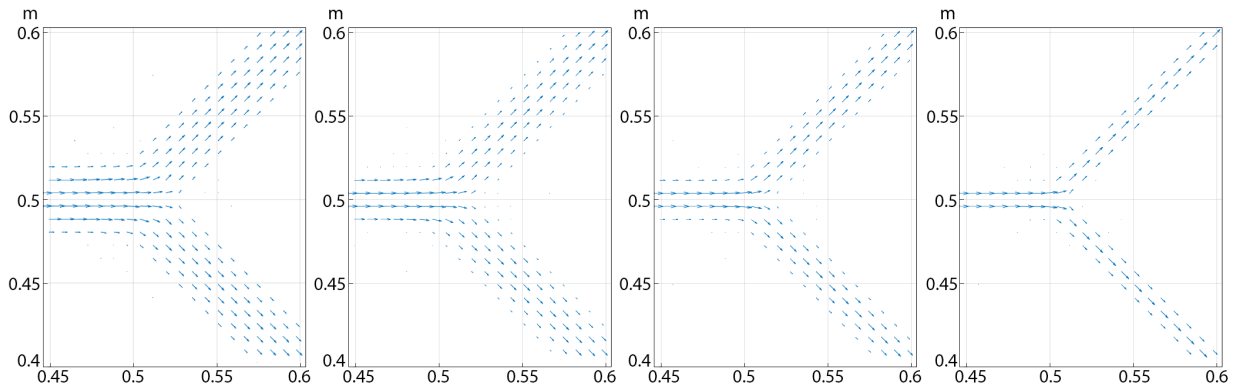


Figure C.5: Projected velocity vectors for a Y-split channel structure, plotted in Matlab. Channel width from left to right: 0.04 m, 0.03 m, 0.02 m, 0.01 m.

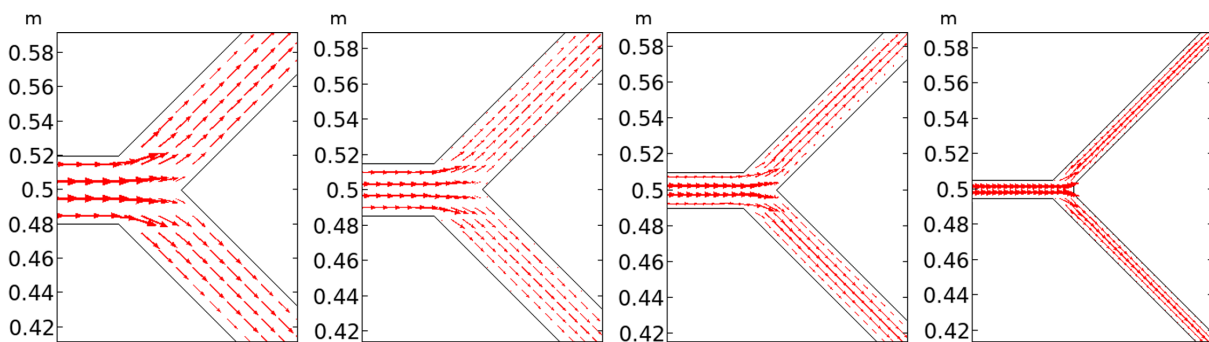


Figure C.6: Velocity vectors of an FEM simulation of the Y-split channel structure, plotted with Comsol. Channel width from left to right: 0.04 m, 0.03 m, 0.02 m, 0.01 m.

## C.2. Tapered channel

A comparison was also done for a tapered channel, see Figure C.7. With the GSP model, the tapered channel is approximated with five connected narrowing channel sections. The horizontal cut line drawn in Figure C.7 was used to evaluate and graph the temperatures in Figure C.8. Some difference for the temperature is observed near the entrance. This is likely due to the rough approximation with five channel sections.

Finally, Figure C.9 shows how the velocities at a transition of two channel sections are handled. Just before the transition, velocity vectors at the channel edges point slightly inwards, diverting flow towards the center of the channel. After the transition, the velocity vectors at the edges are smaller in magnitude, while the velocity vectors at the center of the channel have increased in magnitude.

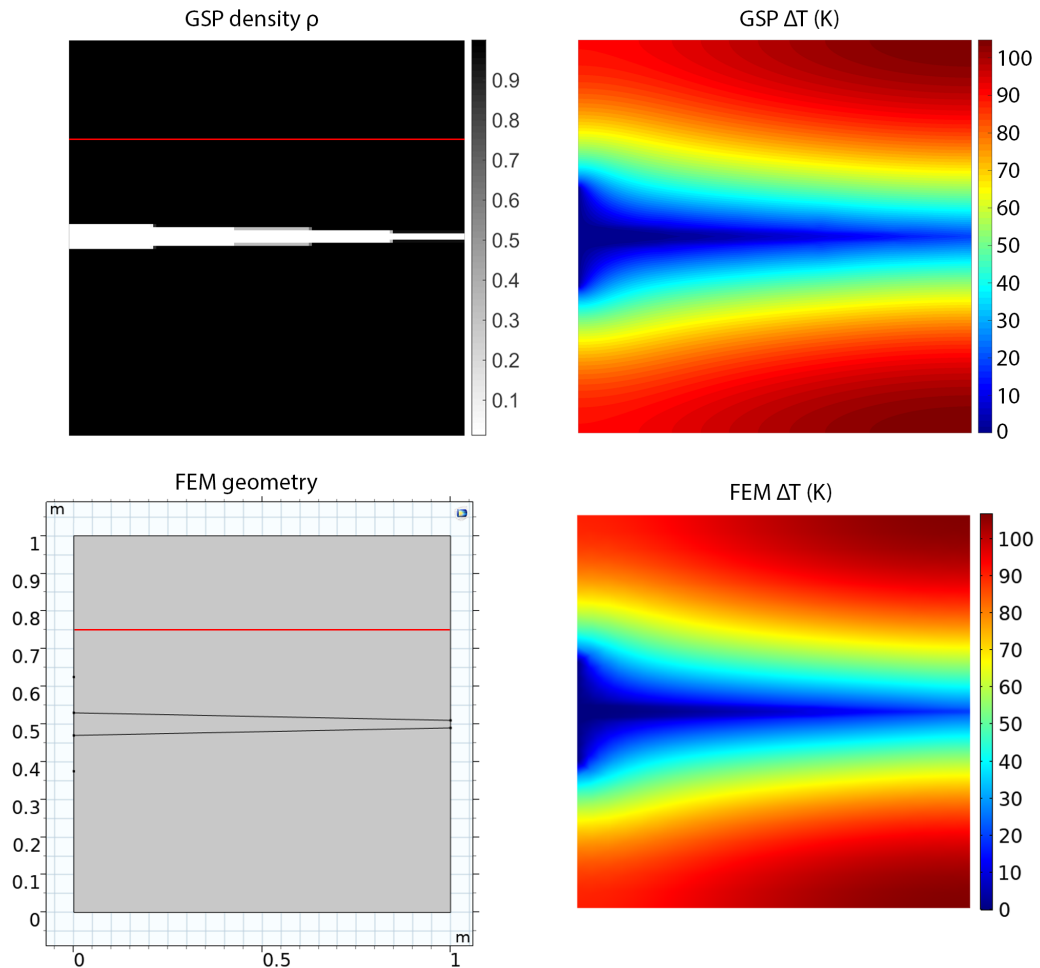


Figure C.7: Comparison between GSP method (top) and FEM model (bottom) of the temperature distribution with a tapered channel. The GSP ground structure consists of five narrowing channel sections, whereas the FEM geometry has a continuously narrowing channel. The red line in the figures of the GSP density distribution and FEM geometry is a cut line used to sample temperatures.

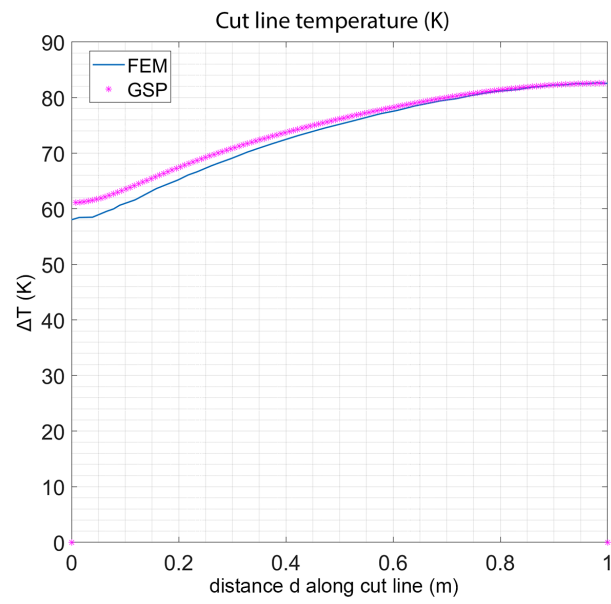


Figure C.8: Comparison graph of GSP vs. FEM, quantifying the temperature results along the cut line in Figure C.7.

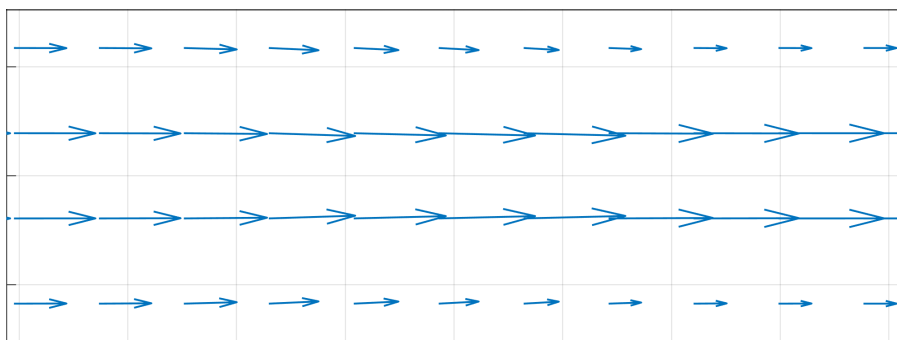


Figure C.9: Close-up of GSP velocity arrows at second to last channel connection. Before the transition, outer velocity vectors point inward. After the transition, outer velocity vectors are horizontal and smaller in magnitude.



# Bibliography

- [1] G. B. Airy. On the diffraction of an object-glass with circular aperture. *Transactions of the Cambridge Philosophical Society*, 5:283–291, 1835.
- [2] J. Alexandersen and C. Andreasen. A review of topology optimisation for fluid-based problems. *Fluids*, 5(29), 2020. doi: 10.3390/fluids5010029.
- [3] J. Alexandersen, O. Sigmund, and N. Aage. Large scale three-dimensional topology optimisation of heat sinks cooled by natural convection. *International Journal of Heat and Mass Transfer*, 100:876–891, 2016. doi: 10.1016/j.ijheatmasstransfer.2016.05.013.
- [4] G. Allaire, F. Jouve, and A. Toader. Structural optimization using sensitivity analysis and a level-set method. *Journal of Computational Physics*, 194:363–393, 2004. doi: 10.1016/j.jcp.2003.09.032.
- [5] J. Amanatides and A. Woo. A fast voxel traversal algorithm for ray tracing. In *EG 1987-Technical Papers*. Eurographics Association, 1987. doi: 10.2312/egtp.19871000.
- [6] A. M. Aragón, R. Saksena, B. D. Kozola, P. H. Geubelle, K. T. Christensen, and S. R. White. Multi-physics optimization of three-dimensional microvascular polymeric components. *Journal of Computational Physics*, 233:132–147, 2013. doi: 10.1016/j.jcp.2012.07.036.
- [7] Rocchini (Zom-B at en.wikipedia). Zernike polynomials, 2008. [https://commons.wikimedia.org/wiki/File:Zernike\\_polynomials2.png](https://commons.wikimedia.org/wiki/File:Zernike_polynomials2.png) [Accessed: 2019-07-19].
- [8] B. Bell, J. Norato, and D. Tortorelli. A geometry projection method for continuum-based topology optimization of structures. In *12th AIAA Aviation Technology, integration, and operations (ATIO) conference and 14th AIAA/ISSMO multidisciplinary analysis and optimization conference*, page 5485, 2012. doi: 10.2514/6.2012-5485.
- [9] M. P. Bendsoe and O. Sigmund. *Topology Optimization: Theory, Methods, and Applications*. Springer, Berlin, Heidelberg, 2004. ISBN 978-3-540-42992-0.
- [10] M. Bendsøe. Optimal shape design as a material distribution problem. *Structural optimization*, 1(4): 193–202, 1989. doi: 10.1007/BF01650949.
- [11] M. P. Bendsøe and O. Sigmund. *Topology Optimization: Theory, Methods, and Applications*. Springer-Verlag, 2003.
- [12] Max Born and Emil Wolf. *Principles of Optics: Electromagnetic Theory of Propagation, Interference and Diffraction of Light*. Pergamon Press, 1959. ISBN 978-1-108-47743-7.
- [13] O. Borrvall and J. Petersson. Topology optimization of fluids in stokes flow. *International Journal for Numerical Methods in Fluids*, 41:77–107, 2003. doi: 10.1002/flid.426.
- [14] J. E. Bresenham. Algorithm for computer control of a digital plotter. *IBM Systems Journal*, 4(1):25–30, 1965. doi: 10.1147/sj.41.0025.
- [15] S. Cho and J. Y. Choi. Efficient topology optimization of thermo-elasticity problems using coupled field adjoint sensitivity analysis method. *Finite Elements in Analysis and Design*, 41(15):1481–1495, 2005. doi: 10.1016/j.finel.2005.05.003.
- [16] A. J. Chorin. Numerical solution of the navier-stokes equations. *Mathematics of Computation*, 22:745–762, 1968. doi: 10.1090/S0025-5718-1968-0242392-2.
- [17] COMSOL. Comsol multiphysics® v. 5.5, 2021. [www.comsol.com](http://www.comsol.com). COMSOL AB, Stockholm, Sweden.

- [18] COMSOL. Cfd module user's guide, 2021. pp. 64, COMSOL Multiphysics® v. 5.5. [www.comsol.com](http://www.comsol.com). COMSOL AB, Stockholm, Sweden.
- [19] Erwin Coumans and Yunfei Bai. Pybullet, a python module for physics simulation for games, robotics and machine learning. <http://pybullet.org>, 2016–2021.
- [20] H. Cross. Analysis of flow in networks of conduits or conductors. *University of Illinois Bulletin*, 34(22), 1936.
- [21] E. M. Dede. Multiphysics topology optimization of heat transfer and fluid flow systems. In *Proceedings of the COMSOL Conference 2009 Boston*, 2009.
- [22] E. M. Dede, S. N. Joshi, and F. Zhou. Topology optimization, additive layer manufacturing, and experimental testing of an air-cooled heat sink. *Journal of Mechanical Design*, 137(11), 2015. doi: 10.1115/1.4030989.
- [23] H. Deng and A. C. To. Linear and nonlinear topology optimization design with projection-based ground structure method (p-gsm). *International Journal for Numerical Methods in Engineering*, 121(11):2437–2461, 2020. doi: 10.1002/nme.6314.
- [24] S. Deng and K. Suresh. Stress constrained thermo-elastic topology optimization with varying temperature fields via augmented topological sensitivity based level-set. *Structural and Multidisciplinary Optimization*, 56(6):1413–1427, 2017. doi: 10.1007/s00158-017-1732-2.
- [25] A. Diaz and O. Sigmund. Checkerboard patterns in layout optimization. *Structural optimization*, 10(1): 40–45, 1995. doi: 10.1007/BF01743693.
- [26] T. Dinh, H. Phan, N. Kashaninejad, T. Nguyen, D. V. Dao, and N. Nguyen. An on-chip sic mems device with integrated heating, sensing, and microfluidic cooling systems. *Advanced Materials Interfaces*, 5(2), 2018. doi: 10.1002/admi.201800764.
- [27] E. G. D. do Carmo and G. B. Alvarez. A new stabilized finite element formulation for scalar convection–diffusion problems: the streamline and approximate upwind/petrov–galerkin method. *Computer Methods in Applied Mechanics and Engineering*, 192(31–32):3379–3396, 2003. doi: 10.1016/S0045-7825(03)00292-5.
- [28] J. Donea and A. Huerta. *Finite Element Methods for Flow Problems*. Wiley, 2003. ISBN 9780471496663.
- [29] W. S. Dorn, R. E. Gomory, and H. J. Greenberg. Automatic design of optimal structures. *Journal de Mecanique*, 3(6):25–52, 1964.
- [30] N. Foster and D. Metaxas. Realistic animation of liquids. *Graphical Models and Image Processing*, 58(5): 471–483, 1996. doi: 10.1006/gmip.1996.0039.
- [31] A. Gersborg-Hansen, O. Sigmund, and R.B. Haber. Topology optimization of channel flow problems. *Structural and Multidisciplinary Optimization*, 30(3):181–192, 2005. doi: 10.1007/s00158-004-0508-7.
- [32] J. W. Gibbs and E. B. Wilson. *Vector Analysis: A Text-book for the Use of Students of Mathematics & Physics: Founded Upon the Lectures of J. W. Gibbs*. Yale University Press, 1901.
- [33] J. K. Guest. Imposing maximum length scale in topology optimization. *Structural and Multidisciplinary Optimization*, 37:463–473, 2009. doi: 10.1007/s00158-008-0250-7.
- [34] J. K. Guest, J. H. Prévost, and T. Belytschko. Achieving minimum length scale in topology optimization using nodal design variables and projection functions. *International Journal for Numerical Methods in Engineering*, 61(2):238–254, 2004. doi: 10.1002/nme.1064.
- [35] X. Guo, W. Zhang, and W. Zhong. Doing topology optimization explicitly and geometrically—a new moving morphable components based framework. *Journal of Applied Mechanics*, 81(8), 2014. doi: 10.1115/1.4027609.
- [36] R. T. Haftka. Techniques for thermal sensitivity analysis. *International Journal for Numerical Methods in Engineering*, 17(1):71–80, 1981. doi: 10.1002/nme.1620170106.

- [37] W. S. Hemp. *Optimum structures*. Clarendon Press, 1973.
- [38] S. D. Hudson. Poiseuille flow and drop circulation in microchannels. *Rheologica Acta*, 49:237–243, 2010. doi: 10.1007/s00397-009-0394-4.
- [39] Corning Incorporated. Corning® ule® glass, 2021. <https://www.corning.com/worldwide/en/products/advanced-optics/product-materials/semiconductor-laser-optic-components/ultra-low-expansion-glass.html> [Accessed: 2021-04-30].
- [40] C. Johnson, A. H. Schatz, and L. B. Wahlbin. Crosswind smear and pointwise errors in streamline diffusion finite element methods. *Mathematics of Computation*, 49(179):25–38, 1987. doi: 10.2307/2008248.
- [41] J. Y. Kim, K. Park, and S. Youn. The design of reflective mirrors for high-power laser systems using topology optimization. In *6th World Congress on structural and multidisciplinary optimization*, 2005.
- [42] W. Y. Kim, R. V. Grandhi, and M. Haney. Multi objective evolutionary structural optimization using combined static/dynamic control parameters. *AIAA Journal*, 44(4):794–802, 2006. doi: 10.2514/1.16971.
- [43] E. Kjeang, N. Djilali, and D. Sinton. Microfluidic fuel cells: A review. *Journal of Power Sources*, 186(2):353–369, 2009. doi: 10.1016/j.jpowsour.2008.10.011.
- [44] A. Klarbring, J. Petersson, B. Torstenfelt, and M. Karlsson. Topology optimization of flow networks. *Computer Methods in Applied Mechanics and Engineering*, 192(35-36):3909–3932, 2003. doi: 10.1016/S0045-7825(03)00393-1.
- [45] A. A. Koga, E. C. C. Lopes, H. F. Villa Nova, C. R. de Lima, and E. C. N. Silva. Development of heat sink device by using topology optimization. *International Journal of Heat and Mass Transfer*, 64:759–772, 2013. doi: 10.1016/j.ijheatmasstransfer.2013.05.007.
- [46] S. Koppen, M. van der Kolk, F. C. M. van Kempen, J. de Vreugd, and M. Langelaar. Topology optimization of multicomponent optomechanical systems for improved optical performance. *Structural and Multidisciplinary Optimization*, 58(3):885–901, 2018. doi: 10.1007/s00158-018-1932-4.
- [47] B. S. Lazarov and F. Wang. Maximum length scale in density based topology optimization. *Computer Methods in Applied Mechanics and Engineering*, 318:826–844, 2017. doi: 10.1016/j.cma.2017.02.018.
- [48] Q. Li, G. P. Steven, O. M. Querin, and Y. M. Xie. Optimization of thin shell structures subjected to thermal loading. *Structural Engineering & Mechanics*, 7(4):401–412, 1999. doi: 10.12989/sem.1999.7.4.401.
- [49] Q. Li, G. P. Steven, and Y. M. Xie. Thermoelastic topology optimization for problems with varying temperature fields. *Journal of Thermal Stresses*, 24(4):347–366, 2001. doi: 10.1080/01495730151078153.
- [50] G. Liu, L. Guo, X. Wang, and Q. Wu. Topology and parametric optimization based lightweight design of a space reflective mirror. *Optical Engineering*, 57(7):075101, 2018. doi: 10.1117/1.OE.57.7.075101.
- [51] MathWorks. Constrained nonlinear optimization algorithms, 2021. <https://nl.mathworks.com/help/optim/ug/constrained-nonlinear-optimization-algorithms.html#brnpd5f> [Accessed: 2021-03-27].
- [52] T. Matsumori, T. Kondoh, A. Kawamoto, and T. Nomura. Topology optimization for fluid–thermal interaction problems under constant input power. *Structural and Multidisciplinary Optimization*, 47(4):571–581, 2010. doi: 10.1007/s00158-013-0887-8.
- [53] A.F. Mills. *Basic Heat and Mass Transfer*. Pearson Higher Education, 2013. ISBN 978-1292042480.
- [54] J. Norato, B. Bell, and D. A. Tortorelli. A geometry projection method for continuum-based topology optimization with discrete elements. *Computer Methods in Applied Mechanics and Engineering*, 293:306–327, 2015. doi: 10.1016/j.cma.2015.05.005.
- [55] J. K. Nunes, K. Sadlej, J. I. Tama, and H. A. Stone. Control of the length of microfibers. *Lab on a chip*, 13:2301–2304, 2012. doi: 10.1039/C2LC40280G.

- [56] K. Park, S. Chang, and S. Youn. Topology optimization of the primary mirror of a multi-spectral camera. *Structural and Multidisciplinary Optimization*, 25(1):46–53, 2003. doi: 10.1007/s00158-002-0271-6.
- [57] K. Park, Lee J. H., and S. Youn. Lightweight mirror design method using topology optimization. *Optical Engineering*, 44(5):053002, 2005. doi: 10.1117/1.1901685.
- [58] E.W Parkes. Joints in optimum frameworks. *International Journal of Solids and Structures*, 11(9):1017–1022, 1975. doi: 10.1016/0020-7683(75)90044-X.
- [59] R. C. Penmetsa, R. V. Grandhi, and M. Haney. Topology optimization for an evolutionary design of a thermal protection system. *AIAA Journal*, 44(11):2664–2671, 2006. doi: 10.2514/1.15906.
- [60] A. Perazzo, J. K. Nunens, S. Guido, and H. A. Stone. Flow-induced gelation of microfiber suspensions. *Proceedings of the National Academy of Sciences*, 114(41):E8557–E8564, 2017. doi: 10.1073/pnas.1710927114.
- [61] M. Pietropaoli, F. Montomoli, and A. Gaymann. Three-dimensional fluid topology optimization for heat transfer. *Structural and Multidisciplinary Optimization*, 59(3):801–812, 2019. doi: 10.1007/s00158-018-2102-4.
- [62] O. Pironneau. On optimum design in fluid mechanics. *Journal of Fluid Mechanics*, 64(1):97–110, 1974. doi: 10.1017/S0022112074002023.
- [63] A. Pizzolato, A. Sharma, K. Maute, A. Sciacovelli, and V. Verda. Topology optimization for heat transfer enhancement in latent heat thermal energy storage. *International Journal of Heat and Mass Transfer*, 113: 875–888, 2017. doi: 10.1016/j.ijheatmasstransfer.2017.05.098.
- [64] C. Poelma. Exploring the potential of blood flow network data. *Meccanica*, 52(3):489–502, 2017. doi: 10.1007/s11012-015-0255-4.
- [65] F. A. Potra and S. J. Wright. Interior-point methods. *Journal of Computational and Applied Mathematics*, 124(1-2):281–302, 2000. doi: 10.1016/S0377-0427(00)00433-7.
- [66] C. Prohm and S. Holger. Feedback control of inertial microfluidics using axial control forces. *Lab on a chip*, 14:2115–2123, 2014. doi: 10.1039/C4LC00145A.
- [67] Y. Qu, Y. Jiang, L. Feng, X. Li, B. Liu, and W. Wang. Lightweight design of multi-objective topology for a large-aperture space mirror. *Applied Sciences*, 8(11):2259, 2018. doi: 10.3390/app8112259.
- [68] H. Rodrigues and P. Fernandes. A material based model for topology optimization of thermoelastic structures. *International Journal for Numerical Methods in Engineering*, 38(12):1951–1965, 1995. doi: 10.1002/nme.1620381202.
- [69] G. I. N. Rozvany. A critical review of established methods of structural topology optimization. *Structural and Multidisciplinary Optimization*, 37(3):217–237, 2009. doi: 10.1007/s00158-007-0217-0.
- [70] S. Seiffert and J. Thiele. *Microfluidics: Theory and Practice for Beginners*. De Gruyter, 2019. ISBN 9783110487770.
- [71] H. M. Shewan and J. R. Stokes. Review of techniques to manufacture micro-hydrogel particles for the food industry and their applications. *Journal of Food Engineering*, 119(4):781–792, 2013. doi: 10.1016/j.jfoodeng.2013.06.046.
- [72] O. Sigmund. Design of multiphysics actuators using topology optimization—part i: One-material structures. *Computer methods in applied mechanics and engineering*, 190(49-50):6577–6604, 2001. doi: 10.1016/S0045-7825(01)00251-1.
- [73] O. Sigmund and K. Maute. Topology optimization approaches: A comparative review. *Structural and Multidisciplinary Optimization*, 48:1031–1055, 2013. doi: 10.1007/s00158-013-0978-6.
- [74] O. Sigmund and S. Torquato. Design of materials with extreme thermal expansion using a three-phase topology optimization method. *Journal of the Mechanics and Physics of Solids*, 45(6):1037–1067, 1997. doi: 10.1016/S0022-5096(96)00114-7.

- [75] H. A. Smith and J. A. Norato. Topology optimization of fail-safe structures via geometry projection. In *AIAA 2021-2026 Session: Structural Optimization, Composite Material Design, Optimization with Multiscale Modeling II*, 2021. doi: 10.2514/6.2021-2026.
- [76] M. Stolpe and K. Svanberg. An alternative interpolation scheme for minimum compliance topology optimization. *Structural and Multidisciplinary Optimization*, 22(2):116–124, 2001. doi: 10.1007/s001580100129.
- [77] H. A. Stone, A. D. Stroock, and A. Ajdari. Engineering flows in small devices: Microfluidics toward a lab-on-a-chip. *Annual Review of Fluid Mechanics*, 36:381–411, 2004. doi: 10.1146/annurev.fluid.36.050802.122124.
- [78] M. Stynes. Convection-diffusion-reaction problems, sdfem/supg and a priori meshes. *International Journal of Computing Science and Mathematics*, 1(2-4), 2007. doi: 10.1504/IJCSM.2007.016543.
- [79] K. Svanberg. The method of moving asymptotes – a new method for structural optimization. *International Journal for Numerical Methods in Engineering*, 24:359–373, 1987. doi: 10.1002/nme.1620240207.
- [80] M. Tanyeri, M. Ranka, N. Sittipolkul, and M. Schroeder. A microfluidic-based hydrodynamic trap: Design and implementation. *Lab on a chip*, 11:1786–1794, 2011. doi: 10.1039/C0LC00709A.
- [81] F. Wein, P. D. Dunning, and J. A. Norato. A review on feature-mapping methods for structural optimization. *Structural and Multidisciplinary Optimization*, 62:1597–1638, 2020. doi: 10.1007/s00158-020-02649-6.
- [82] G. A. Whan and R. R. Rothfus. Characteristics of transition flow between parallel plates. *American Institute of Chemical Engineers*, 5(2):204–208, 1959. doi: 10.1002/aic.690050215.
- [83] C. Wieners. Taylor-hood elements in 3d. In: *Wendland W., Efendiev M. (eds) Analysis and Simulation of Multifield Problems. Lecture Notes in Applied and Computational Mechanics*, 12:189–196, 2003. doi: 10.1007/978-3-540-36527-3\_21.
- [84] S. Xu, Y. Cai, and G. Cheng. Volume preserving nonlinear density filter based on heaviside functions. *Structural and Multidisciplinary Optimization*, 41(4):495–505, 2010. doi: 10.1007/s00158-009-0452-7.
- [85] K. Yaji, T. Yamada, S. Kubo, K. Izui, and S. Nishiwaki. A topology optimization method for a coupled thermal–fluid problem using level set boundary expressions. *International Journal of Heat and Mass Transfer*, 81:878–888, 2015. doi: 10.1016/j.ijheatmasstransfer.2014.11.005.
- [86] K. Yaji, M. Ogino, Chen C., and K. Fujita. Large-scale topology optimization incorporating local-in-time adjoint-based method for unsteady thermal-fluid problem. *Structural and Multidisciplinary Optimization*, 58(2):817–822, 2018. doi: 10.1007/s00158-018-1922-6.
- [87] P. Yi, A. A. Kayani, A. F. Chrimes, K. Ghorbani, S. Nahavandi, K. Kalantar-zadeh, and K. Khoshmanesh. Thermal analysis of nanofluids in microfluidics using an infrared camera. *Lab on a chip*, 12:2520–2525, 2012. doi: 10.1039/C2LC40222J.
- [88] A. R. Yildiz and K. Saitou. Topology synthesis of multicomponent structural assemblies in continuum domains. *Journal of Mechanical Design*, 133(1), 2011. doi: 10.1115/1.4003038.
- [89] G. H. Yoon. Topological design of heat dissipating structure with forced convective heat transfer. *Journal of Mechanical Science and Technology*, 24(6):1225–1233, 2010. doi: 10.1007/s12206-010-0328-1.
- [90] M. Yu, S. Ruan, X. Wang, Z. Li, and C. Shen. Topology optimization of thermal–fluid problem using the mmc-based approach. *Structural and Multidisciplinary Optimization*, 60(1):151–165, 2019. doi: 10.1007/s00158-019-02206-w.
- [91] Zeiss. Extreme ultra violet (euv) lithography, 2017. <https://stories.zeiss.com/en/extreme-ultra-violet-lithography-euv/> [Accessed: 2019-07-19].
- [92] F. Zernike. Beugungstheorie des schneidenverfahrens und seiner verbesserten form, der phasenkontrastmethode. *Physica*, 1(7-12):689–704, 1934. doi: 10.1016/S0031-8914(34)80259-5.

- [93] W. Zhang, J. Yuan, J. Zhang, and X. Guo. A new topology optimization approach based on moving morphable components (mmc) and the ersatz material model. *Structural and Multidisciplinary Optimization*, 54:1243–1260, 2016. doi: 10.1007/s00158-015-1372-3.
- [94] W. Zhang, J. Chen, X. Zhu, J. Zhou, D. Xue, X. Lei, and X. Guo. Explicit three dimensional topology optimization via moving morphable void (mmv) approach. *Computer Methods in Applied Mechanics and Engineering*, 322(8):590–614, 2017. doi: 10.1016/j.cma.2017.05.002.
- [95] X. Zhao, Ole. Sigmund, and C. S. Andreasen. A “poor man’s approach” to topology optimization of cooling channels based on a darcy flow model. *International Journal of Heat and Mass Transfer*, 116:1108–1123, 2018. doi: 10.1016/j.ijheatmasstransfer.2017.09.090.
- [96] M. Zhou, B. S. Lazarov, F. Wang, and O. Sigmund. Minimum length scale in topology optimization by geometric constraints. *Computer Methods in Applied Mechanics and Engineering*, 293:266–282, 2015. doi: 10.1016/j.cma.2015.05.003.
- [97] T. Zhou, T. Liu, Y. Deng, L. Chen, S. Qian, and Z. Liu. Design of microfluidic channel networks with specified output flow rates using the cfd-based optimization method. *Microfluidics and Nanofluidics*, 21(11), 2017. doi: 10.1007/s10404-016-1842-y.
- [98] O. C. Zienkiewicz, R. L. Taylor, and J. Z. Zhu. *The Finite Element Method: Its Basis and Fundamentals*. Elsevier, 2005. ISBN 9780080472775.